ORNL/SPR-2021/2241

Oak Ridge National Laboratory Analysis of Approximations in Modeling of BWR Bundle Void Distributions

Chase Lawing, NCSU
Scott Palmtag, NCSU
David Kropaczek, ORNL

August 2021

OAK RIDGE National Laboratory

ORNL IS MANAGED BY UT-BATTELLE LLC FOR THE US DEPARTMENT OF ENERGY

ORNL/SPR-2021/2241

Nuclear Energy and Fuel Cycle Division

Analysis of Approximations in Modeling of BWR Bundle Void Distributions

Chase Lawing, NCSU

Scott Palmtag, NCSU

David Kropaczek, ORNL

Date Published: August 2021

Prepared by
OAK RIDGE NATIONAL LABORATORY
Oak Ridge, TN 37831
managed by
UT-Battelle LLC
for the
US DEPARTMENT OF ENERGY
under contract DE-AC05-00OR22725

CONTENTS

LIST OF FIGURES

LIST OF TABLES

ABBREVIATIONS

B_4C	Boron Carbide
BWR	boiling water reactor
CASL	Consortium for Advanced Simulation of Light Water Reactors
CTF	COBRA-TF
HFP	hot full power
kW/L	kilowatts per liter
LWR	light water reactor
MCNP	Monte Carlo Neutral Particle transport code
MOC	Method of Characteristics
NE	northeast
NW	northwest
PCM	percent-mille $\left(10^{-5}\right)$
PSIA	pounds per square inch (absolute pressure)
PWR	pressurized water reactor
RCS	reactor coolant system
RMS	root mean square
SE	southeast
SNVT	smeared thermal neutron fluence in units of $10^{21}\,\frac{ntns}{cm^2}$.
SW	southwest
Unnn	uranium-nnn
UO_2	uranium dioxide
VERA	Virtual Environment for Reactor Applications
VTM	VERA to MCNP
W/O	weight percent (the percent by mass of an isotope or element in a substance)

ACKNOWLEDGMENTS

For research to benefit the community, its purpose, methods, and results must be clearly documented for others to read. I would like to thank two reviewers, Dr. Jason Hou and Dr. David Kropaczek, for their excellent critiques of this report. They helped clarify and improve the presentation of information within the document and are very appreciated.

I would also like to thank my advisor, Dr. Scott Palmtag, for his guidance during my research. Along with providing support in understanding the computational software used, Dr. Palmtag provided direction and offered an expert perspective on the work conducted during this project. This often led to new and interesting questions to be answered and enriched the research experience.

This research used resources of the Compute and Data Environment for Science (CADES) at the Oak Ridge National Laboratory, which is supported by the Office of Science of the US Department of Energy under Contract No. DE-AC05-00OR22725.

Additional high-performance computing resources were provided by the Reactor Dynamics and Fuel Modeling Group of the Department of Nuclear Engineering at North Carolina State University.

ABSTRACT

In boiling water reactors, complex heterogeneous bundle designs, control blades adjacent to the corner of bundles, and the presence of boiling can lead to complex internal void distributions. A few approximations exist to model these void distributions. They could be modeled using a 1D axial solver in which each axial node is assumed to be at an average void, or each pin cell could be modeled with its own void concentration. In the latter case, the void could be discretized in pin-centered or coolant-centered channels. The goal of this project was to quantify the effect of using the different approximations for modeling internal void distributions on neutronics calculations. Using 3D void distributions calculated with CTF, Monte Carlo Neutral Particle (MCNP) transport code models were created for GE-9 and GE-14 lattices. For each model, the internal void distribution from CTF at a given axial node was selected, and a lattice calculation was carried out with MCNP. Comparisons between models using a lattice-averaged void, or using a void distribution in coolant-centered channels, showed large differences in reactivity which in some cases were well above 1,000 pcm, and it also showed differences in normalized fission rates greater than 20%. It was also found that using a lattice average void can lead to a significant difference in the estimation of the worth of a control blade. The differences found when comparing results from models using pin-centered and coolant-centered channels were up to 200 pcm in reactivity and up to 1.4% in the normalized fission rates. In addition to these two sets of comparisons, MCNP models were set up so that each subchannel had a saturated liquid component around the fuel pins and a saturated vapor component in the center to approximate annular flow. In comparison to the models using coolant-centered subchannels, up to 1–3% differences in normalized fission rates could be found.

1 Background

As of September 2019, there were 96 commercial nuclear power reactors producing about one fifth of the United States' electricity. All of these power reactors are light-water reactors (LWRs), meaning that they use ordinary water as the method of heat removal and neutron moderation. Of the 96 LWRs, 64 are pressurized water reactors (PWRs), and 32 are boiling water reactors (BWRs) [NRC, 2019].

In PWRs, heat is removed by a reactor coolant system (RCS) which is kept at a nominal pressure of approximately 2,250 psia. These high pressures ensure that at the core average exit temperatures of approximately 620 $^{\circ}$F [Todreas and Kazimi, 2011, p. 6], there is no bulk boiling, and only slight nucleate boiling is possible in the channels of the hottest fuel rods. Unlike PWRs, the RCSs in BWRs operate at lower nominal pressures of around 1,040 psia, and water exits the core as a saturated mixture at the saturation temperature of approximately 547 $^{\circ}$F [Todreas and Kazimi, 2011, p. 6].

LWRs are built to provide electricity, and as such, each power plant includes at least one steam-driven turbine that is used to convert energy carried by steam into electricity. Because PWRs use a high-pressure RCS, steam is not produced in the primary coolant system, and a secondary loop must be employed at a lower pressure to extract heat from the water of the RCS through a heat exchanger called a *steam generator*. The steam in this secondary loop drives the electricity production of the turbine. In BWRs, the lower pressures allow the coolant to exit the core as a saturated mixture. The steam is already present, and moisture separators and steam dryers are used to remove liquid droplets from the saturated mixture. This leaves only the steam, which can then be sent directly to the turbine. This means that BWRs do not need the secondary loop that is needed in PWRs.

Water not only removes heat from the fuel of LWRs, but it also serves as a source of neutron moderation. Collisions between neutrons and the hydrogen atoms in water molecules effectively transfer kinetic energy from neutrons and convert high-energy "fast" neutrons to lower energy "thermal" neutrons. For the purposes of this report, the energy groups for neutrons are taken to be those set out in Lewis' *Fundamentals of Nuclear Reactor Physics*[Lewis, 2008] and are presented in Table 1. Neutron cross sections, which describe the probability of an interaction between a neutron and an atom's nucleus, are measured in barns and are highly dependent on the energy of the incident neutron. Fission cross sections for the two most prevalent uranium isotopes in LWR fuel are described in Table 1. LWRs use uranium dioxide (UO_2) fuel in which the heavy metal atoms are mostly made up of ^{235}U (typically 3–5% by mass) and ^{238}U (typically 95–97% by mass). The fission cross sections of ^{235}U and ^{238}U show that, although the heavy metal mass of UO_2 is dominated by ^{238}U, the majority of fission is from the interaction of neutrons with energies less than 0.1 MeV and ^{235}U nuclei.

Table 1. Neutron energy range definitions with corresponding ^{235}U and ^{238}U microscopic fission cross sections [Lewis, 2008, p. 40, 76-77].

Energy range	Bounds [MeV]	σ_f ^{235}U [barns]	σ_f ^{238}U [barns]
Thermal	$(10^{-9}, 10^{-6})$	505	1.05×10^{-5}
Epithermal	$[10^{-6}, 10^{-1}]$	272	2×10^{-3}
Fast	$(10^{-1}, 10)$	1.22	0.304

In addition to cooling the fuel and moderating neutrons, water also serves as a method for reactivity control in LWRs. In PWRs, reactivity control is implemented by adding soluble boron to the coolant. The ^{10}B in the soluble boron, which has a thermal absorption cross section of over 3,800 barns (for the (n, α) reaction) [Shultis and Faw, 2008, p. 543], can absorb a large number of thermal neutrons and helps maintain steady-state operation. In BWRs, the method for reactivity control using water is through steam produced by boiling in the coolant as it flows along the length of the fuel. This steam is commonly referred to as *void*. The pumps in the BWR RCS can be used to increase or decrease the flow rate of water through the core with faster flow, thus leading to less void throughout the core. When large bubbles of steam form in the BWR's coolant, there are less water molecules and thus less hydrogen atoms locally in this steam as a result of its lower density. The rate, R, at which a neutron interaction of type x happens with atoms of isotope, i, is directly proportional to the number of atoms of the isotope per unit volume, N_i, the cross section for that isotope, σ_i^x, and the local neuron flux, ϕ.

$$R = N_i \sigma_i^x \phi \tag{1}$$

Thus, if x stands for a neutron scattering interaction, which is the interaction through which fast neutrons are thermalized in water, then Equation 1 shows that the lower density of steam indicates a lower rate of neutron thermalization.

1.1 A Closer Look at BWRs

In a BWR, fuel is contained in assemblies or bundles such as the GE14 bundle shown in Figure 1. BWR fuel bundles are unique in that they are contained within a Zircaloy channel box (note the purple box surrounding the fuel in Figure 1). Additionally, BWR fuel bundles often contain water boxes, water crosses, or large water rods such as the two sitting in the center of the GE14 bundle. All three structures allow water to travel vertically through the channel without being directly heated and boiled by fuel. The channel box surrounding BWR fuel bundles illustrates that there is no cross flow between assemblies, and each bundle is essentially its own pot to boil water in, with the heat source being the fuel rods.

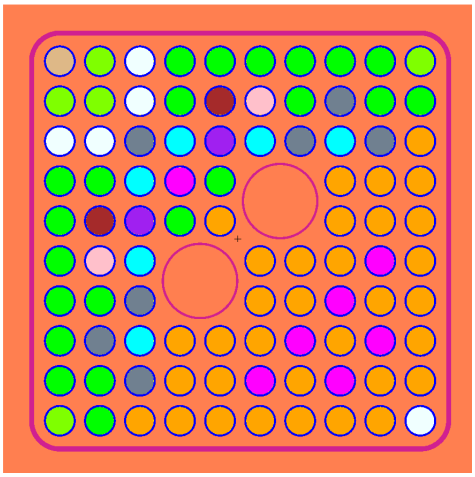

Figure 1. Radial cross section of a GE14 fuel bundle.

As water enters the bottom of the BWR core, its flow is divided between flowing beside fuel rods or flowing up through the gap outside of the channel box and through water rods. The water flowing through the water rods or outside the channel box is called *bypass flow*. All water enters the core subcooled, but the water that flows through the bundle next to the fuel immediately begins to capture heat from the UO_2 fuel as it conducts through the Zircaloy cladding. This heated water quickly becomes saturated and begins to boil. By the time it exits the top of the fuel bundle, it has absorbed enough heat from the fuel so that large amounts of steam can exist within the coolant of the bundle. The bypass flow does not gain much heat and is therefore still liquid. As more steam forms in the assembly coolant, neutron thermalization in the bypass flow water becomes more important because there is less neutron thermalization occurring in the lower density saturated mixture in the top of a BWR bundle.

The thermal neutron induced fission spectrum of ^{235}U235 is heavily weighted towards fast neutrons, with most neutrons born from fission having initial energies between 1 and 2 MeV [Todreas and Kazimi, 2011, p. 73]. Based on the fission cross sections in Table 1, neutrons have a very low probability of causing fission at these energies and must shed energy down to at least 0.1 MeV to increase the chances of inducing fission. This means that one important factor regarding the amount of neutrons available to cause fission is the rate at which fast neutrons born from fission are thermalized. Fuel assemblies in PWRs are very uniform. Typically, only one type of fuel is used, although some fuel pins may include a burnable absorber. Additionally, the high pressure of the RCS ensures that the coolant stays in a liquid form, so PWR assemblies will have mostly uniform moderator density distributions in a given assembly. This uniformity is not present in BWRs. As shown in Figure 1, BWR bundles may contain several types of fuel, and they may have increased heterogeneities such as water rods and channel boxes. These features in BWR bundles, coupled with the lower RCS pressure, lead to widely varying channel void distributions. That is, at a given axial level, one area of a BWR bundle may contain liquid water, whereas void bubbles are forming in another area of the same bundle.

The location of BWR control elements adds to the complexity of moderator density distribution (void distribution at higher levels in the bundle). In PWRs, control rods are inserted into

assemblies via guide tubes which are placed in an octant symmetric pattern within the assembly. As shown in the GE14 radial cross section in Figure 1, there is no room for a control element within a BWR assembly. In fact, control blades are inserted in the outer gap of BWR bundles, as shown in Figure 2. The control blade tubes are filled with B_4C, and as mentioned earlier, the high thermal absorption cross section of ^{10}B means that it absorbs a large number of the thermal neutrons that travel into the control blade tubes. Additionally, when the control blade is inserted into the gap outside the assembly, it displaces liquid water and thus lowers the number of water molecules. Again, less water molecules means a lower rate of neutron thermalization based on Equation 1. Therefore, the major effect of a control blade is to absorb thermal neutrons and thus locally decrease the number of thermal neutrons available for fission. The second effect of the control blade is that it lowers the rate of neutron thermalization and further decreases the thermal neutron availability. Both of these effects lead to suppression of fission rates and heat generation in fuel pins in the corner and along the edges where the control blade is inserted, whereas the fission rates of pins in the opposite corner to the control blade are less effected.

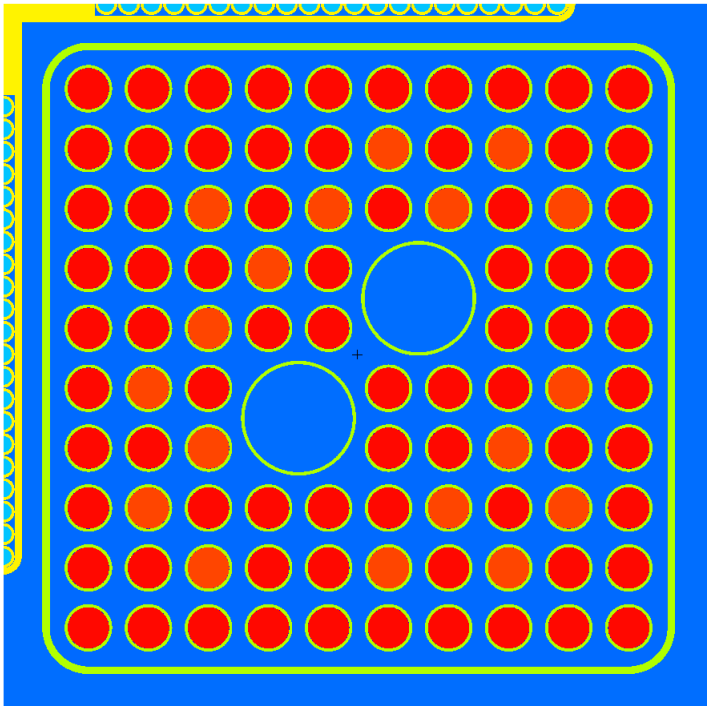

Figure 2. Control blade insertion at northwest (NW) corner of GE14 bundle. The control blade (yellow and light blue) can be seen running along the north and west edges of the system.

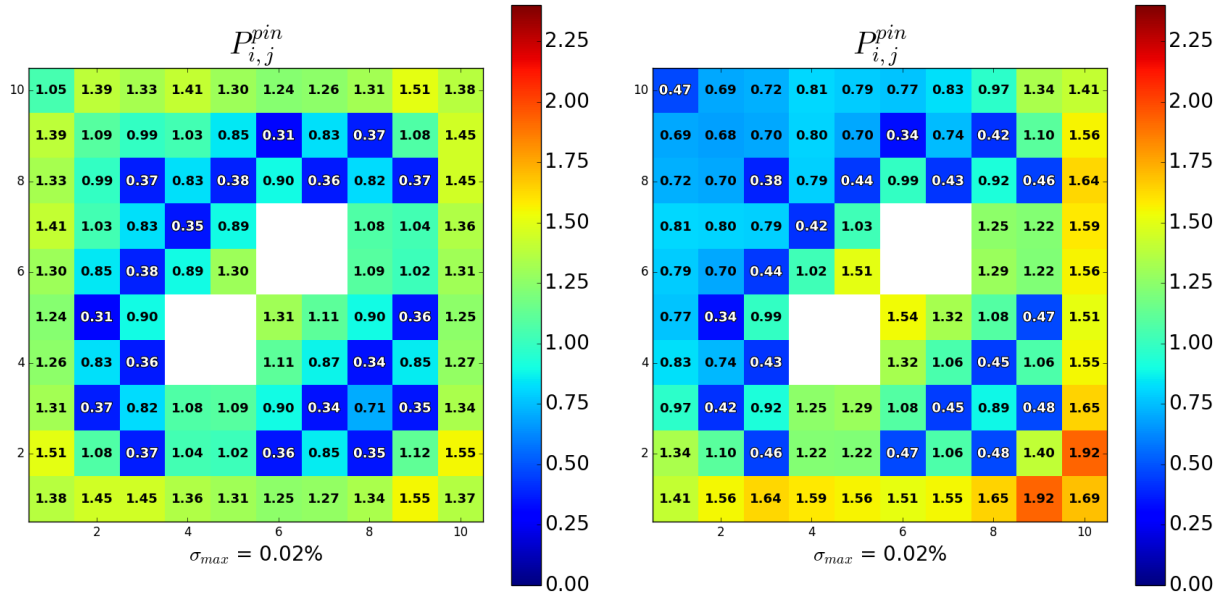

Figure 3. Normalized fission rates in an uncontrolled GE14 bundle (left) compared to that of an identical bundle with a control blade present at the NW corner (right) from an example set of MCNP calculations.

Figure 3 shows normalized fission rates in a GE14 bundle calculated with MCNP for an uncontrolled case and an identical case with a control blade inserted. The normalized fission rates in the NW corner are reduced by as much as 50% by the insertion of a control blade. When control blades are inserted in the gap next to a BWR bundle, the shift of power away from the controlled corner and towards the uncontrolled corner causes the water flowing through the controlled corner subchannels to boil less rapidly than that in the uncontrolled corners.

1.2 Objectives

The combination of complex BWR bundle geometries with water rods, channel boxes, moderator gaps outside of the bundle, and highly varied fuel pins with the low RCS pressure lead to potentially large moderator density gradients within a given bundle. Two examples of void distributions calculated by COBRA-TF (CTF) [Salko and Avramova, 2016] for a GE14 bundle are shown in Figure 4. CTF is a thermal-hydraulics code capable of calculating 3D subchannel based void distributions for 3D assemblies. It calculates these distributions using axial nodes. In this work, several axial nodes were selected for each bundle, and the corresponding radial void distribution at that axial level was extracted for use. This is how the radial void distributions in Figure 4 were obtained. A brief description of CTF is provided in paragraph 1.3.1.2.

As shown in Figure 4, for the uncontrolled case, subchannels have a void fraction as low as 7%, whereas some subchannels have void fractions as large as 47.3%. In the controlled case, the void fraction in a given subchannel can be as low as 0% or as high as 60% for this particular example.

This is a good example of the complex nature of the void distributions that can exist in BWR bundles.

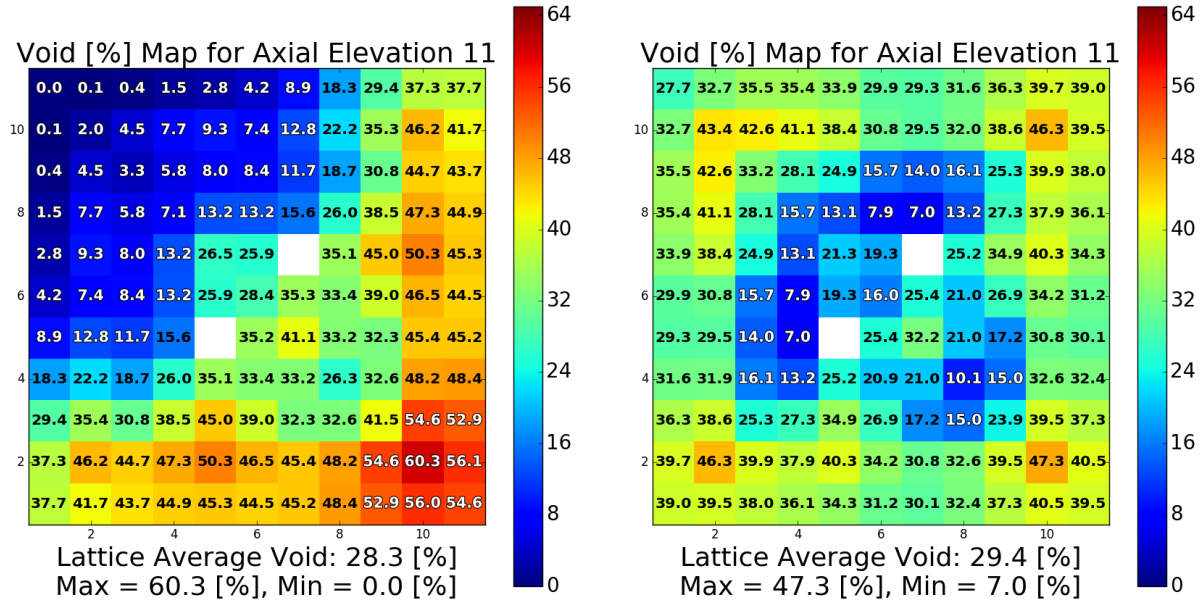

Figure 4. Void distribution for GE14 bundles with (left) and without (right) a control blade present in the NW corner.

The lattice average void, also referred to as the *bundle average void*, is calculated using Equation 2.

$$\overline{\alpha_{bun}} = \frac{\sum_{i=1}^{N} A_i \alpha_i}{\sum_{i=1}^{N} A_i} \tag{2}$$

In Equation 2, A_i is the flow area of subchannel i, α_i is the void fraction in subchannel i, and N is the total number of subchannels. Note that this calculation does not include the bypass flow.

1.2.1 Analysis of Bundle Average Void Approximation

In modern nodal codes, the void distribution in each assembly of a BWR is modeled using a 1D thermal-hydraulic solver. This method allows the void distribution to vary axially within each bundle, but it assumes that at a given height in the bundle, the radial void profile is uniform. In the best case, a nodal code will divide each bundle into four quadrants radially and determine the void in each of those quadrants. This method is better than the 1D solver, but it is still far from explicitly modeling void in each coolant-centered subchannel, as depicted in Figure 4.

If the example void profiles of Figure 4 are considered, then setting the void fraction in each subchannel to the lattice average void would be a similar approach to the 1D thermal-hydraulic solver used in modern nodal codes for a given axial level. However, the bundle average void of the uncontrolled case is only about 1% larger than the controlled case. Therefore, if a bundle averaged void were used, then the void distributions in each case would look very similar, but in reality, the

two distributions are extremely different. In the controlled case, the lowest voids are present in the NW corner of the bundle, whereas in the uncontrolled case, the lower voids are near the center of the assembly.

The previous example shows the amount of information that can be lost by assuming one uniform void radially for each axial node in a BWR assembly. When the void distribution is modeled inaccurately, the water density distribution is also modeled inaccurately as density, ρ, which is related to void fraction, α for cell i using the following equation:

$$\rho_i = (1 - \alpha_i)\,\overline{\rho_l} + \alpha_i \overline{\rho_g}, \tag{3}$$

where $\overline{\rho_l}$ and $\overline{\rho_g}$ are the liquid and vapor densities, respectively. The liquid density could be the density of subcooled liquid (when subcooled boiling occurs) or the saturated liquid density (when bulk boiling occurs). In this work, the densities are set to be $\overline{\rho_l} = 736.69\ kg/m^3$ and $\overline{\rho_g} = 37.5\ kg/m^3$; the saturated liquid and saturated vapor densities are set at 1,040 psia and were found using ChemicaLogic's SteamTab Companion [ChemicaLogic, 2003]. These saturated liquid and saturated vapor densities are used in the setup of all models in this project. (Note that this is a small approximation, because there is a slight pressure drop across the core height.) If an inaccurate void distribution is used which leads to an inaccurate moderator density distribution, then the rate of thermalization of neutrons is inaccurate, and thus the fission rates in fuel pins can be incorrect.

The first goal of this work was to use MCNP models with radial void distributions taken from a 3D CTF void distribution to determine how large the inaccuracy in fission rates can be as a result of the use of a uniform radial void profile. This objective was achieved through the use of MCNP models [Los, 2017] of 1 cm tall slices of the GE9 and GE14 bundles described in subsection 1.4. A 3D void distribution was obtained for each bundle type from CTF, and for a given axial node in the CTF void distribution, an MCNP model would be run with the CTF radial void distribution in that axial node. An identical MCNP case would be run with each subchannel set to the bundle average density calculated from the corresponding radial CTF void distribution using Equation 2. This process was completed for three different axial locations, translating to three different lattice average voids, for both the GE9 and GE14 geometries.

1.2.2 Approximation of Pin-Centered Channels for Neutronics Calculations

When CTF performs thermal-hydraulic calculations, the calculations and results are in coolant-centered channels throughout the assembly. This means that the channel geometry of a CTF calculation looks like that shown in Figure 5 (left). However, in neutronics codes such as MPACT, the moderator is discretized in pin-centered channels similar to those shown in Figure 5 (right). If detailed coupled thermal-hydraulic and neutronics calculations are performed, then moderator properties such as void distribution must be averaged over a pin cell. Averaging can be carried out using Equation 4.

$$\alpha^i = \frac{c^i_{nw} A^i_{nw} \alpha^i_{nw} + c^i_{ne} A^i_{ne} \alpha^i_{ne} + c^i_{sw} A^i_{sw} \alpha^i_{sw} + c^i_{se} A^i_{se} \alpha^i_{se}}{c^i_{nw} A^i_{nw} + c^i_{ne} A^i_{ne} + c^i_{sw} A^i_{sw} + c^i_{se} A^i_{se}}. \tag{4}$$

In Equation 4, α^i is the void fraction in pin cell i, A^i_{yx} is the flow area of the coolant-center channel in the yx corner of pin cell i, α^i_{yx} is the void fraction of the coolant-centered channel in the yx corner of pin cell i, and c^i_{yx} is the fraction of the area of the coolant-centered channel in the yx corner which lies within pin cell i. A depiction of this averaging can be seen in Figure 6. In pin cell 1 of Figure 6, the NW corner's coolant-centered channel is a corner channel and thus is fully contained in pin-centered channel 1, so for cell 1, $c^1_{nw} = 1$. The NE and southwest (SW) channels of pin cell 1 lie along the edges of the channel box, and as seen in the figure, it is clear that pin cell 1 contains half of the area of coolant-centered channels to its SW and NE, and $c^1_{ne} = c^1_{sw} = 1/2$. Finally, the southeast (SE) coolant-centered channel of pin-centered channel 1 is an interior channel, and pin-centered channel 1 contains a fourth of the area of this coolant-centered channel; thus, $c^1_{se} = 1/4$. In general, for corner channels like the NW coolant-centered channel in pin cell 1, $c^i_{yx} = 1$, and for edge channels such as the SW and NE channels of pin-centered channel 1, $c^i_{yx} = 1/2$. For interior coolant-centered channels like the SE corner of pin cell 1, and all four corners of pin cell 2, $c^i_{yx} = 1/4$.

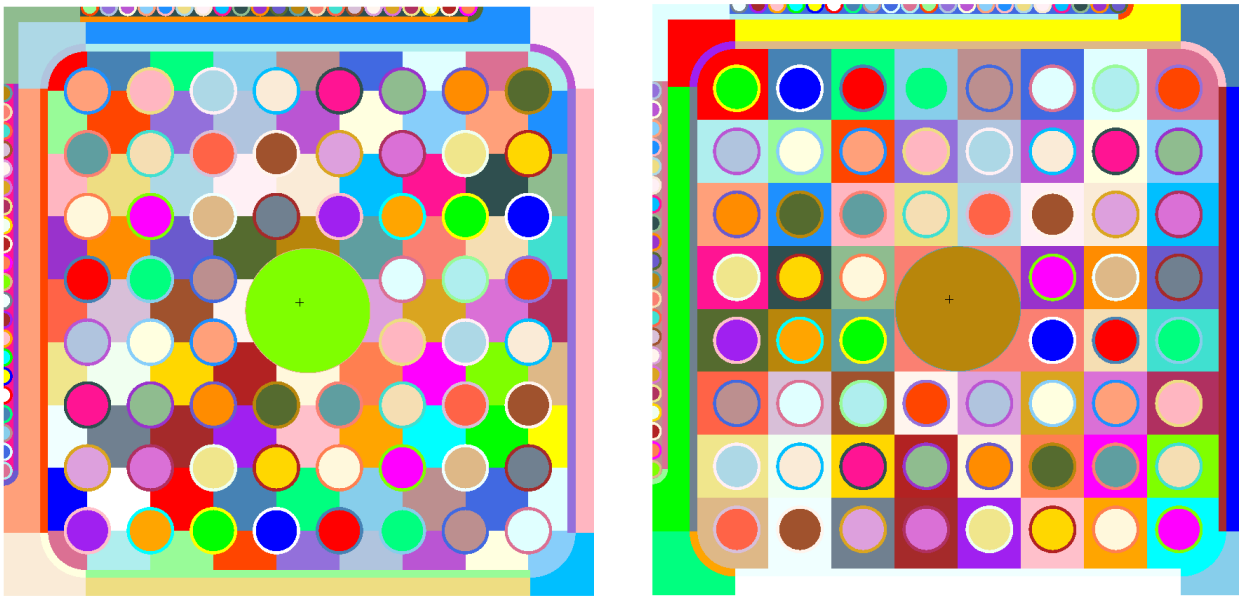

Figure 5. Example of coolant-centered channels (left) and pin-centered channels (right) representing the moderator in MCNP models of GE9 bundles.

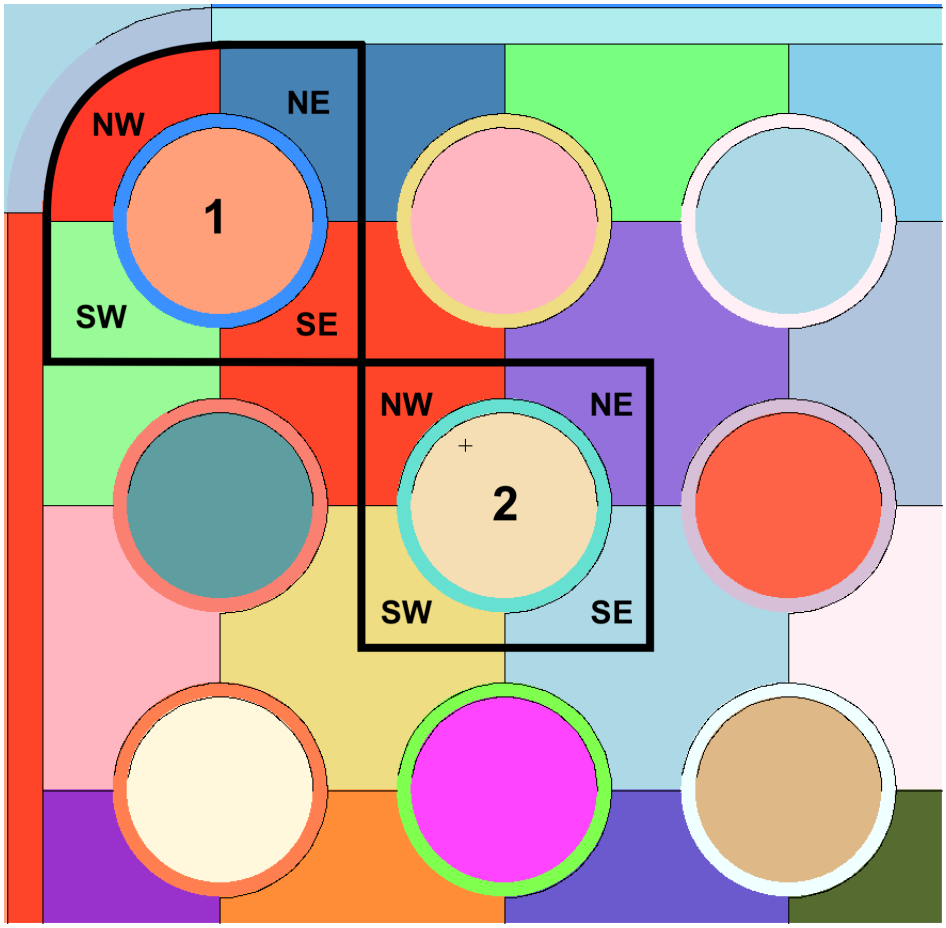

Figure 6. Pin-centered channel domain overlay onto coolant-centered channel domain for two pin cells.

The second goal of this project was to determine whether fission rates are sensitive to the use of averaged pin-centered channels as opposed to coolant-centered channels. This is important when modeling BWR bundles, which can have highly nonuniform void distributions with coupled codes. If a thermal-hydraulic code such as CTF, which uses coolant-centered channels, is used with a neutronics code such as MPACT, which uses averaged pin-centered channels, then it is possible that the loss of directionality in the moderator density around a fuel pin can lead to inaccurate fission rates. If this is the case, then the coupling of the two calculations is not as accurate as it could be if the two codes used the same moderator cell layout.

To analyze this issue, the generality of MCNP geometry is employed. At three axial levels of both a GE9 and GE14 bundle, an MCNP input is generated that uses the coolant-centered channel void distribution from CTF for a specific axial level. This same radial void distribution is then mapped to pin-centered channels using Equation 4, and an otherwise identical MCNP case is run using this pin-centered channel void distribution. If the fission rates in both cases agree, then the neutronics calculations are not sensitive to this method of obtaining and using pin-centered channels.

1.2.3 Annular Flow Approximations

In BWRs, the higher steam qualities and large vertical coolant flow rates lead to various two-phase flow regimes that occur within the channels of the BWR bundles. The annular flow regime occurs at high void fractions. In annular flow, a liquid film flows up along the fuel pins, and vapor flows through the center of the channel. The third objective of this project was to analyze the sensitivity of fission rates to annular flow. To do this, MCNP models were created to approximate the appearance of annular flow, as shown in Figure 7. Note that many two-phase flow regimes can exist in BWRs, such as bubbly flow, slug flow, and annular flow [Todreas and Kazimi, 2011, p. 603].

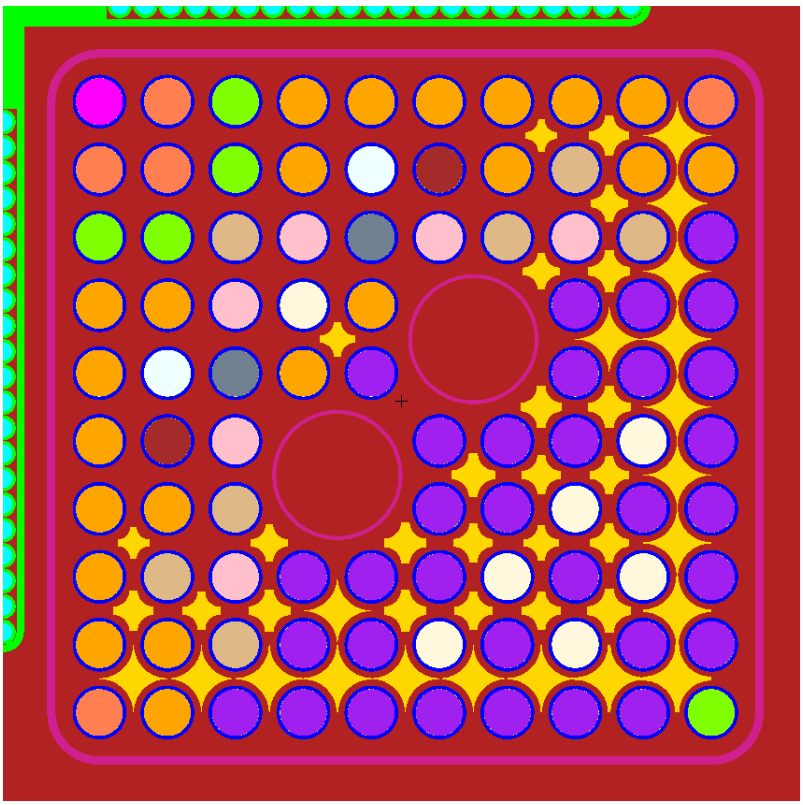

Figure 7. Example of an approximation of annular flow geometry in MCNP based on a CTF void distribution from a controlled GE14 bundle. The yellow spaces between fuel pins are saturated vapor, and red moderator areas are saturated liquid. In channels with no saturated vapor cell, the moderator density is set to the mixture density calculated using Equation 3.

To determine the sensitivity of fission rates to annular flow, MCNP cases must be run with an estimation of annular flow geometry. To achieve this, a 3D CTF void distribution was employed. MCNP inputs were generated for the GE9 and GE14 bundles with 1 cm heights for radial void distributions at 3 axial levels along the CTF results for the corresponding bundle type. Each moderator- centered channel of the void distribution was analyzed to determine the size of a vapor

cell if it is assumed that instead of a saturated mixture at a mixture density, a saturated liquid exists as a film on the fuel pins, and saturated vapor exists in the center of the channel. The size of the vapor cell is determined to preserve the mass of water within the channel. A more detailed description of the methods used to determine the dimensions of the vapor cell can be found in section A.

In each coolant-centered channel, if the void fraction for that cell is calculated by CTF to be less than 20%, then that cell is assumed to be bubbly flow and is modeled as a saturated mixture at the mixture density calculated using Equation 3. Therefore, for channels of less than 20% void, the model in that channel reverts back to the normal coolant-centered channel approach as discussed in the two previous sections. This also describes how channels directly adjacent to the channel box are handled. If the void is greater than 20%, then the channel is assumed to be occupied by a saturated liquid film around the 4 neighboring fuel pins and a separate saturated vapor region in the center of the channel. The 20% cutoff is based on the vertical flow regime map found in Todreas and Kazimi [Todreas and Kazimi, 2011, p. 607]. As shown in this map, at 20% void, the flow will transition into slug flow, in which elongated bubbles of vapor flow up through the centers of the channel. Thus, the image presented in Figure 7 shows a snapshot of the flow at which point, in the northwestern moderator channels, bubbly flow exists. Moving across the bundle from the NW corner towards the SE corner, smaller cells of saturated vapor begin to appear. This represents the large, elongated bubbles which flow through the center of the channels in slug flow. In channels near the south and east edges, the large vapor cells represent annular flow.

In the MCNP inputs for modeling annular flow, the radial profile of the vapor cells are in the shape of a square with a quarter circle removed from each corner. The determination of the shapes and sizes of these cells is described in section A. Instead of using a saturated mixture density, the water mass in the channel is preserved by creating separate cells, with saturated liquid at the saturated liquid density for 1,040 psia, and with saturated vapor at the saturated vapor density for 1,040 psia. The results from these cases are compared with those from MCNP cases which are run with coolant-centered channels filled with a saturated mixture at a density determined using Equation 3.

It is important to note that the goal of this segment of the project is not to determine an exact way to model annular flow, as this is an extremely difficult problem and is beyond the scope of the project. The goal is simply to insert some reasonable approximation to annular flow into MCNP models of BWR bundles and then to determine whether the results of these models are at all sensitive to the existence of a liquid film and vapor center in the channel. If the results indicate sensitivity to the inclusion of these annular flow approximations, then further research into the topic may yield more physically accurate simulations.

1.2.4 Effects of Radial Void Distribution on Control Blade Depletion

The final objective of this work is to determine how sensitive control blade absorption rates are to the use of a bundle average void instead of an internal radial void distribution. The idea is that if the use of a bundle average void profile leads to inaccurate fission rates, then the neutron population is being shifted around within the BWR bundle, and therefore, the neutron flux that makes it to the control blades may be inaccurate.

BWR control blades are usually replaced when their reactivity worth has decreased by 10% Kennard and Harbottle [2000]. If control blade depletion simulations rely on uniform radial void models, as is the case in modern nodal codes, then it is likely that the estimation on the depletion of control blades could be over or under approximated. This would mean that control blades might be getting replaced earlier than necessary, which would be of economic importance, or they might be getting replaced too late, when their worth has actually decreased to less than 90%, which would be a safety concern.

To determine how the use of a bundle-averaged void affects control blade depletions, control blades were depleted next to GE9 and GE14 bundles with a radial void distribution and again with a uniform void distribution at the bundle average void. In these calculations, the control blade was assumed to be constantly inserted and it was also assumed that the fuel does not deplete. Additionally, the radial void distribution was assumed to be constant as the control blade depletes. These calculations should provide some idea of the sensitivity of control blade absorption rates to the void distribution within the bundle.

1.3 Simulation Tools Used

1.3.1 Virtual Environment for Reactor Applications (VERA)

The Virtual Environment for Reactor Applications (VERA) is the result of work performed under the Consortium for Advanced Simulation of Light Water Reactors (CASL). VERA includes a suite of computational software which can be used to model LWRs. These tools represent the state of the art in reactor simulation, offering capabilities such as calculation of 3D, pin-resolved power distributions, and fuel depletion ORNL.

Some of VERA's computational tools were used for the work presented in this report, namely, CTF, MPACT, and VERAin. Brief descriptions of these tools and how they were used are presented in the following sections.

1.3.1.1 MPACT

MPACT is a 3D neutron transport code that was developed in a collaboration between the University of Michigan, Oak Ridge National Laboratory, and CASL. The code allows whole core power and burnup calculations to be determined at a pin-by-pin resolution. MPACT offers solutions with the 3D method of characteristics (MOC), or additionally, it offers the option to model the core radially using a 2D MOC calculation coupled with a 1D P_3 or neutron diffusion calculation in the axial direction *et al* [2015].

MPACT is a versatile code that can be used to model anything from a pin cell to a full core calculation. When used with VERA, MPACT can perform coupled detailed thermal hydraulic and neutronics using CTF. MPACT was used in this work to calculate a radial pin power distribution which could be input into CTF and used to determine a 3D void distribution for use in MCNP models.

1.3.1.2 COBRA-TF (CTF)

COBRA-TF, or CTF, is a detailed, two-fluid thermal-hydraulic code which considers the three fluid fields: continuous liquid, continuous vapor, and liquid droplets Salko and Avramova [2016]. For each field, CTF considers three conservation equations: conservation of mass, conservation of momentum, and conservation of energy. However, the continuous liquid and liquid droplet fields share the energy equation. The equations are coupled by consideration of mass and energy transfer between fields Salko and Avramova [2016]. When used with VERA, CTF can perform coupled neutronics and thermal-hydraulic calculations to obtain the most physically accurate results possible. As previously mentioned, CTF solves its equations in coolant-centered channels. Additionally, CTF is capable of analyzing cross flow between the coolant-centered channels, the effects of spacer grids on coolant flow, and heat conduction from fuel pins. The effects of spacer grids on coolant flow enters the problem through the conservation of energy equations as it considers heat energy being transferred into the fluid Salko and Avramova [2016].

In this work, CTF was used to obtain a 3D void distribution for controlled and uncontrolled GE9 and GE14 bundles. For each test case, a radial void distribution would be extracted from a given axial location in this 3D void distribution (see the two radial distributions shown in Figure 4 as an example). These radial void distributions can then be used on a coolant-centered channel basis directly in MCNP. Additionally, with post-processing, corresponding pin-centered channel data can be calculated using Equation 4, and a bundle average void can be calculated using Equation 2.

1.3.1.3 VERAin

The common input for VERA (see the simple example in section C) is used across all codes used in VERA. That is, MPACT, CTF, and other reactor simulation software packaged with VERA can be used from the same input file. VERAin takes the simple text file inputs and converts them into extensible markup language (XML) files that can be easily interpreted by the suite of codes offered in VERA.

To complete the work detailed in this report, it was necessary to generate many MCNP models of BWR bundles. This is a tedious, error-prone task when carried out by hand. To mitigate the risk of errors in the MCNP inputs and to speed up the process of input generation, a Python program, VERA to MCNP (VTM), was created to read the XML-formatted files generated by VERAin and build a corresponding MCNP input file. A more detailed description of VTM can be found in section B.

1.3.2 Monte Carlo N-Particle Transport Code (MCNP)

MCNP uses a stochastic approach to particle transport and can model many types of particles, including neutrons and photons. MCNP uses continuous-energy cross sections and allows for a very general geometry specification. In this project, the general geometry aspect of MCNP is leveraged because it easily allows for modeling pin-centered or coolant-centered channels, and these channels can be set up to use any type of void distribution. For all calculations presented in this document, MCNP version 6.2 Los [2017] was used with the continuous-energy cross section

library ENDF/B-VII.1.

1.3.3 VERA to MCNP

MCNP is a very useful tool. It allows the user to model very general geometries and materials. This generality comes at the cost of an input which in most cases is tedious to build. For the problems considered in this work, the MCNP models consisted of up to a few hundred cells and a few hundred surfaces that were used to define the shape of those cells. Each cell must have material, density, temperature, and surface specifications. All surfaces must have coordinates and dimensions defined. Additionally, all materials used in the problem must have their isotopic make-ups and temperatures specified. To build inputs for MCNP cases—such as those used in this project, which have complications such as varied moderator densities— would be very time consuming and error prone. However, the VERA common input is very easy to build (see example in section C). A Python program known as VERA to MCNP (VTM) was developed to utilize the simplicity of the VERA common input to build MCNP inputs. VTM uses the VERA common inputs in XML format to obtain problem geometry, material, and temperature specifications. Additionally, VTM can read the results of CTF calculations and apply the void distributions to BWR bundles in MCNP models.

In this work, the only type of inputs needed were 1 slice (uniform in the axial direction) BWR bundles. However, VTM can generate inputs for pin cell, single-assembly, and multi-assembly cases for both BWRs and PWRs. More details about VTM can be found in section B.

1.4 Bundle Descriptions

1.4.1 GE9 Bundle

A depiction of the GE9 bundle geometry modeled in this work is shown in Figure 8. Dimensions corresponding to this diagram are listed in Table 2. The fuel layout of the GE9 bundle modeled in all GE9 test cases can be seen in Figure 9, and the corresponding fuel descriptions are laid out in Table 3. All geometry specifications and isotopic data for fuel were obtained from the information presented in Kelly [1995].

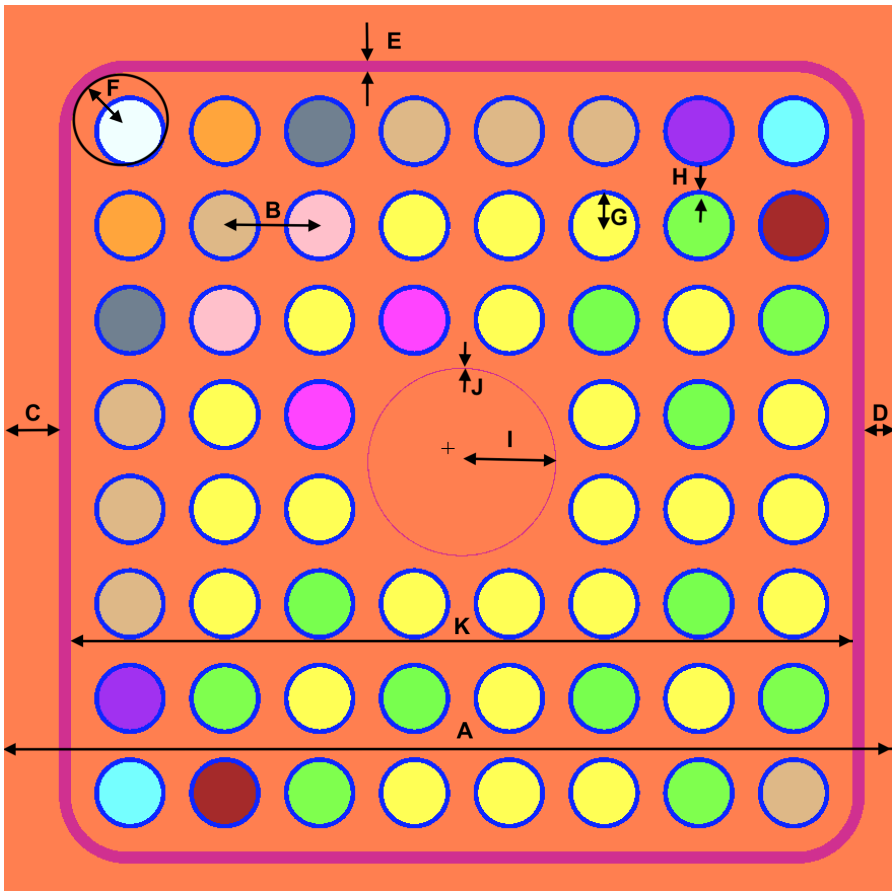

Figure 8. Diagram for parameters of interest in GE9 assembly. Corresponding dimensions can be found in Table 2.

Table 2. Geometric description of GE9 bundle analyzed Kelly [1995]

Parameter	Key in Figure 8	Value
Assembly pitch [cm]	A	15.24
Pin pitch [cm]	B	1.6256
Wide gap [cm]	C	0.9525
Narrow gap [cm]	D	0.47498
Channel box thickness [cm]	E	0.2032
Channel box corner radius [cm]	F	0.9652
Fuel radius [cm]	G	0.53213
Fuel clad thickness [cm]	H	0.08128
Water rod radius [cm]	I	1.60
Water rod clad thickness [cm]	J	0.02
Internal width [cm]	K	13.40612
Number of pins across edge	-	8

Notice that the internal distance across the bundle, K, is slightly larger than the number of pins across the edge times the pin pitch: $1.6256\,cm \times 8 = 13.0048\,cm$. There is an internal gap padding the channel box facing side of pin cells along the bundle edges. This internal gap is 0.20066 cm wide and is determined using Equation 5, where IG is the internal gap, N_{pin} is the number of pins along the edge of the bundle, and all other symbols are as shown in Table 2 from Palmtag [2015].

$$IG = \frac{A - 2E - C - D - N_{pin}B}{2}. \tag{5}$$

It is also important to note that the radius for the water rods shown above is slightly smaller than that provided in Kelly [1995] (1.6002 cm). Additionally, the thickness of the water rod cladding has been reduced in the models contained in this work from the original thickness obtained from Kelly [1995] (0.1016 cm). This was done for compatibility with MPACT. Pin powers were estimated in MPACT, and these pin powers were provided as the radial pin power distribution in the CTF input deck used to generate the void distributions for this work. At the time of these calculations, MPACT could only model oversized water rods that fit within a 2×2 block of pin cells. Because this is consistent in all models that were run, this slight change to the water rod dimensions will not significantly impact the ability to confidently answer the questions laid out in subsection 1.2. For example, in calculating the differences in pin powers and eigenvalue caused by the use of a bundle average void vs. an internal void distribution, both models will be using the reduced sized water rod, so the differences found in eigenvalue and pin powers will be unaffected by the changes to the water rod size.

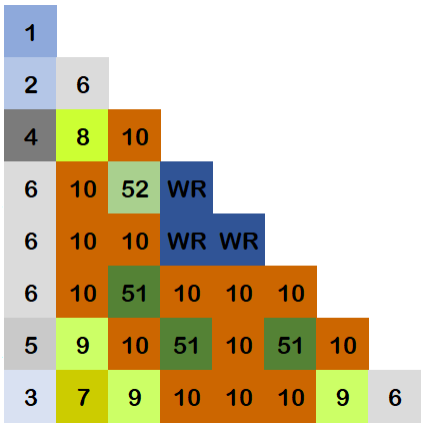

Figure 9. Fuel layout of diagonally symmetric GE9 bundle. A single large water rod occupies 4 cells in the center of the bundle. The four cells are marked "WR." The fuel types used in this assembly are described in Table 3. This information was obtained using number densities from Kelly [1995].

Table 3. Isotopic description of fuel types used in the GE9 bundle analyzed

Fuel type	^{235}U [w/o]	Gad [w/o]	Fuel type	^{235}U [w/o]	Gad [w/o]
1	1.60	0.0	7	3.00	0.0
2	2.00	0.0	8	3.60	0.0
3	2.20	0.0	9	3.80	0.0
4	2.40	0.0	10	3.95	0.0
5	2.60	0.0	51	3.95	4.0
6	2.80	0.0	52	3.60	4.0

Note the unit *[w/o]* in Table 3 and Table 5 means "weight percent," and in this context, it is the percent by mass of the heavy metal taken up by the indicated isotope. This means that fuel type 1 in Table 3 is 3 % ^{235}U by mass heavy metal.

1.4.2 GE14 Bundle

A diagram of the GE14 bundle is shown in Figure 10, and the dimensions corresponding to this diagram are tabulated in Table 4. The geometry of the GE14 bundle was obtained from the report on the KBS-3 Repository REP [2010]. Information for the fuel layout of the GE14 bundle was gathered from Fensin [2004]. The fuel layout and isotopic description can be found in Figure 11 and Table 5.

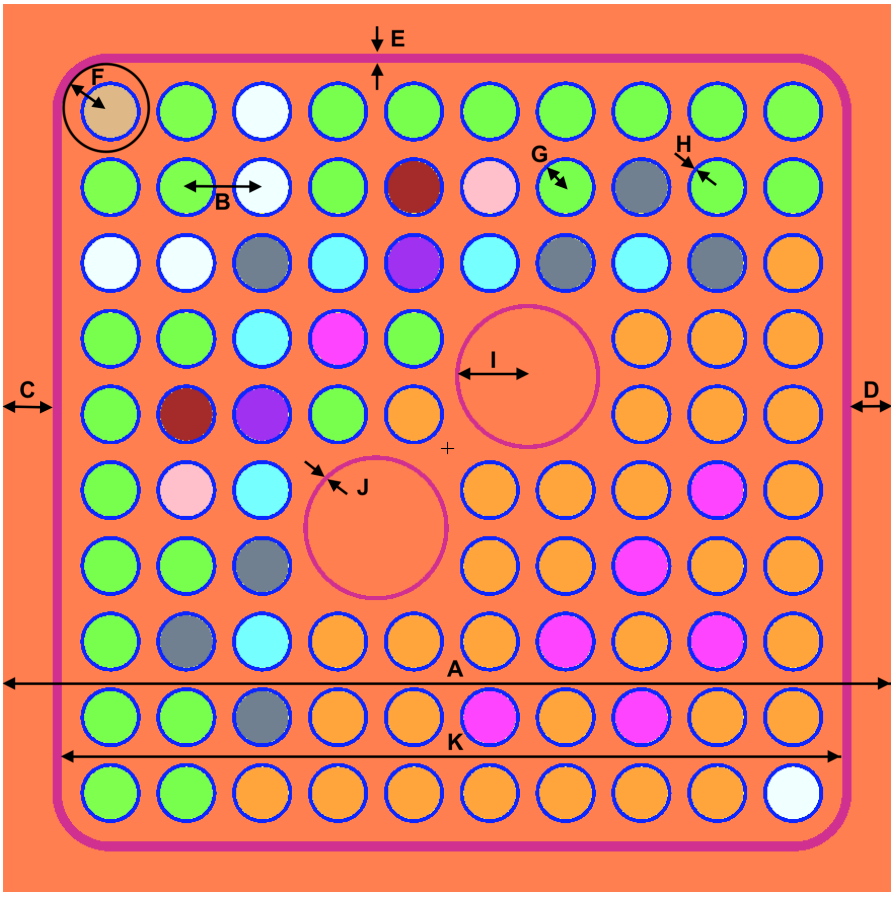

Figure 10. Diagram of parameters of interest for the GE14 bundle analyzed. The geometric design of the GE14 bundle was obtained from the report on the KBS-3 Repository REP [2010], and the dimensions corresponding to this diagram can be found in Table 4.

Table 4. Geometric description of GE14 bundle analyzed REP [2010]

Parameter	Key in Figure 10	Value
Assembly pitch [cm]	A	15.24
Pin pitch [cm]	B	1.3
Wide gap [cm]	C	0.840
Narrow gap [cm]	D	0.700
Channel box thickness [cm]	E	0.165
Channel box corner radius [cm]	F	0.837
Fuel radius [cm]	G	0.447
Fuel clad thickness [cm]	H	0.066
Fuel gap [cm]	-	0.002
Water rod radius [cm]	I	1.17
Water rod clad thickness [cm]	J	0.075
Internal width [cm]	K	13.4
Number of pins across edge	-	10

As with the GE9 bundle, the internal gap of moderator padding the channel box–facing side of pin cells along the edge of the bundle can be determined using Equation 5.

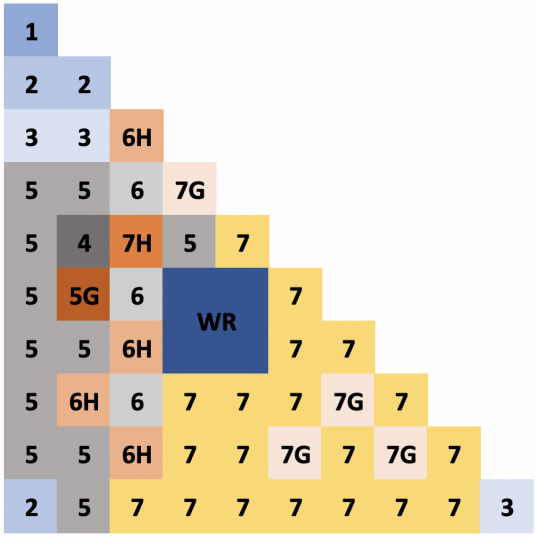

Figure 11. Fuel layout of diagonally symmetric GE14 bundle. Two large water rods, one in each half of the bundle, occupy four cells each near the center of the bundle. Descriptions of the fuel types used in this assembly can be seen in Table 5. The fuel layout and fuel descriptions were obtained from Fensin [2004].

Table 5. Isotopic description of fuel types used in the GE14 bundle analyzed. The ^{235}U and gadolinium weight fractions were gathered from Fensin [2004]

Fuel type	^{235}U [w/o]	Gad [w/o]	Fuel type	^{235}U [w/o]	Gad [w/o]
1	1.60	0.0	7	4.90	0.0
2	2.80	0.0	5G	3.95	8.0
3	3.20	0.0	6H	4.40	6.0
4	3.60	0.0	7G	4.90	8.0
5	3.95	0.0	7H	4.90	6.0
6	4.40	0.0			

1.4.3 Original Equipment Manufacturer Control Blades

The control blades described in this section are used in both the GE9 and the GE14 models. Although newer control blade designs exist, they are typically designed to have the same rod worth as the original equipment manufacture (OEM) designs, so the use of OEM control blades is deemed acceptable for the neutronics calculations in this work.

In general, the control blade data were found in the work by Solius *et al* [2001]. However, the stainless steel density was obtained from from United Performance Metals. Also, in Solius *et al* [2001], the B_4C is stated to be 70% of the theoretical density. A theoretical density of 2.51 g/cc for B_4C powder was obtained from Reade READE. The 1.757 g/cc as shown in the table below is 70% of 2.51 g/cc.

Table 6. Control blade data for controlled cases from Solius *et al* [2001]

Parameter	Key in Figure 12	Value
Blade material	-	Stainless steel
Control pin clad material	-	Stainless steel
Absorber material	-	B_4C
Stainless steel density [g/cc]	-	8.0
B_4C density [g/cc]	-	1.757
Number of absorber pins per wing [g/cc]	-	21
Blade span [cm]	A	12.3825
Blade half thickness [cm]	B	0.39624
Blade tip radius [cm]	C	0.39624
Absorber tube outer radius [cm]	D	0.23876
Absorber tube clad thickness [cm]	E	0.0635
Thickness of control blade walls (sheath) [cm]	F	0.14224
Central structure thickness [cm]	G	1.98501

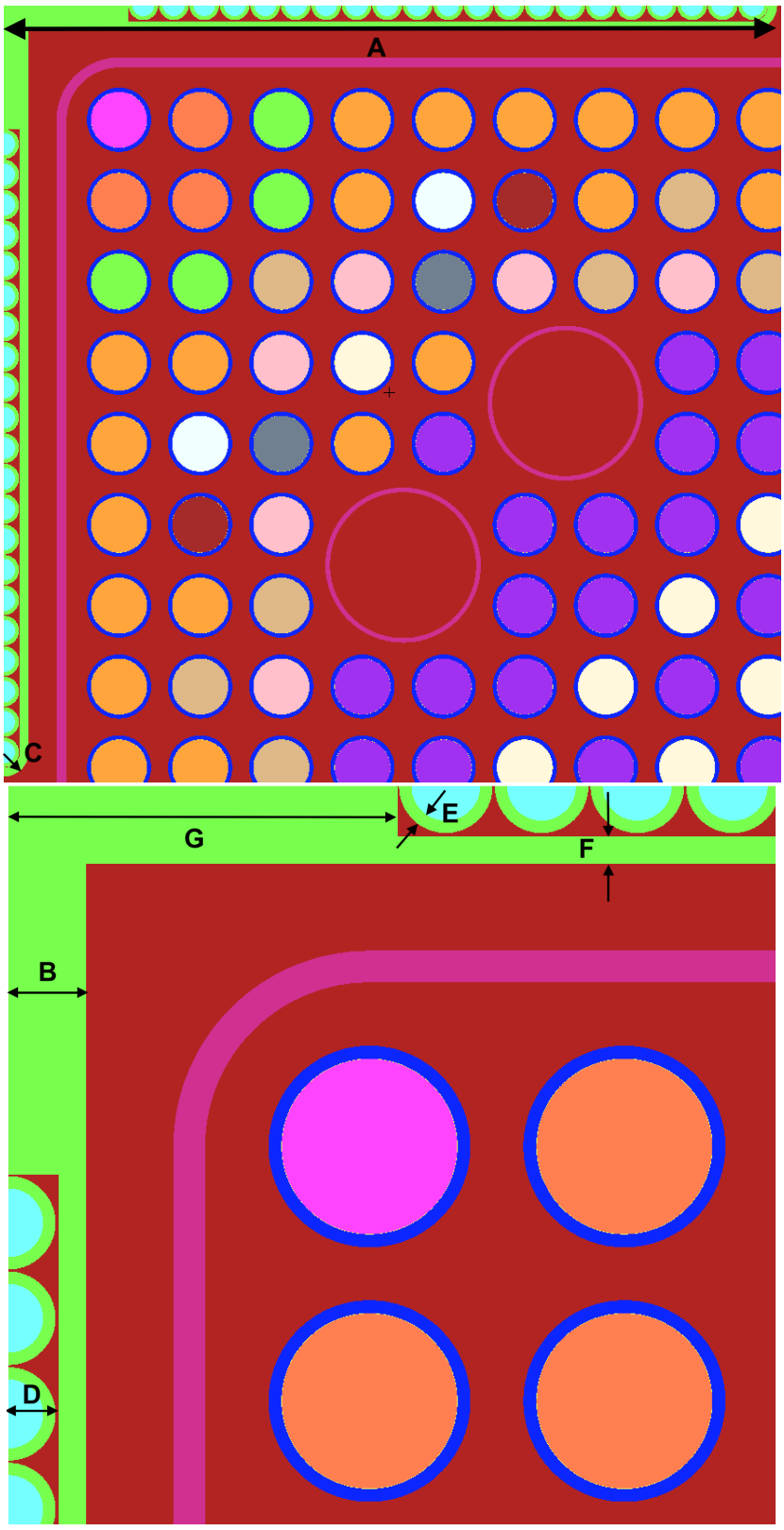

Figure 12. Diagram of control blade used in all controlled models (dimensions can be found in Table 6 from Solius *et al* [2001].

1.5 Summary

The design of BWR bundles and control elements can lead to highly nonuniform radial void distributions. The most accurate method for modeling BWRs would be to explicitly consider the radial void distributions inside each BWR bundle. The work in this report aims to determine how sensitive neutronics models are to the following factors:

1. The use of a uniform void instead of a radial void distribution
2. The use of pin-centered moderator channels in neutronics models instead of coolant-centered channels with thermal-hydraulic calculations performed with coolant-centered channels
3. The inclusion of annular flow into neutronics models

Furthermore, the sensitivity of control blade absorption rates and depletion to item 1 listed above list is analyzed. Void distributions from CTF were implemented in MCNP neutronics models of 1 cm slices of controlled and uncontrolled GE9 and GE14 bundles. The findings will be used to inform improvements to BWR models in VERA.

2 Results

2.1 Methodology

All MCNP models were run with fuel temperatures of 900 K, and temperatures for all other materials were set to 600 K. The default MCNP cross section libraries provide data at only a few temperatures, including: 293.6, 600, 900, and 1,200 K. Parameters for a generic BWR model are offered in Covington and Gheorghiu [1999] and suggest a saturation temperature for the coolant to be 560 K and an average fuel temperature of 813.6 K at nominal hot full power (HFP) conditions. The channel box, water rods, control blades, and cladding are immersed in the coolant and thus will be at a similar temperature. Based on these nominal temperatures, all coolant and structural materials (besides the UO_2 fuel) were set to a temperature of 600 K, which is reasonably close to the temperatures at HFP conditions, thus allowing the use of the default MCNP cross section libraries. For the fuel, the closest available temperature to the suggested average is 900 K. This is slightly high, but it allows for the use of the default cross section data and will likely not have a significant impact on the differences between cases, because all runs will be consistently using this temperature.

All GE9 and GE14 cases used 500,000 particles per cycle with 2,700 active cycles, with the exception of the control blade depletion calculations presented in subsection 2.5, which used 160,000 particles per cycle and 2,750 active cycles. This reduction in particle count was made because when control blades are depleted, 18 MCNP models must be run for each test case. These models correspond to 18 three-month time-steps over which the control blades are depleted, and higher particle counts would require a much larger computational budget.

In both the GE9 bundle and GE14 bundle, 3 axial levels were selected from which to obtain radial void distributions from the CTF results; these were always at the bottom of the bundle, the top of

the bundle, and one axial level above the bottom fifth but below the bottom half of the bundle. As presented, these axial locations can be recognized by increasing the bundle average void.

In all cases, the fission rates obtained from MCNP were normalized such that the average was one. The percent differences in fission rates were then calculated as follows:

$$\Delta P_{i,j} = \left(P^x_{i,j} - P^y_{i,j} \right) \times 100, \tag{6}$$

and the eigenvalue differences were determined according to the following:

$$\Delta k = (k_x - k_y) \times 10^5 \,\text{pcm}, \tag{7}$$

where $P^x_{i,j}$ is the normalized fission rate in the (i,j) fuel pin for case x. Likewise, k_x is the eigenvalue found for case x. For example, in subsection 2.2, the sensitivity of neutronics calculations to the use of a uniform radial void is considered, so throughout the section, case x is the case using a uniform radial void distribution at the bundle average void, and case y is the case using a radial void distribution from CTF.

Additionally, the root mean square (RMSs) of the differences in normalized fission rates for each case are presented in Table 8, Table 10, and Table 12. The RMS values are calculated using the following formula:

$$RMS = \left[\frac{1}{N_{pin}} \sum_j \sum_i \left(\Delta P_{i,j} \right)^2 \right]^{1/2}, \tag{8}$$

where N_{pin} is the total number of fuel pins in the fuel bundle.

2.2 Bundle Average Void Approximation in BWR Models

Table 7 presents the difference in k_{eff} for all bundle average cases considered. The lattice or bundle average void for the radial void distribution in each case is provided and was calculated using Equation 2. Additionally, the area weighted standard deviation of the void distribution used in each case is provided. The standard deviations were calculated using Equation 9, where i is the channel index, N is the number of channels, A_i is the flow area of channel i, α_i is the void fraction in channel i, and α_{bun} is the bundle average void. The largest differences are not seen in the top or bottom of the bundle, but they are seen in the cases using void distributions obtained from the bottom half of the CTF distribution.

$$\sigma_{void} = \left[\frac{1}{\sum_i^N A_i} \sum_i^N A_i \left(\alpha_i - \alpha_{bun} \right)^2 \right]^{\frac{1}{2}}. \tag{9}$$

This standard deviation is not intended to be used to measure error, but instead is only used as a metric for the spread in a given radial void distribution.

In this section, results from cases using a radial void distribution are labeled ctf, and results found using a uniform void distribution at the bundle average void are marked bun.

Table 7. Δk between MCNP cases using a bundle average void (bun) and MCNP cases using a CTF radial void distribution (ctf) (The error in all eigenvalues reported by MCNP was 2 pcm)

Bundle type	Lattice average void [%]	Standard deviation of the Void [%]	k_{ctf}	$k_{bun} - k_{ctf}$ [pcm]
Controlled GE9	1.0	0.70	0.84310	51.0
	36.5	12.28	0.78954	1206.0
	81.4	5.30	0.71936	819.0
Uncontrolled GE9	0.9	0.43	1.08611	26.0
	36.9	7.73	1.06562	569.0
	81.6	2.71	1.03345	190.0
Controlled GE14	1.1	1.33	0.81732	126.0
	28.3	17.21	0.77732	1881.0
	80.3	8.35	0.73273	1333.0
Uncontrolled GE14	0.6	0.63	0.99313	37.0
	29.4	9.89	0.97308	804.0
	80.9	1.63	0.94981	143.0

Generally, larger differences were seen in the GE14 cases than in the GE9 cases, indicating that the bundle design plays a role in the sensitivity of k_{eff} to a bundle average void. The largest difference found was an 1,881 pcm increase in the eigenvalue when using a bundle average void. This was in the case of a controlled GE14 bundle. The insertion of a control rod leads to a greater standard deviation in the radial void and corresponds to the larger differences in eigenvalue. These patterns were also witnessed in the maximum and minimum pin power differences as a result of the bundle average void approximation, which can be seen in Table 8. Figures showing pin powers from the most limiting cases for each bundle type are shown in the following pages. For cases not found to be the most limiting, the pin powers and pin power differences can be found in section E.

The differences have been plotted against both bundle average void (Figure 13) and standard deviation in the radial void profile (Figure 14). The two plots show that the standard deviation in the void is a better gauge for how large the differences will be as a result of the use of a bundle average void. As bundle average void increases past a certain point, the standard deviation of the void begins to decrease, and with it, the error incurred by using a uniform void distribution also decreases.

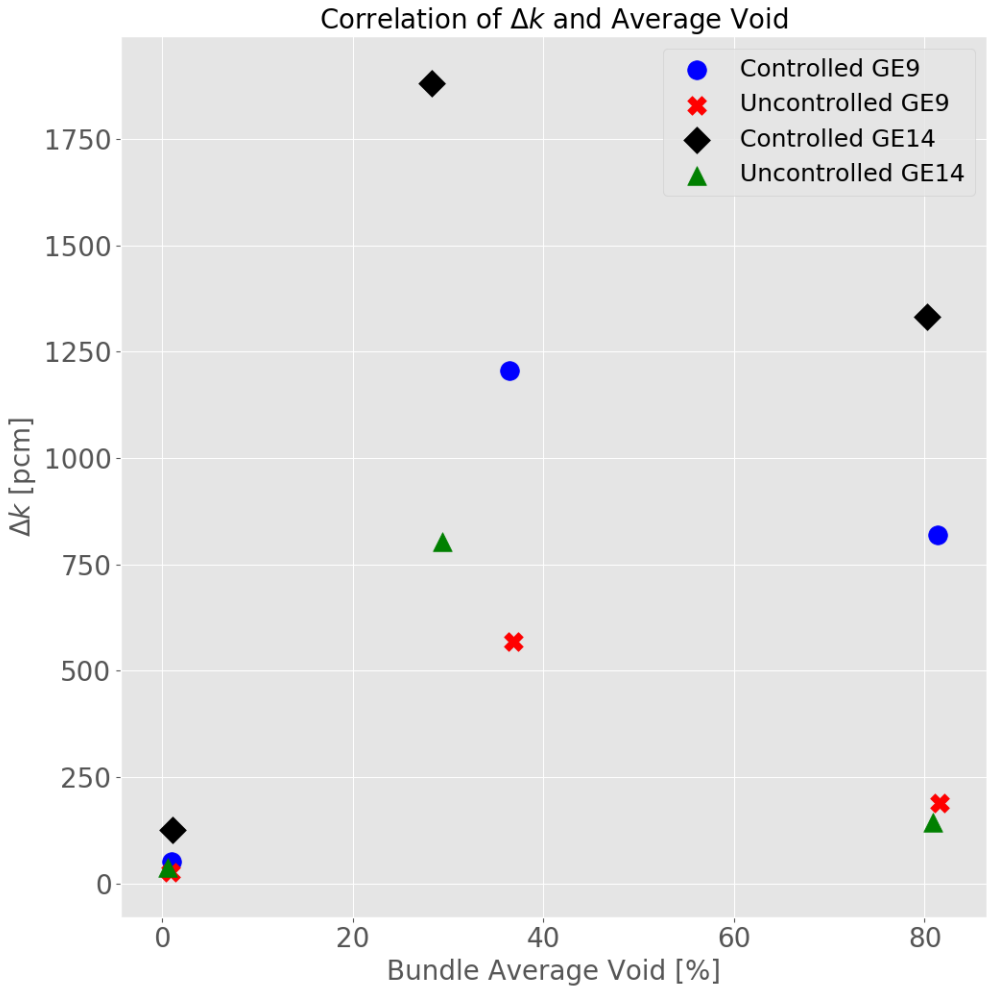

Figure 13. Difference in eigenvalue as a function of lattice average void.

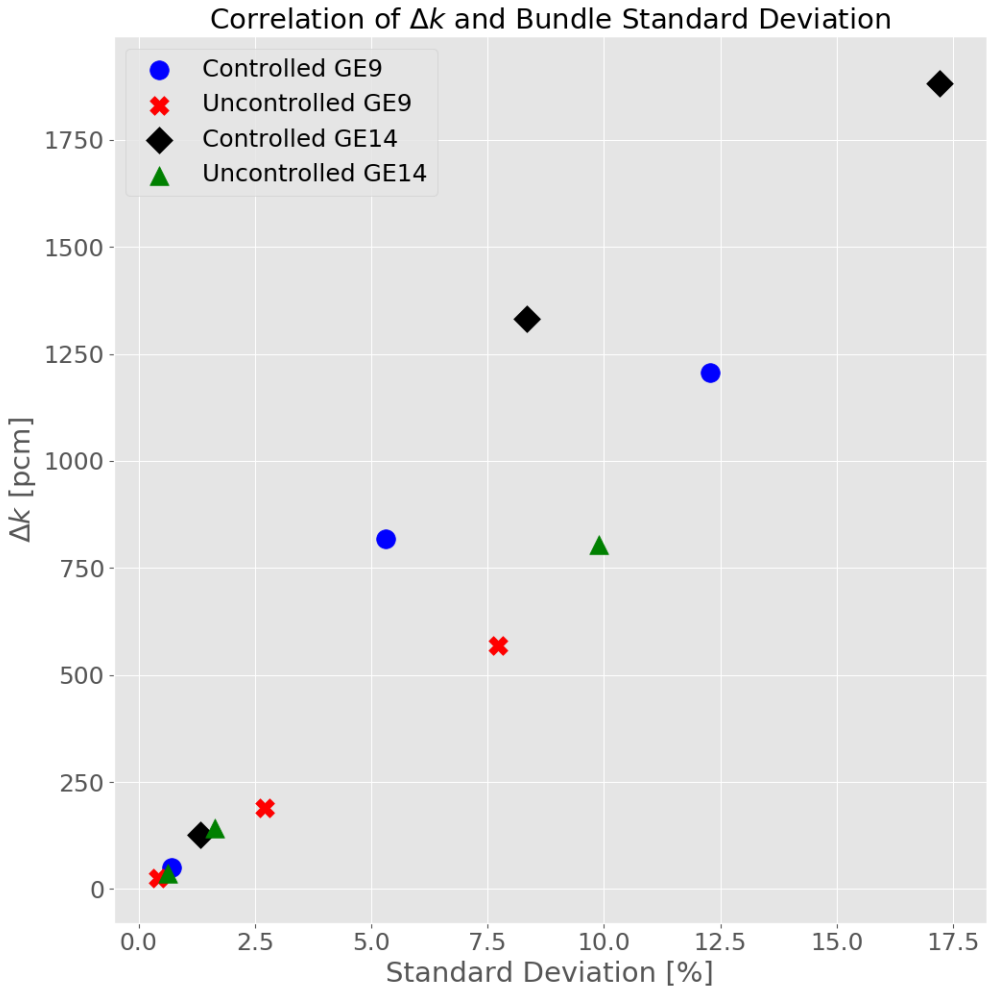

Figure 14. Difference in eigenvalue as a function of lattice void standard deviation.

According to Figure 14, the higher the spread of the radial void distribution, the more inaccurate the results will be from the use of a uniform void. This correlation supports the concept that controlled cases having a larger sensitivity to uniform void as the void distributions in controlled cases will have a larger standard deviation in channel voids.

2.2.1 Differences in Normalized Fission Rates

The maximum variance of any normalized fission rate for the cases run when investigating the sensitivity of neutronics models to bundle average was 0.03%.

Table 8. Maximum, minimum, and RMS difference in normalized fission rates between MCNP cases using a bundle average void (bun) and MCNP cases using a CTF radial void distribution (ctf) (The largest variance reported for any pin in any case was 0.03%)

Bundle type	Lattice average void [%]	Standard deviation of the void [%]	RMS [%]	$P_{i,j}^{bun}$-$P_{i,j}^{ctf}$ Max. [%]	Min. [%]
Controlled GE9	1.0	0.70	0.41	1.1	-0.6
	36.5	12.28	7.55	17.6	-12.5
	81.4	5.30	4.58	11.9	-6.5
Uncontrolled GE9	0.9	0.43	0.17	0.3	-0.4
	36.9	7.73	3.81	5.2	-7.1
	81.6	2.71	2.08	3.6	-4.5
Controlled GE14	1.1	1.33	0.80	3.0	-0.9
	28.3	17.21	10.66	29.5	-14.8
	80.3	8.35	6.80	21.1	-9.8
Uncontrolled GE14	0.6	0.63	0.24	0.6	-0.5
	29.4	9.89	3.76	7.3	-10.5
	80.9	1.63	0.73	1.7	-1.9

Again, GE14 bundles and controlled cases have the larger errors. This applies to larger maximums and lower (more negative) minimums. As expected, the largest difference is in the case of the controlled GE14 bundle, which had an increase of up to 29.5% in the most limiting fuel pin. Even in uncontrolled cases, pin power increases of up to 5% and decreases of 7% were observed.

The following plots show normalized fission rates from the two MCNP cases that were run for each test (top two plots); the difference in fission rates is shown on the bottom left of each figure, and the void distribution from CTF is included on the bottom right. The void distribution is provided as it is found in CTF, so it is on a coolant-centered channel basis.

2.2.1.1 Controlled GE9

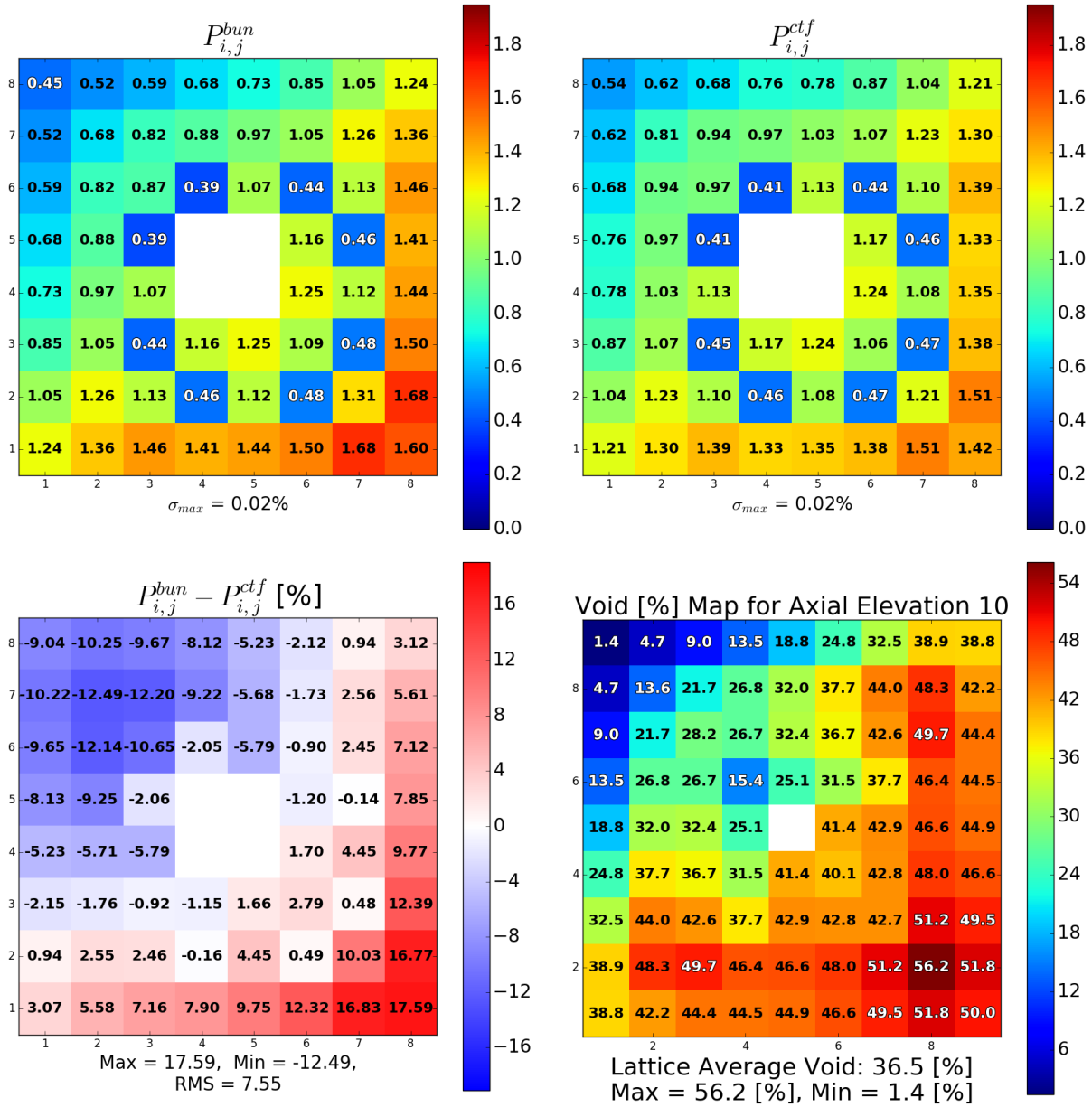

Figure 15. Comparison of normalized fission rates for the most limiting void distribution considered for a controlled GE9 bundle in the bundle average void test.

2.2.1.2 Uncontrolled GE9

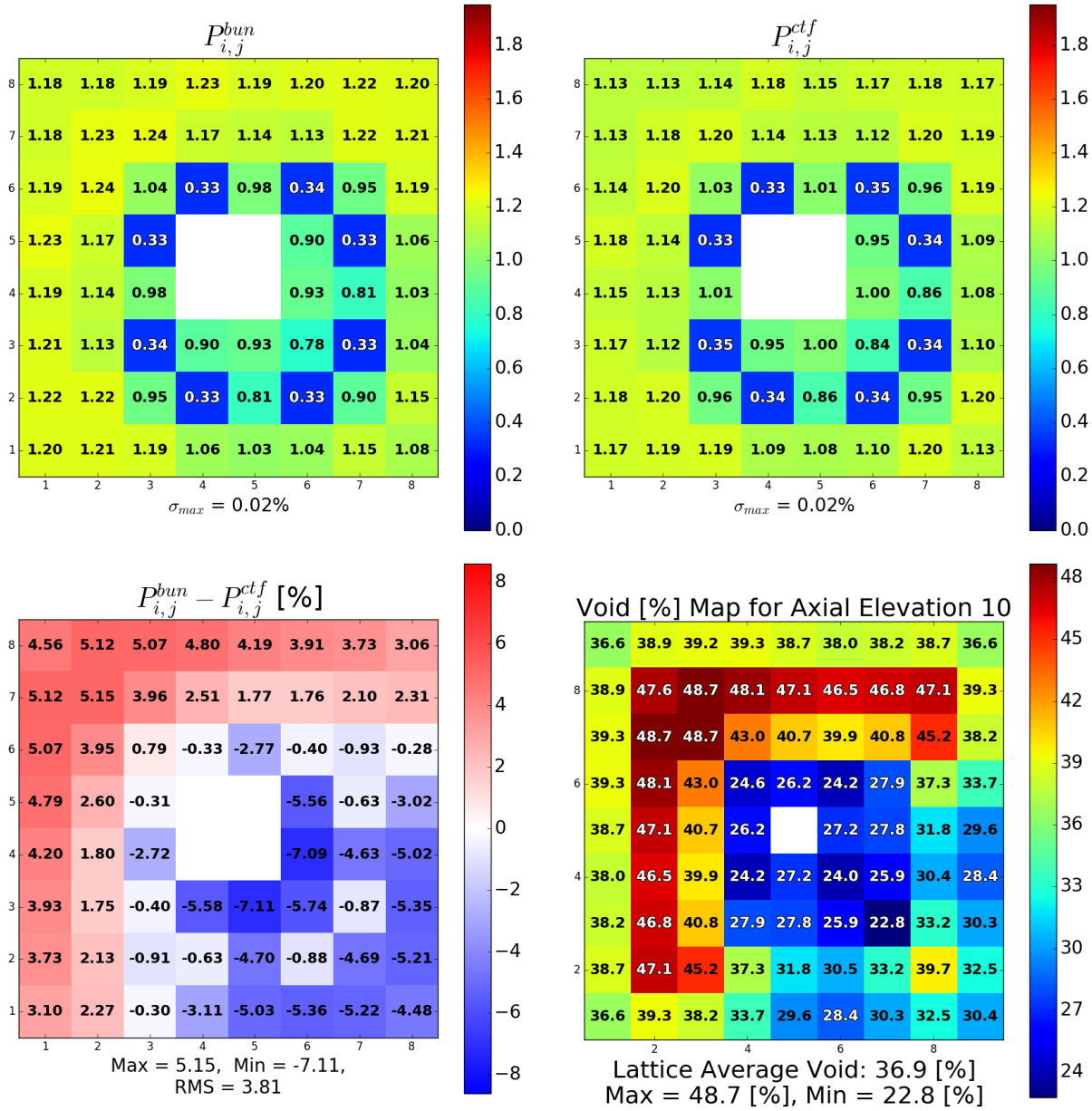

Figure 16. Comparison of normalized fission rates for the most limiting void distribution considered for an uncontrolled GE9 bundle in the bundle average void test.

2.2.1.3 Controlled GE14

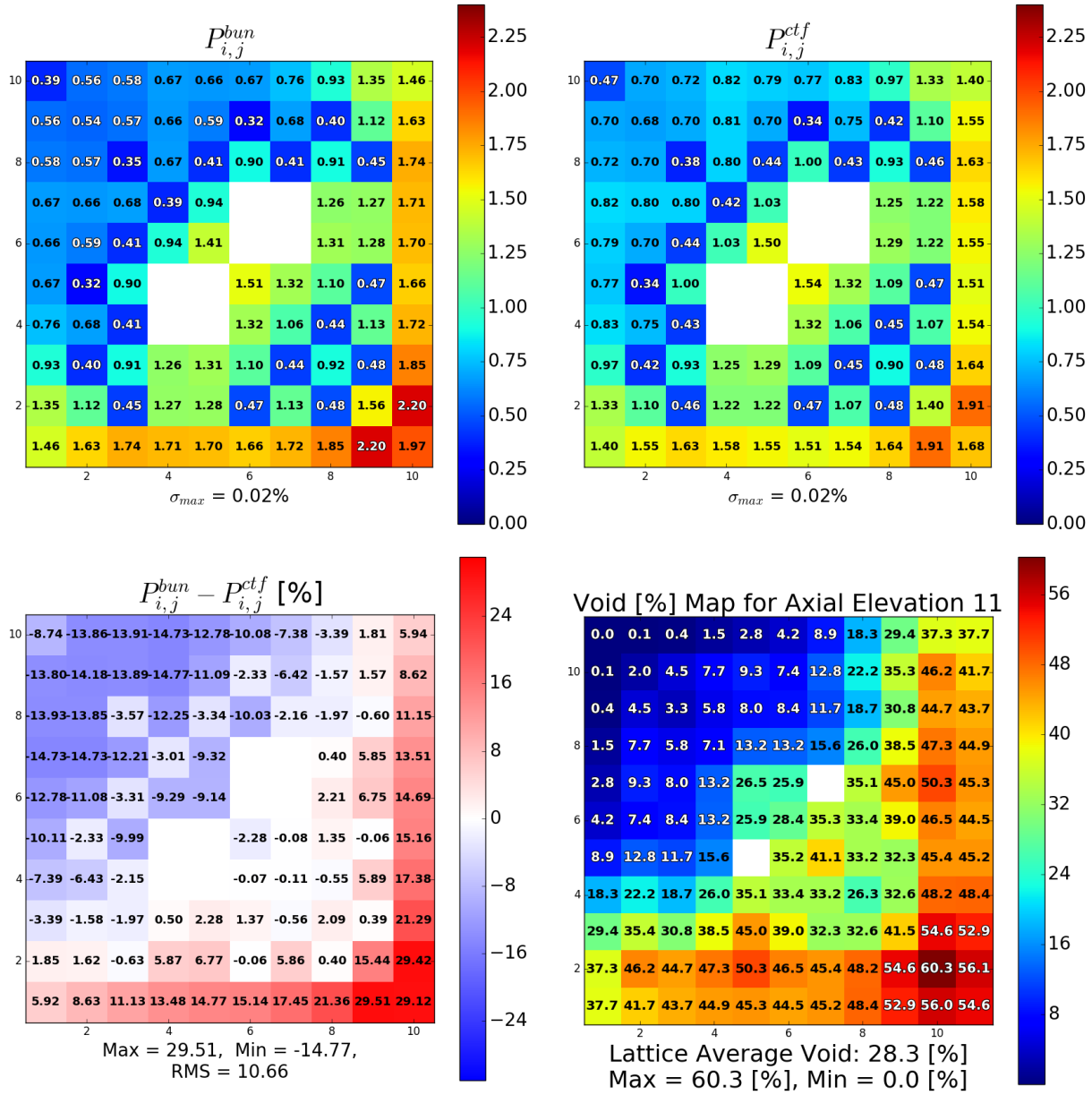

Figure 17. Comparison of normalized fission rates for the most limiting void distribution considered for a controlled GE14 bundle in the bundle average void test.

2.2.1.4 Uncontrolled GE14

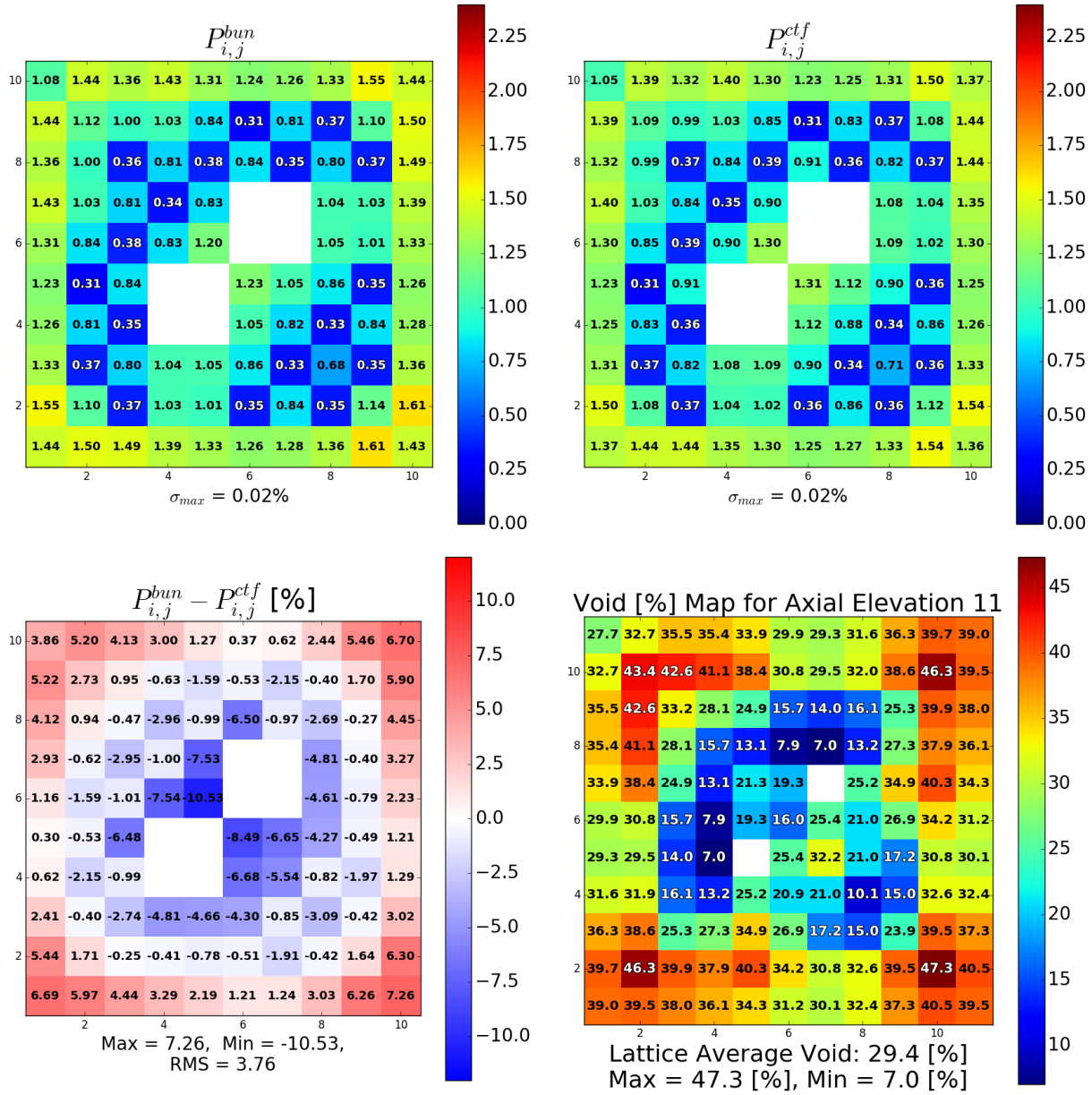

Figure 18. Comparison of normalized fission rates for the most limiting void distribution considered for an uncontrolled GE14 bundle in the bundle average void test.

According to the data shown in Figure 15, the use of a bundle average uniform void instead of a radial void distribution from CTF in a controlled case leads to a dip in pin powers in the corner where the control blade sits, and it pushes power towards the corner, away from the control blade. In Figure 16, there is no control blade present, so the largest nonfission absorption is coming from fuel pins which include gadolinium. In this case, the use of a bundle average void pushes power away from the gadolinium pins, which can be located using the low pin powers in Figure 16.

Similar patterns are seen in Figure 17 and Figure 18. Notice that although the bundle average void of the GE14 cases is lower than those seen in the GE9 cases, the spread of the void distributions is more dramatic.

In all cases, comparison of the radial void distribution with the differences caused by using a uniform void shows that for pins where void is lower, a uniform void at the bundle average will cause a lower pin power. When the void distribution is averaged, the total mass of moderator within the bundle is smeared across the bundle. This means that in locations where void was low in the radial distribution, the bundle average void will lead to increased void and thus decreased moderator density. The decrease in moderator density leads to decreased neutron thermalization and lower fission rates. The opposite effect occurs for pins near high void fractions, where the bundle average void will act to bring the void fraction down and will smear extra moderator into channels surrounding these pins, thus allowing for more neutron thermalization and more fission.

In general, for cases in which strong absorbers such as control blades exist in BWR bundles, void will be lower as a result of lower fission rates. The use of a bundle average void artificially raises the void near control elements, so it pushes power away from these locations. This means that more fission occurs away from absorbers, so less neutrons are available near burnable poisons and the control elements to be absorbed by them. Shifting neutron flux away from burnable absorbers and control blades in this manner will lead to a higher eigenvalue and will essentially lower the average absorption cross section in the system.

2.3 Pin Centered Channels in Neutronics Calculations

The differences in eigenvalues of cases using coolant-centered channels and pin-centered channels are shown in Table 9. When setting up pin-centered channel cases, the coolant-centered channel void distribution for each case is mapped into pin-centered channel voids using Equation 4.

Generally, GE14 bundles are more sensitive to the use of pin-centered channels, although this trend is not as noticeable as in the bundle average void tests. Additionally, when a control blade is present, the sensitivity to pin-centered channels decreases. In all cases, the use of pin-centered channels leads to an overestimation of the eigenvalue.

In this section, results marked with *mod* are those found using a radial void distribution in the coolant-centered channel, and results marked *pin* are those found using a radial void distribution that has been mapped into pin-centered channels.

Table 9. Δk between MCNP cases using a void distribution averaged into pin-centered channels (pin) and MCNP cases using a CTF radial void distribution in coolant-centered channels (mod). The error in all eigenvalues reported by MCNP was 2 pcm.

Bundle type	Lattice average void [%]	Standard deviation of the void [%]	k_{pin}	$k_{mod} - k_{pin}$ [pcm]
Controlled GE9	1.0	0.70	0.84318	-8.0
	36.5	12.28	0.79123	-169.0
	81.4	5.30	0.71993	-57.0
Uncontrolled GE9	0.9	0.43	1.08621	-10.0
	36.9	7.73	1.06755	-193.0
	81.6	2.71	1.03391	-46.0
Controlled GE14	1.1	1.33	0.81753	-21.0
	28.3	17.21	0.77901	-169.0
	80.3	8.35	0.73357	-84.0
Uncontrolled GE14	0.6	0.63	0.99330	-17.0
	29.4	9.89	0.97539	-231.0
	80.9	1.63	0.95031	-50.0

2.3.1 Differences in Normalized Fission Rates

Pin powers are far less sensitive to the use of pin-centered channels than they were to bundle average void, but this is no surprise, because when the void distribution is mapped to pin-centered channels, averaging is taking place over smaller areas instead of over the entire bundle. However, in the uncontrolled cases, pin power decreases of up to 1.2% were found when using pin-centered channels, and such differences are not insignificant.

Table 10. Maximum, minimum, and RMS difference in normalized fission rates between MCNP cases using a void distribution averaged into pin-centered channels (*pin*) and MCNP cases using a CTF radial void distribution in coolant-centered channels (*mod*) (The largest variance reported for any pin in any case was 0.02%)

Bundle type	Lattice average void [%]	Standard deviation of the void [%]	RMS [%]	$P_{i,j}^{mod}$-$P_{i,j}^{pin}$ Max. [%]	Min. [%]
Controlled GE9	1.0	0.70	0.04	0.1	-0.1
	36.5	12.28	0.35	0.8	-0.7
	81.4	5.30	0.23	0.4	-0.6
Uncontrolled GE9	0.9	0.43	0.03	0.1	-0.1
	36.9	7.73	0.47	1.2	-0.6
	81.6	2.71	0.21	0.4	-0.4
Controlled GE14	1.1	1.33	0.09	0.2	-0.4
	28.3	17.21	0.49	0.8	-1.4
	80.3	8.35	0.31	0.4	-1.0
Uncontrolled GE14	0.6	0.63	0.05	0.1	-0.2
	29.4	9.89	0.52	1.1	-1.0
	80.9	1.63	0.15	0.2	-0.4

The following plots show normalized fission rates from the two MCNP cases that were run for each test (top two plots). The difference in fission rates is shown in the center left of each figure, and the void distribution from CTF is located in the center right. The void distribution is provided as it is found in CTF, so it is on a coolant-centered channel basis. Additionally, the pin-centered channel void distributions are provided for comparison in the bottom plot of each figure.

2.3.1.1 Controlled GE9

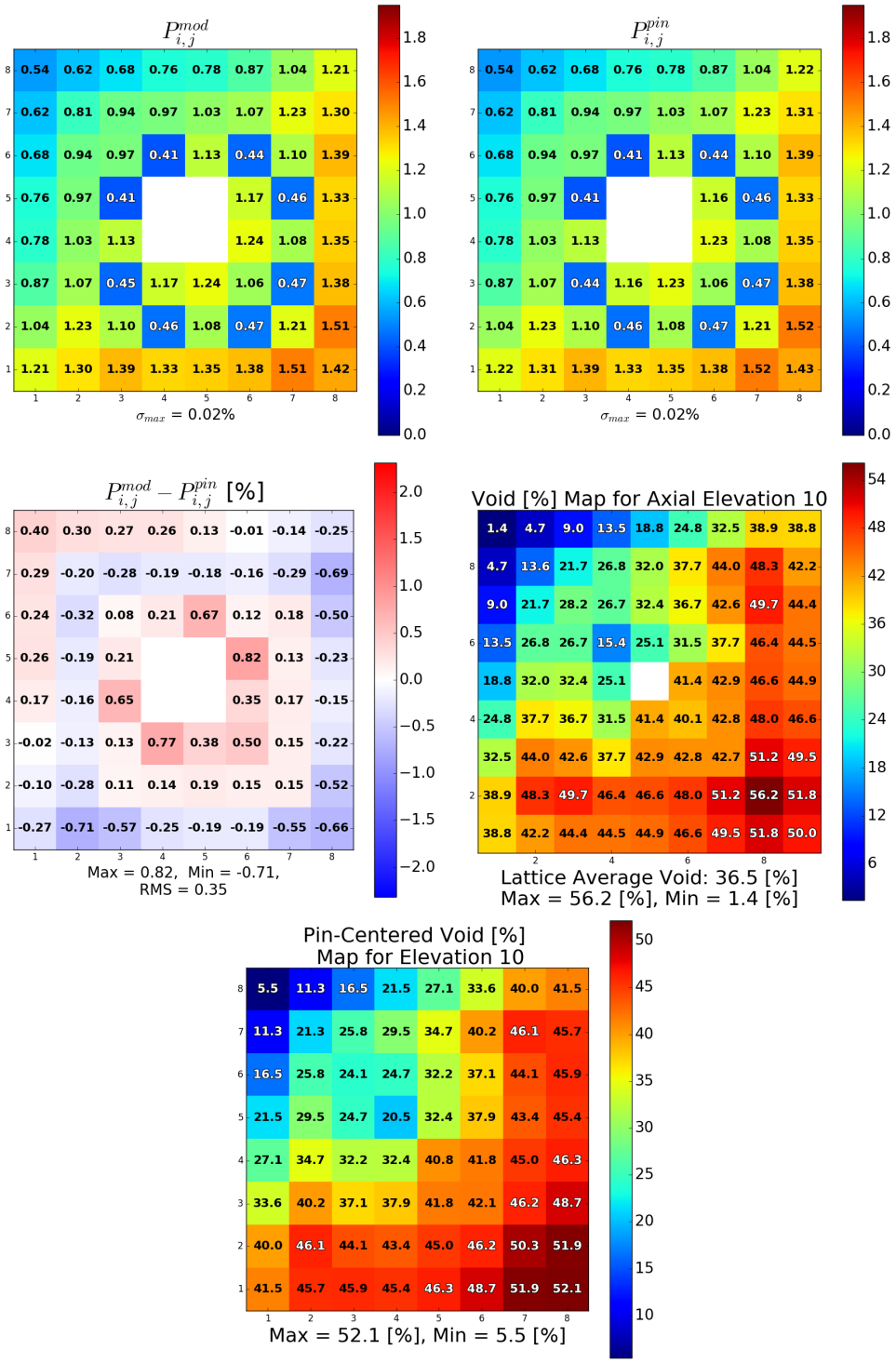

Figure 19. Comparison of normalized fission rates for most limiting void distribution considered for a controlled GE9 bundle in the pin-centered channel test.

2.3.1.2 Uncontrolled GE9

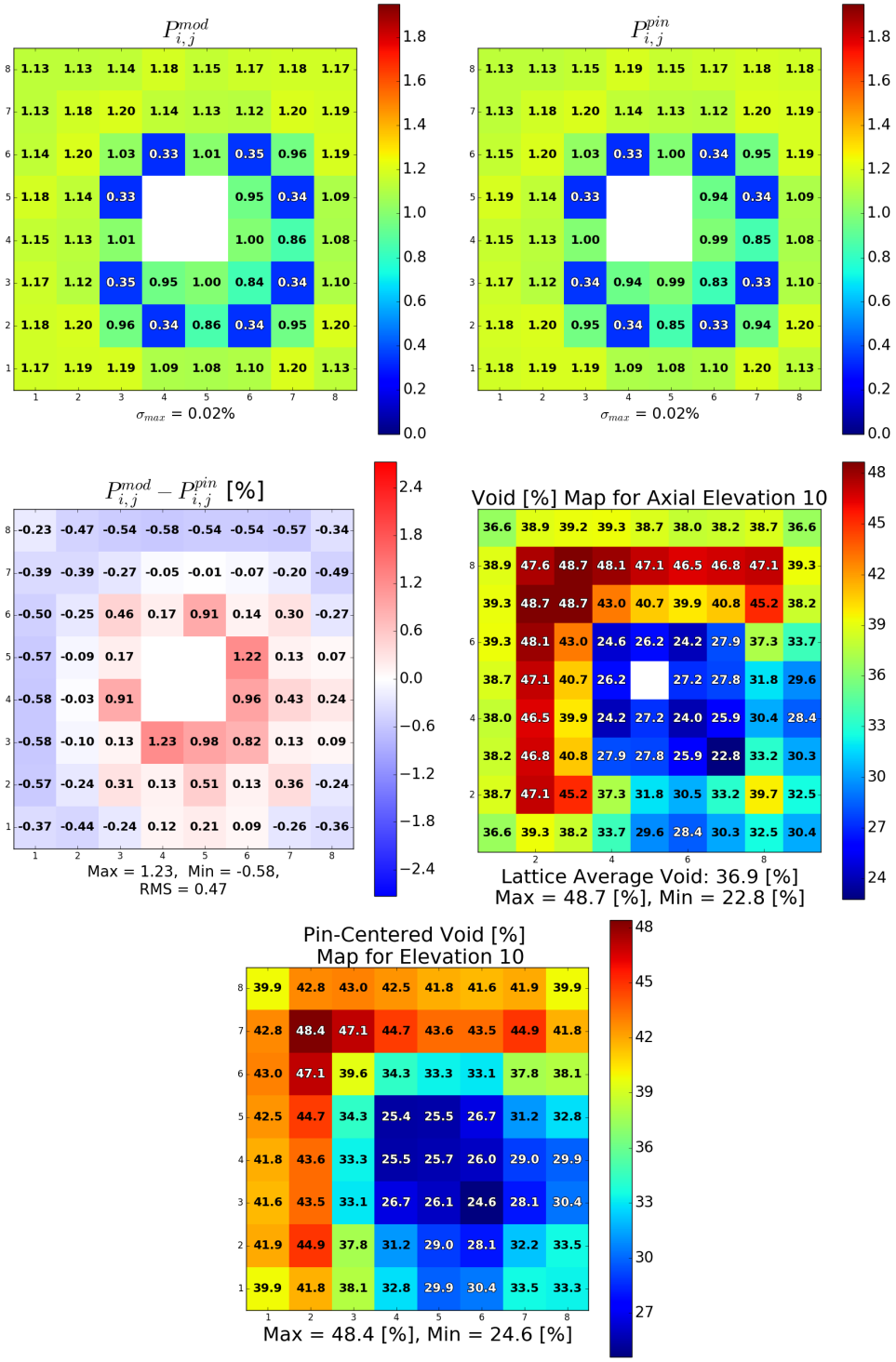

Figure 20. Comparison of normalized fission rates for most limiting void distribution considered for an uncontrolled GE9 bundle in the pin-centered channel test.

2.3.1.3 Controlled GE14

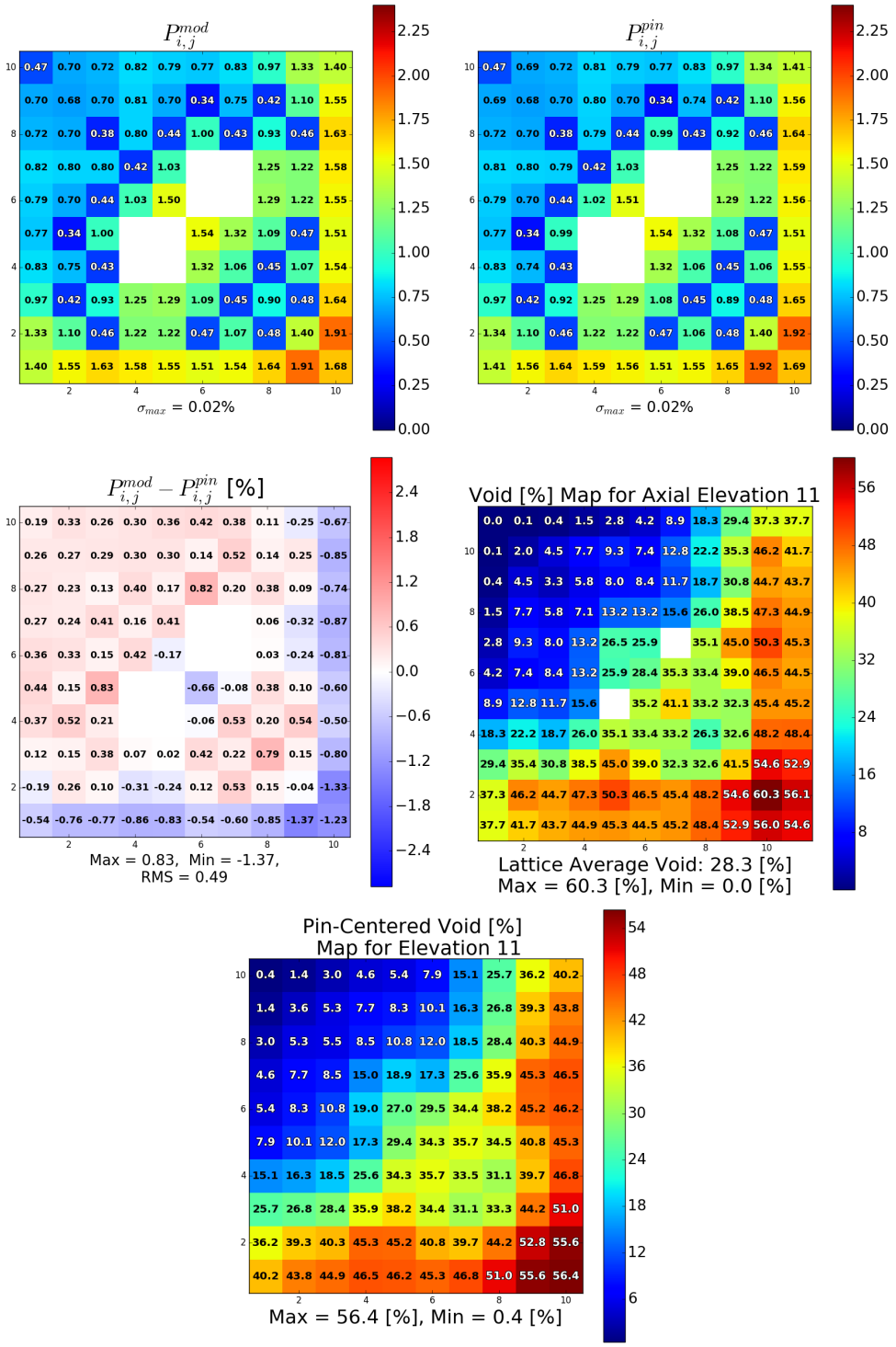

Figure 21. Comparison of normalized fission rates for most limiting void distribution considered for a controlled GE14 bundle in the pin-centered channel test.

2.3.1.4 Uncontrolled GE14

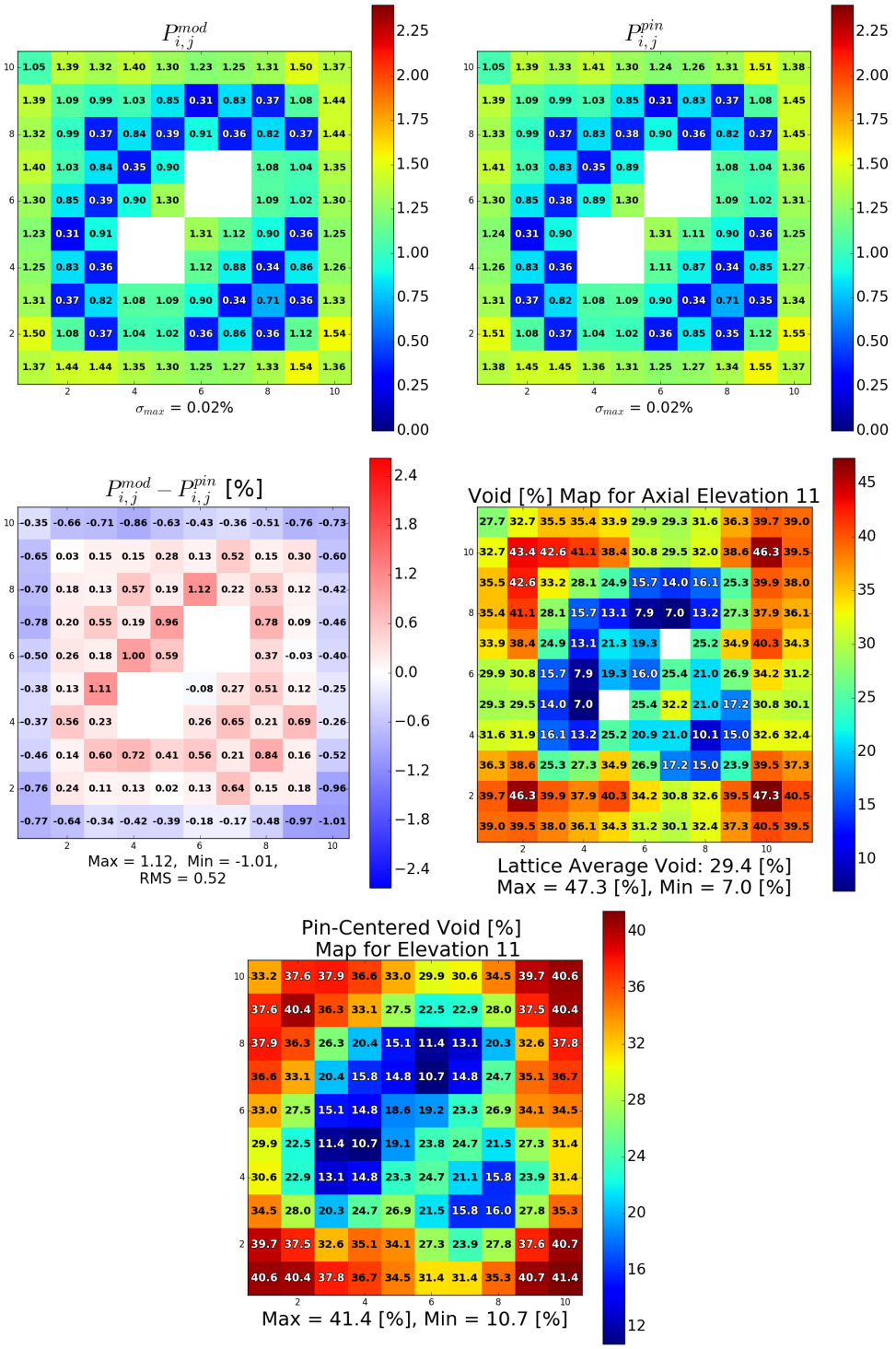

Figure 22. Comparison of normalized fission rates for most limiting void distribution considered for an uncontrolled GE14 bundle in the pin-centered channel test.

The differences in normalized fission rates in Figure 19 through Figure 22 show that in areas with lower pin powers such as gadolinium-containing fuel rods and their neighbors, the use of pin-centered channels decreases fission rates. The pin-centered channel averaging essentially behaves the same as when using a bundle average void, but on a smaller scale. When mapping coolant-centered channel voids to a pin-centered channel basis, the mass in each pin cell is preserved, but overall, the void becomes less distributed. This is most easily observed when looking at maximum and minimum voids for each case. In Figure 19, when on a coolant-centered basis, the maximum and minimum voids are 56.2 and 1.4%, but when averaged into pin-centered channels the maximum and minimum have become 52.1 and 5.5%. This occur in all four cases shown in this section.

In channels near gadolinium pins where the void is low, the averaging used to map data into pin-centered channels slightly increases void locally, which inserts negative reactivity. This reactivity insertion is most noticeable in fission rates in fuel pins adjacent to gadolinium pins. In hotter pins, the void is higher, and the use of pin-centered channels leads to slightly increased fission rates caused by the positive reactivity inserted when the pin-centered averaging acts to locally push a slight amount of void away.

Although the use of pin-centered channels does not change the overall void or moderator mass in a bundle, it does slightly smooth the distribution. In turn, this smoothing of the void distribution leads to a slight exaggeration of fission rates. That is, using pin-centered channels will push low pin powers lower and high pin powers higher. From Figure 19 through Figure 22, it appears that the effect is more noticeable in bundles containing gadolinium rods when they are not exposed to a control blade.

2.4 Neutronic Calculation Sensitivity to Annular Flow Geometry

When setting up the annular cases, the methods described in subsubsection 1.2.3 are used to determine cell sizes of vapor cells within coolant-centered channels. In these inputs, in channels with void fractions above 20%, the moderator is assumed to have a saturated liquid region located around the fuel pins and a saturated vapor region in the center of the channels. The results from these cases are compared to simply using the coolant-centered channel void distribution and modeling all channels as a saturated mixture. The equations used to calculate the sizes of the vapor cells are shown in section A.

In this section, anu represents data calculated with annular flow, and ctf represents data calculated using a saturated mixture in all channels. Note that there are now only two cases for each bundle type. When setting up annular flow inputs, all channels in the cases for the bottoms of the BWR bundles were less than 20%, which indicates that they were still likely to be in a bubbly flow or a saturated mixture regime and would revert back to simply using the saturated mixture representation. This results in identical inputs for the bottom of the assembly; therefore, no difference would occur because of the annular flow in these cases, so they have been excluded.

Table 11. Δk between MCNP cases using annular flow (anu) and MCNP cases using a CTF radial void distribution in coolant-centered channels (ctf) (The error in all eigenvalues reported by MCNP was 2 pcm)

Bundle type	Lattice average void [%]	Standard deviation of the void [%]	k_{ctf}	$k_{anu} - k_{ctf}$ [pcm]
Controlled GE9	36.5	12.28	0.78954	58.0
	81.4	5.30	0.71936	38.0
Uncontrolled GE9	36.9	7.73	1.06562	69.0
	81.6	2.71	1.03345	41.0
Controlled GE14	28.3	17.21	0.77732	80.0
	80.3	8.35	0.73273	77.0
Uncontrolled GE14	29.4	9.89	0.97308	-43.0
	80.9	1.63	0.94981	127.0

The sensitivity of the eigenvalue to annular flow is smaller than in the case of pin-centered channels or the bundle-averaged channels. The largest difference in this case is a 127 pcm increase when modeling annular flow. The maximum and minimum differences in fission rate from including annular flow in neutronics models are more noticeable than that seen for the use of pin-centered channels. In Table 12, fission rates are shown to increase by as much as 3% in the most limiting pins.

2.4.1 Differences in Normalized Fission Rates

Table 12. Maximum, minimum, and RMS difference in normalized fission rates between MCNP cases using annular flow (anu) and MCNP cases using a CTF radial void distribution in coolant-centered channels (ctf) (The largest variance reported for any pin in any case was 0.03%)

Bundle type	Lattice average void [%]	Standard deviation of the void [%]	RMS [%]	$P_{i,j}^{anu}$-$P_{i,j}^{ctf}$	
				Max. [%]	Min. [%]
Controlled GE9	36.5	12.28	0.91	3.0	-1.6
	81.4	5.30	0.53	1.9	-0.8
Uncontrolled GE9	36.9	7.73	0.85	2.4	-1.2
	81.6	2.71	0.55	1.9	-0.6
Controlled GE14	28.3	17.21	0.88	3.0	-1.4
	80.3	8.35	0.49	1.3	-1.0
Uncontrolled GE14	29.4	9.89	0.60	1.4	-1.1
	80.9	1.63	0.58	1.5	-0.7

The following plots show normalized fission rates from the two MCNP cases that were run for each test (top two plots). The difference in fission rates is shown in the bottom left of each figure, and

the void distribution from CTF is located in the bottom right. The void distribution is provided as it is found in CTF, so it is on a coolant-centered channel basis.

2.4.1.1 Controlled GE9

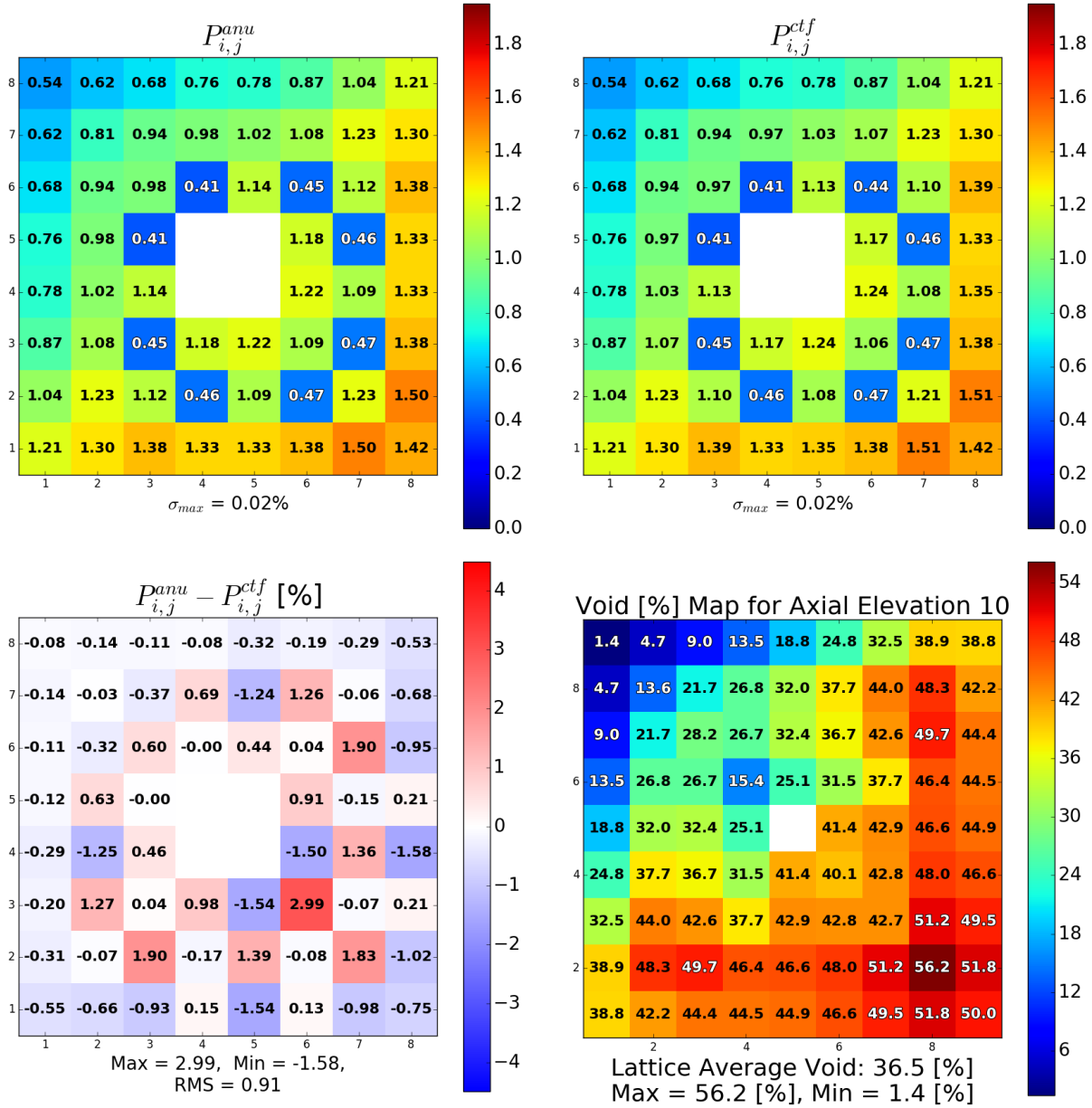

Figure 23. Comparison of normalized fission rates for the most limiting void distribution considered for a controlled GE9 bundle in the annular flow test.

2.4.1.2 Uncontrolled GE9

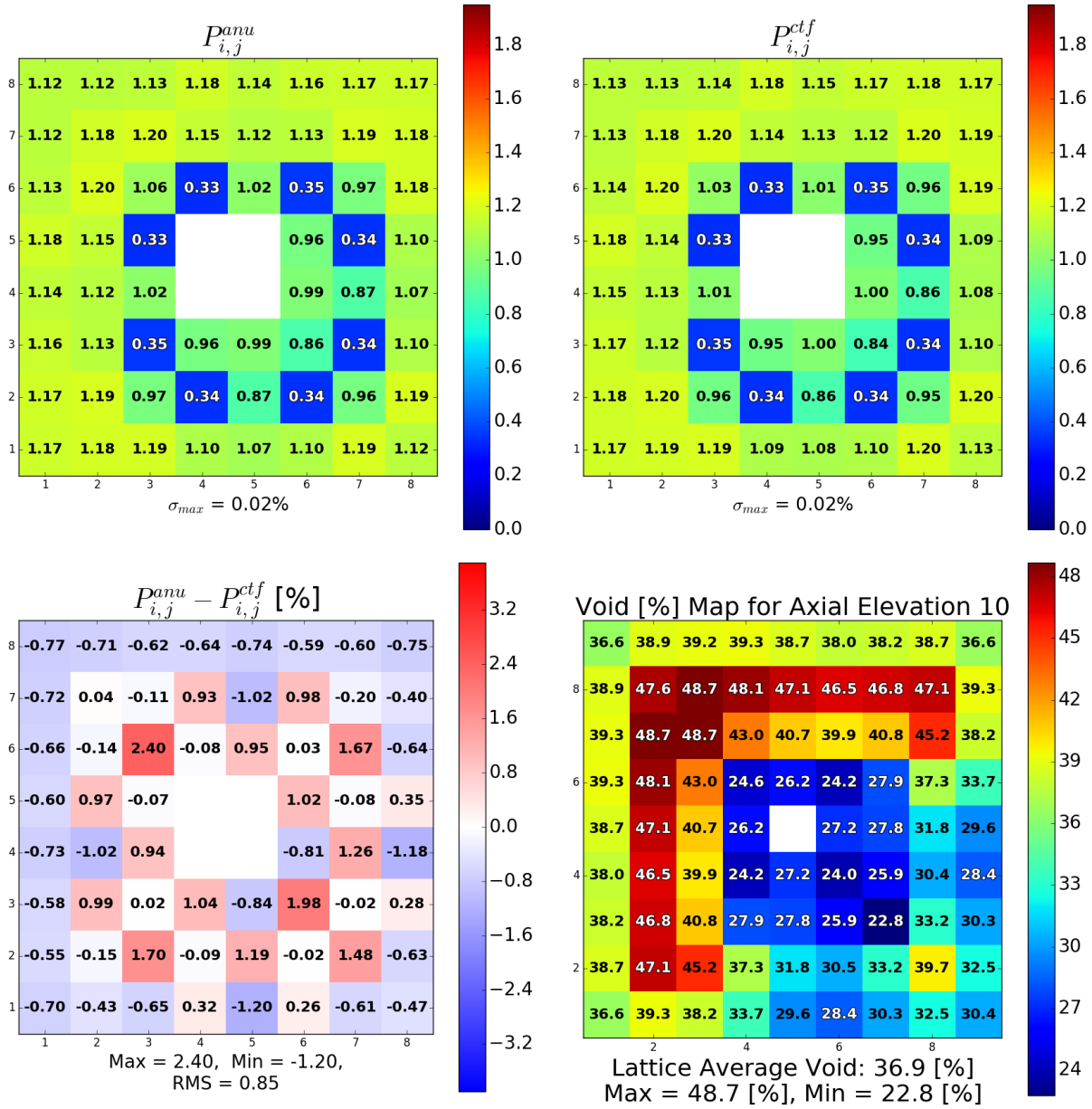

Figure 24. Comparison of normalized fission rates for the most limiting void distribution considered for an uncontrolled GE9 bundle in the annular flow test.

2.4.1.3 Controlled GE14

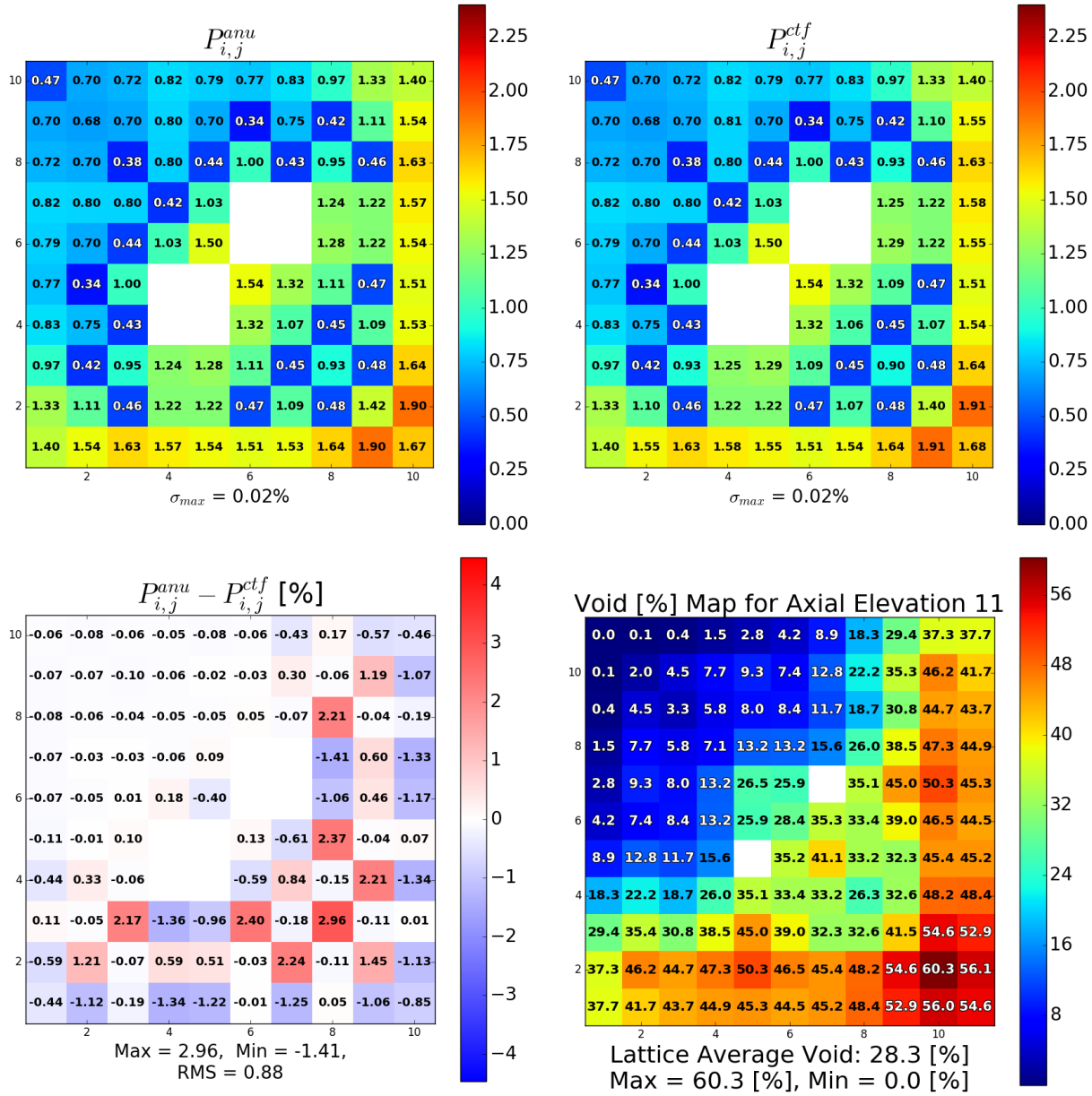

Figure 25. Comparison of normalized fission rates for the most limiting void distribution considered for a controlled GE14 bundle in the annular flow test.

2.4.1.4 Uncontrolled GE14

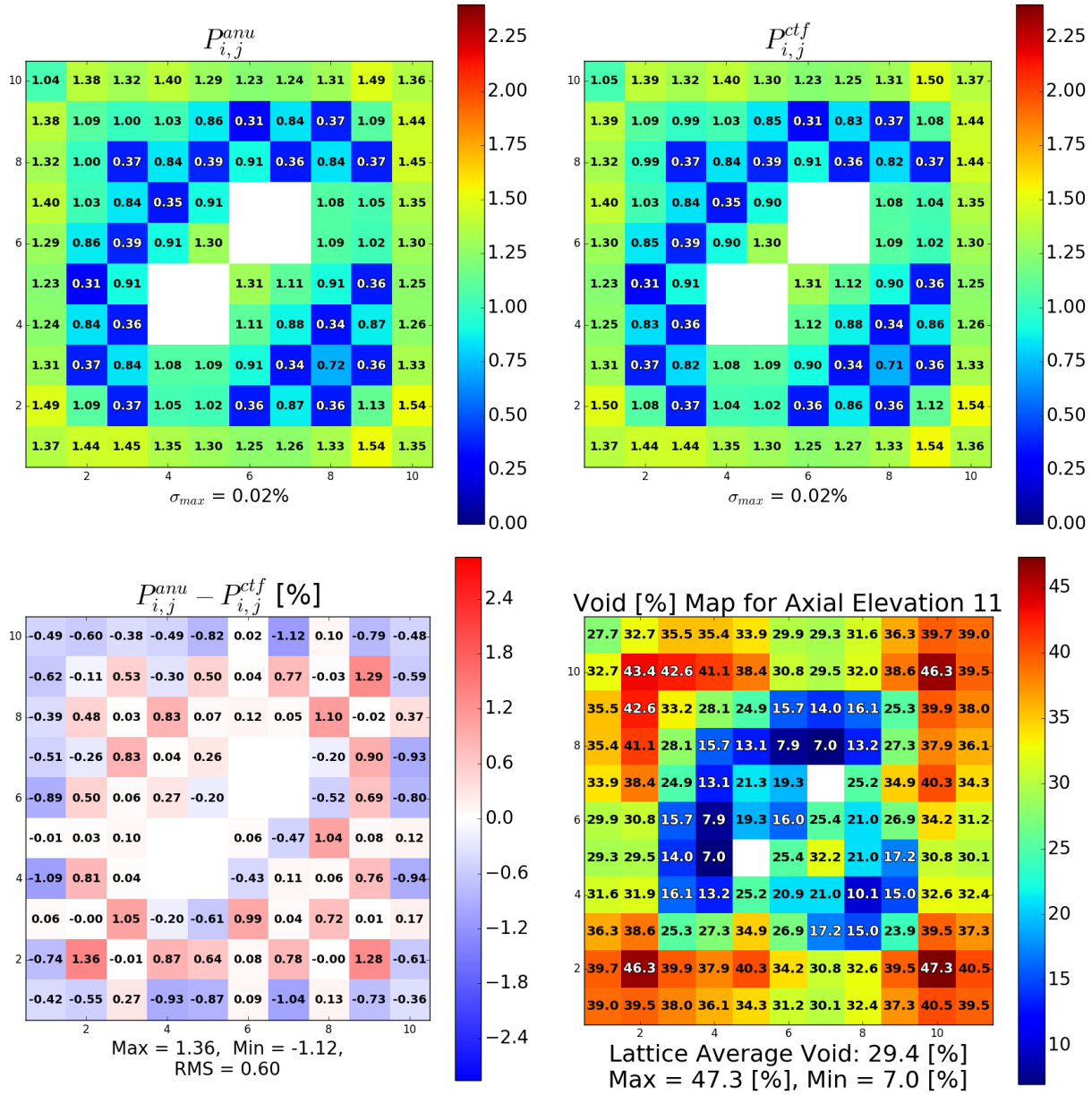

Figure 26. Comparison of normalized fission rates for the most limiting void distribution considered for an uncontrolled GE14 bundle in the annular flow test.

Figure 23 and Figure 24 show that in the case of the GE9 bundles, the insertion of a control blade does not shift the locations of pin power differences. The same pins which increase in power in the uncontrolled case (Figure 24) still increase in power when the control blade is inserted, but the increase in fission rate is redistributed among those same pins. This is still true in the GE14 cases. When comparing the differences in fission rates to those in the fission rate maps provided, it is clear that fission rates increase in the pins adjacent gadolinium-containing pins.

This is an interesting result, but it might be caused by some neutron streaming effects that are

mitigated when annular flow is approximated by a uniform saturated mixture in each channel. One likely cause of the increase in fission rates in pins that neighbor gadolinium-containing rods is that when annular flow is explicitly considered, there is a higher density of water molecules directly against the fuel pins, but the thickness of this film is much smaller than the mean free path of a neutron in an LWR. Because of this, it is more likely that a neutron leaving a gadolinium-containing pin will pass through the dense liquid film, and because everything else in the channel is saturated vapor with a much lower density, it is less likely that this neutron will scatter back into the gadolinium pin. Because the liquid film is so thin, it is not very likely that a neutron will interact with it, and because the liquid film is the result of the number density of hydrogen atoms being less concentrated in the center of the channel where the steam is, this neutron is less likely to change direction and go back into the gadolinium-containing pin. Therefore, when annular flow is considered, on average, more neutrons leave gadolinium pins and travel into the neighboring pins to cause fission instead of being scattered back into the gadolinium pin of origin where it could be absorbed by gadolinium instead of causing fission.

2.5 Control Blade Depletion Sensitivity to Bundle Average Void

In subsection 2.2, it was determined that the most severe difference in eigenvalue and pin power distribution resulting from the use of a bundle average void instead of a radial void distribution was in the case of a controlled GE14 bundle. Therefore, the GE14 bundle case was used to analyze sensitivity of absorption rates and depletion in control blades. The case considered was the case with a 28.3% average void. The process used to calculate absolute absorption rates in the control blade is described in subsection B.2. Essentially, a power density of 54 Kilowatts per liter (kW/L) is assumed in the bundle. This number is used to determine a renormalization factor for the MCNP tallies.

The plot presented in Figure 27 compares differences in absorption rates along the control blade wing from a case using a uniform void at the bundle average void and a case using a radial void distribution. This case was for a fresh control blade.

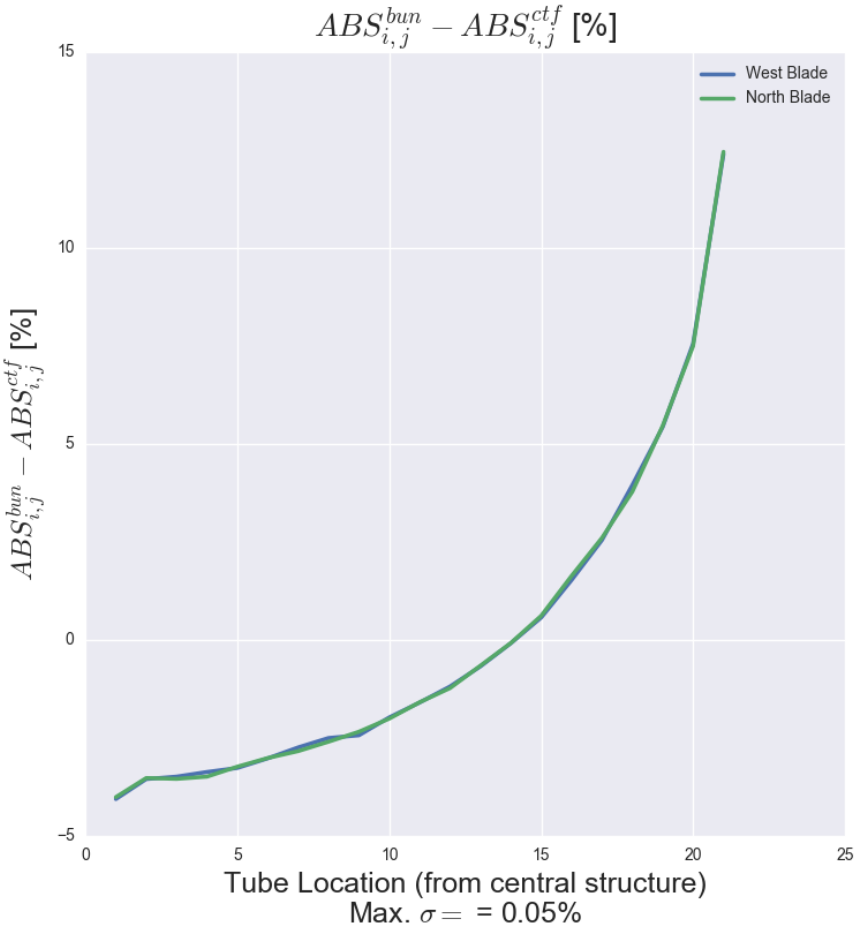

Figure 27. Relative difference in control blade tube absorption rates across the control blade caused by the use of a uniform void. The differences in this figure are for a GE14 bundle modeled with a CTF radial void distribution with an average void of 28.3% and a standard deviation of 17.21%. This is the case depicted in Figure 17 and is for fresh fuel and a fresh control blade.

In Figure 17, the corresponding differences in normalized fission rates for this case are shown. In pins in the NW corner of the bundle, the use of a bundle average void lead to decreased fission rates. In Figure 27, in the tubes closest to the NW corner, the absorption rate is lowered when using the bundle average void. It appears that lower fission rates lead to lower thermal flux in the nearby absorber tubes. However, moving along the wing from the north west corner to the wing tips, one also moves towards the east and south fuel pins. In these areas, fission rates were increased as a result of the use of a bundle average void, and correspondingly, the absorption rates in these tubes are higher by as much as 12% in the bundle averaged void case. From this it is clear that absorption rates in individual tubes are sensitive to the void distribution used. However, this does not directly indicate that the rate at which the control blade loses its overall reactivity worth will be sensitive.

Because the MCNP models used did not have explicit consideration of fuel depletion and had a constant power density with the control blade always inserted, it is difficult to gauge how quickly the control blade should deplete. Therefore, it is easier to measure "time" using the smeared thermal neutron fluence, SNVT, in units of 10^{21} $ntns/cm^2$ Kennard and Harbottle [2000]. Notice that this is a sextillion (S) $ntns/cm^2$, and "NVT" stands for $N \times v \times t$, where N is the number of neutrons, v is the neutron velocity, and t is time. This is a unit commonly used in industry to describe control blade depletion. In order to estimate SNVT, a CASMO Stu [2009] model of a representative BWR bundle was used to determine an average value of the absolute neutron flux in that bundle. This provided a thermal neutron flux of $\phi_t = 2.5606 \times 10^{13} \frac{ntns}{s-cm^2}$. Using this thermal flux, the SNVT at simulation time t can be calculated as $\phi_t \times t$. Note that this flux is only used to map from seconds to SNVT for plotting purposes and was not used in any other calculation. From [Kennard and Harbottle, 2000, p. 230, 233], a 10% reduction in reactivity worth corresponds to a 42% decrease in B10 number density, and this would happen at around 2.5 SNVT.

In Figure 28, it is shown that with the calculations used for this work, the control blade has depleted to 42% B10 after between 1.5 and 2 SNVT. Considering the use of a thermal flux from CASMO to map time from seconds to SNVT, this is a reasonable agreement with the results found in Kennard and Harbottle [2000].

Figure 28 shows that the use of a bundle average void instead of a radial void distribution translates to a slightly slower depletion in the control blade. In terms of rod worth, the decrease in worth when using a radial void distribution is less than 0.5% greater than that found using a uniform void distribution when it has reached a 10% reduction (see Figure 30).

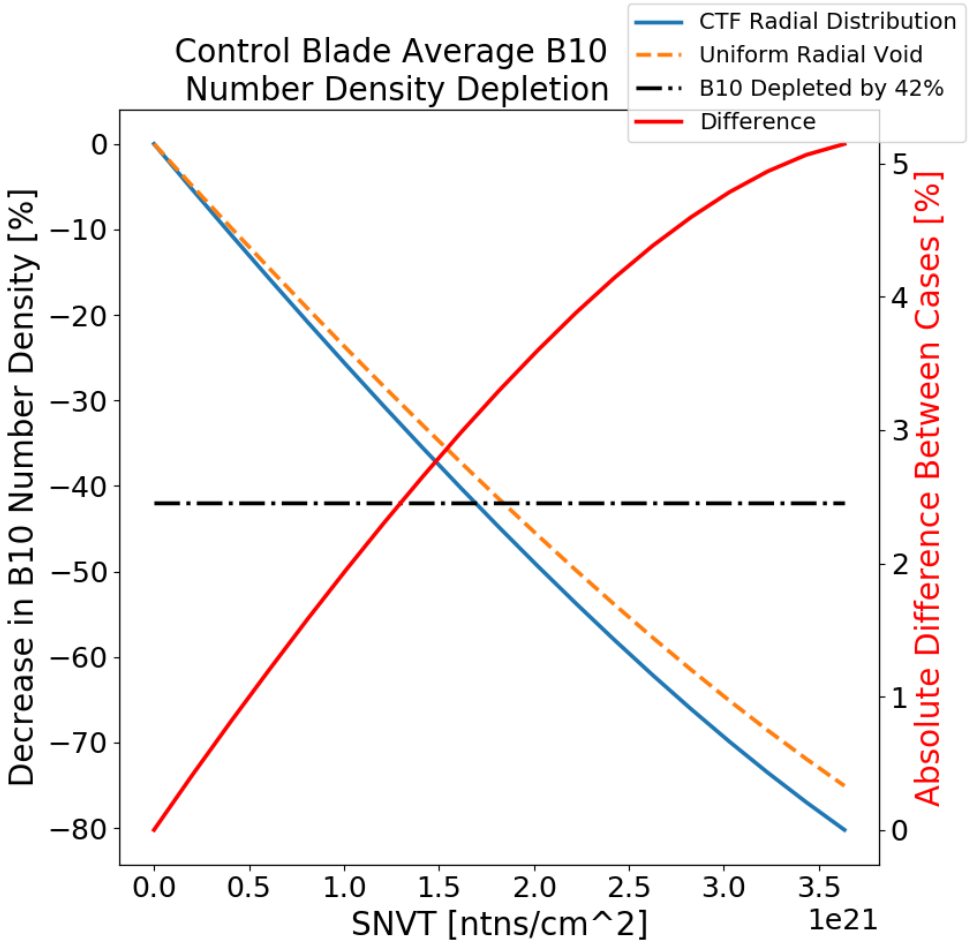

Figure 28. Decrease in B10 number density as a function of SNVT.

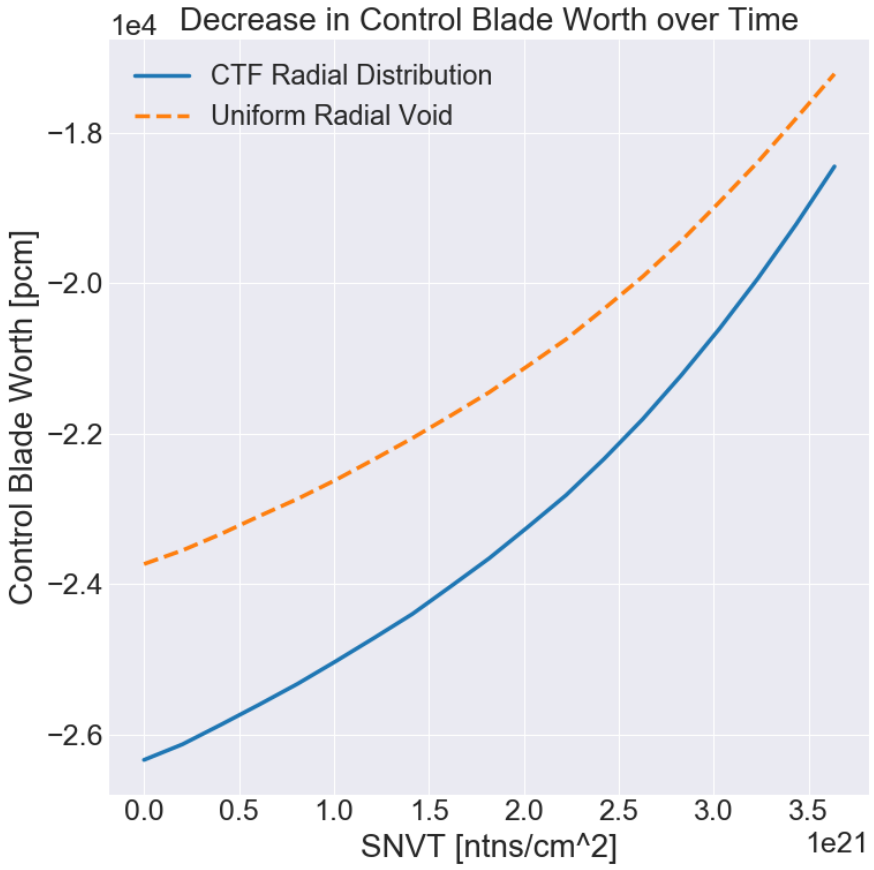

Figure 29. Change in control rod worth as a function of SNVT.

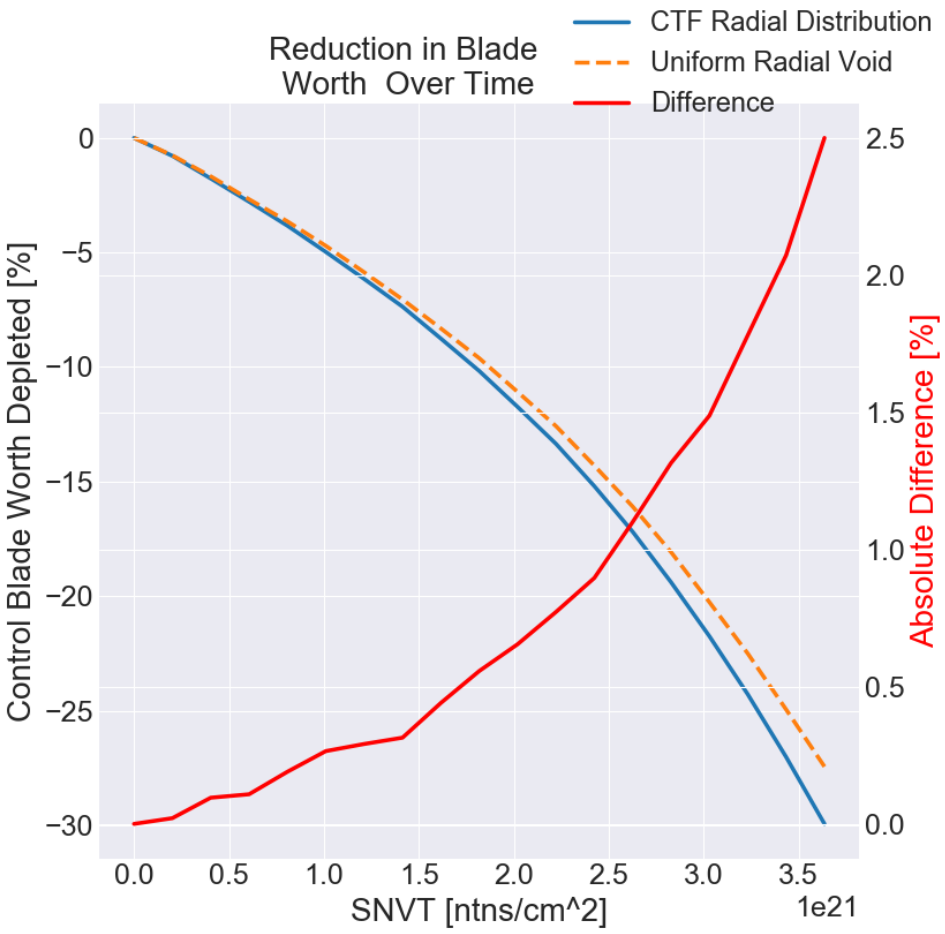

Figure 30. Percent decrease in control blade worth as a function of SNVT.

Figure 29 shows the reactivity worth of a control blade as a function of SNVT for both radial void profiles. The reactivity worth at time t was calculated using the following formula,

$$\rho = \frac{k\,(t) - k_{uncontrolled}}{k\,(t)\,k_{uncontrolled}}, \tag{10}$$

where $k_{uncontrolled}$ and $k\,(t)$ depend on the void distribution used. Although Figure 28 and Figure 30 indicate that the rate of control rod depletion is relatively unaffected by the use of a uniform void distribution, Figure 29 shows that the uniform void approximation can lead to a greatly underestimated rod worth at any given time. This supports the fact that the uniform void distribution pushes pin power into the corner away from the control blade and thus shifts the neutron flux away from the control blade (see Figure 17).

3 Conclusions

3.1 Implications of Results

The goal of this work was to determine how sensitive BWR neutronics calculations were to the following:

- The use of a uniform void at the bundle average instead of a radial distribution
- The use of pin-centered channels when the thermal-hydraulics code uses coolant-centered channels
- Explicit consideration of annular flow

In addition to the above items, it was of interest to see how sensitive control blade depletion calculations would be to the uniform void approximation.

In subsection 2.2, the results show that the use of a uniform void at the bundle average instead of a radial distribution always leads to an overestimation of k_{eff}. In fact, in one of the cases considered, the eigenvalue was almost 1,900 pcm too large when making this approximation. Furthermore, the use of a bundle average void can lead to significant errors in the calculation of pin-by-pin fission rates. In uncontrolled cases, errors of up to 10.5% were found, and in controlled cases errors were as large as 29.5%. Based on these results, it is clear that the neutronics calculations were very sensitive to the uniform void, and the use of this bundle average void comes at the cost of accuracy in both pin power and eigenvalue calculations. However, as was shown in subsection 2.5, it was found that the use of a bundle average void does not significantly affect the overall depletion rate of a control blade. It is important to note that Figure 29 indicates that although the rate of depletion is relatively unaffected by the use of a bundle average void, the actual rod worth is significantly affected.

Although the averaging process used to determine moderator density on a pin-centered channel basis from coolant-centered channel data preserves mass, it causes slight smearing and redistribution of void across the assembly. This is similar in nature to what occurs with the use of a bundle average void, although when averaging over a pin-centered channel basis instead of averaging across the entire bundle, the void redistribution occurs to a lesser extent. Accordingly, in areas of the assembly where void is low, in some slight way, the void will be raised locally. In areas where void is high, the void will be slightly lowered. When using pin-centered channels averaged from coolant-centered channel data, in channels next to the hottest rods, the local void will be lowered. In channels next to cooler rods such as gadolinium rods or the fuel pins on the sides of a bundle facing a control blade, the void will be decreased locally, and pin powers will be artificially decreased as a result of the smeared void. In subsection 2.3, it is shown that the results could be a difference of as much as a 231 pcm increase in eigenvalue and an increase in normalized fission rate of as much as 1.2%.

In subsection 2.4, it is shown that when annular flow is considered, the fission rates of fuel pins adjacent to gadolinium pins increase by as much as 3% in the most limiting pins. This occurred in both GE9 and GE14 bundles, and the use of a control blade did not seem to affect which pins would have increased fission rates. When a control blade was inserted, even though it dampened

the increase in pin power from modeling annular flow in pins near the blade, it did not change which pins experienced this increase.

Overall, the results indicate that the use of a uniform radial void profile can lead to significant errors in the neutronics calculation. The use of pin-centered channels averaged from coolant-centered data leads to an additional error of potentially over 200 pcm in the eigenvalue and up to 1.2% in fission rates. This means that the use of uniform radial void profiles should be phased out, and if a thermal-hydraulics code which calculates moderator properties on a coolant-centered channel basis is used, then coolant-centered channels should also be used in the neutronics calculations. This would provide the most accurate coupled calculations possible. Furthermore, from subsection 2.4, it is clear that fission rate calculations are sensitive to the presence of annular flow when gadolinium pins are present. Because BWR bundles often contain gadolinium, this could play an important role in obtaining accurate pin powers in BWR cores.

3.2 Further Work

The cases used for this project consisted of single assembly calculations. VTM has recently been updated to be able to generate multi-assembly MCNP inputs, and similar studies on multi-assembly cases would help mitigate any exaggeration of pin power differences caused simply by the small geometry, and it would also indicate how sensitive larger cases are to the use of the approximations discussed in this work. Furthermore, fuel depletion was not considered. It would be of interest to determine how the inaccuracies in pin powers affect fuel pin depletion and how the differences in pin power behave over time as the fuel depletes. Finally, the MCNP models used consisted of 1 cm tall radial "slices" of BWR bundles. In many modern BWR bundles, partial length fuel rods and axially varied fuel enrichments are used. In the future, 3D MCNP cases which consider these complex geometries should be considered. For added accuracy, these 3D bundle cases should be explicitly coupled with CTF.

Because the results of subsection 2.4 indicate a sensitivity in neutronics calculations to the presence of annular flow, more work should be performed to better represent annular flow in neutronics calculations. This would allow for further analysis of the effects of annular flow on fission rates.

4 REFERENCES

References

[1] D.J. Kelly. Depletion of a BWR Lattice Using the RACER Continuous Energy Monte Carlo Code. In *Proceedings of the International Conference on Mathematics and Computations, Reactor Physics, and Environmental Analyses*. American Nuclear Society, 1995.

[2] Spent Nuclear Fuel for Disposal in the KBS-3 Repository. Technical report, Svensk KÃď rnbrÃď nslehantering AB, December 2010. TR-10-13.

[3] M.L. Fensin. Optimum Boiling Water Reactor Fuel Design Strategies to Enhance Reactor Shutdown by the Standby Liquid Control System. Master's thesis, 2004.

[4] J. Solis *et al.* Boiling Water Reactor Turbine Trip (TT) Benchmark. Technical report, US NRC, OECD Nuclear Energy Agency, February 2001.

[5] E.E. Lewis. *Fundamentals of Nuclear Reactor Physics*. Academic Press, Elsevier, 2008.

[6] U.S. NRC. Power Reactors, Septermber 2019. URL https://www.nrc.gov/reactors/power.html.

[7] N.E. Todreas and M.S. Kazimi. *Nuclear Systems: Thermal Hydraulic Fundamentals*, volume 1. CRC Press, Taylor and Francis Group, second edition, 2011.

[8] J.K. Shultis and R.E. Faw. *Fundamentals of Nuclear Science and Engineering*. CRC Press, Taylor and Francis Group, second edition, 2008.

[9] R.K. Salko and M.N. Avramova. *CTF Theory Manual*. CASL, May 2016. CASL-U-2016-1110-000.

[10] ChemicaLogic. Steamtab companion, November 2003.

[11] *MCNP Users Manual - Code Version 6.2*. Los Alamos National Laboratory, 2017. LA-UR-17-29981.

[12] M.W. Kennard and J.E. Harbottle. BWR Control Blade Replacement Strategies. Technical report, Stoller Nuclear Fuel, NAC International, 2000. URL https://inis.iaea.org/search/search.aspx?orig_q=RN:31008499.

[13] ORNL. The Virtual Environment for Reactor Applications (VERA). URL https://www.casl.gov/vera.

[14] B. Collins *et al.* *MPACT Theory Manual - Code Version 2.0*. CASL, March 2015. CASL-U-2015-0078-000.

[15] S. Palmtag. Initial Boiling Water Reactor (BWR) Input Specifications. Technical report, CASL, February 2015. CASL-U-2015-0040-000.

[16] United Performance Metals. 304 Stainless Steel and 304L Stainless Steel Sheet, Coil, & Bar - AMS 5513, 5511, 5647. URL https://www.upmet.com/products/stainless-steel/304304l.

[17] READE. Boron Carbide Powder (B_4C), organization=Reade Advanced Materials. URL https://www.reade.com/products/boron-carbide-powder-b4c.

[18] L.J. Covington and H-N.M. Gheorghiu. Generic CMS BWR Equilibrium Model. Rev. 2. Technical report, Studsvik Scandpower, March 1999. SSP-99/407.

[19] *CASMO-4: A Fuel Assembly Burnup Program Users Manual*. Studsvik Scandpower, Inc., 2009. SSP-09/443-U Rev 0.

[20] J.L. Conlin, editor. *Listing of Available* `ACE` *Data Tables*. January 2017. LA-UR-17-20709.

[21] E.M. Baum *et al*. *Chart of the Nuclides*. Knolls Atomic Power Laboratory, seventeenth edition, 2010.

APPENDICES

A Calculation of Vapor Cell Sizes for Approximation of Annular Flow

A.1 Cylindrical Annular Flow

Table 13. Parameters of interest in determination of subchannel annuli for BWRs.

$M_{chan}^{(i,j)}$	Mass of moderator in channel (i,j)
ρ_l	Density of saturated liquid at nominal system pressure
ρ_g	Density of saturated vapor at nominal system pressure
$\overline{\rho^{(i,j)}}$	Density found for subchannel (i,j)
$A^{(i,j)}$	Area of subchannel (i,j)
$r_g^{(i,j)}$	Radius of annulus for subchannel (i,j)
$\alpha^{(i,j)}$	Void fraction of subchannel (i,j)
$h^{(i,j)}$	Height of subchannel (i,j)

For any channel (i,j) the density, $\overline{\rho^{(i,j)}}$, can be found using the channel void fraction, $\alpha^{(i,j)}$, determined from a code such as COBRA-TF. Determination of the channel density is through Equation 11.

$$\overline{\rho^{(i,j)}} = \left(1 - \alpha^{(i,j)}\right) \rho_l + \alpha^{(i,j)} \rho_g \tag{11}$$

From $\overline{\rho^{(i,j)}}$, the total mass in subchannel (i,j) can be determined using Equation 12.

$$M_{chan}^{(i,j)} = A^{(i,j)} \overline{\rho^{(i,j)}} h^{(i,j)} \tag{12}$$

The total mass of the channel could also be determined from the summation of the mass in a saturated liquid region and a saturated vapor region.

$$M_{chan}^{(i,j)} = A_l^{(i,j)} h^{(i,j)} \rho_l + A_g^{(i,j)} h^{(i,j)} \rho_g \tag{13}$$

Setting Equation 12 and Equation 13 equal:

$$A^{(i,j)} \overline{\rho^{(i,j)}} h^{(i,j)} = A_l^{(i,j)} h^{(i,j)} \rho_l + A_g^{(i,j)} h^{(i,j)} \rho_g, \tag{14}$$

but

$$A^{(i,j)} = A_l^{(i,j)} + A_g^{(i,j)} \tag{15}$$

$$A^{(i,j)} \overline{\rho^{(i,j)}} h^{(i,j)} = \left(A^{(i,j)} - A_g^{(i,j)}\right) h^{(i,j)} \rho_l + A_g^{(i,j)} h^{(i,j)} \rho_g, \tag{16}$$

noting that the area containing saturated vapor will be modeled as an annulus, and cancelling out the channel height from both sides of Equation 16,

$$A^{(i,j)} \overline{\rho^{(i,j)}} = \left(A^{(i,j)} - \pi \left(r_g^{(i,j)}\right)^2\right) \rho_l + \pi \left(r_g^{(i,j)}\right)^2 \rho_g \tag{17}$$

$$A^{(i,j)}\left[\left(1-\alpha^{(i,j)}\right)\rho_l+\alpha^{(i,j)}\rho_g\right]=\left(A^{(i,j)}-\pi\left(r_g^{(i,j)}\right)^2\right)\rho_l+\pi\left(r_g^{(i,j)}\right)^2\rho_g \tag{18}$$

$$A^{(i,j)}\left[\rho_l-\alpha^{(i,j)}\rho_l+\alpha^{(i,j)}\rho_g-\rho_l\right]=\pi\left(r_g^{(i,j)}\right)^2\left(\rho_g-\rho_l\right) \tag{19}$$

$$A^{(i,j)}\alpha^{(i,j)}\left(\rho_g-\rho_l\right)=\pi\left(r_g^{(i,j)}\right)^2\left(\rho_g-\rho_l\right) \tag{20}$$

$$r_g^{(i,j)}=\left[\frac{A^{(i,j)}\alpha^{(i,j)}\left(\rho_g-\rho_l\right)}{\pi\left(\rho_g-\rho_l\right)}\right]^{\frac{1}{2}} \tag{21}$$

$$r_g^{(i,j)}=\left[\frac{A^{(i,j)}\alpha^{(i,j)}}{\pi}\right]^{\frac{1}{2}}. \tag{22}$$

A.2 Subchannel-Shaped Annular Flow

Cylindrical annuli in coolant-centered channel MCNP input have one fault in that they do not take advantage of the entire channel before the void cell expands into the fuel pins, thus making the cylindrical annular flow unusable. This can be modified if the radial shape of the void cell is assumed to be the same shape as the channel itself. In this case, it is the shape of a square with a quarter circle removed from each corner, so the area of the vapor patch can be written as follows:

$$A_g^{(i,j)}=\left(s_g^{(i,j)}\right)^2-\pi\left(r_g^{(i,j)}\right)^2 \tag{23}$$

Assuming that the value of $s_g^{(i,j)}$ is related to $r_g^{(i,j)}$ by some constant γ such that $\gamma s_g^{(i,j)}=r_g^{(i,j)}$:

$$A_g^{(i,j)}=\left(s_g^{(i,j)}\right)^2-\pi\left(\gamma s_g^{(i,j)}\right)^2 \tag{24}$$

$$A_g^{(i,j)}=\left(1-\pi\gamma^2\right)\left(s_g^{(i,j)}\right)^2 \tag{25}$$

Until Equation 16, no assumptions on the shape of the void cell has been made. Applying Equation 25 to Equation 16 and canceling the channel height from both sides yields:

$$A^{(i,j)}\overline{\rho^{(i,j)}}=\left(A^{(i,j)}-\left(\left(1-\pi\gamma^2\right)\left(s_g^{(i,j)}\right)^2\right)\right)\rho_l+\left(\left(1-\pi\gamma^2\right)\left(s_g^{(i,j)}\right)^2\right)\rho_g \tag{26}$$

$$A^{(i,j)}\overline{\rho^{(i,j)}}-A^{(i,j)}\rho_l=\left(\left(1-\pi\gamma^2\right)\left(s_g^{(i,j)}\right)^2\right)\left(\rho g-\rho_l\right) \tag{27}$$

$$A^{(i,j)}\left(\overline{\rho^{(i,j)}}-\rho_l\right)=\left(\left(1-\pi\gamma^2\right)\left(s_g^{(i,j)}\right)^2\right)(\rho g-\rho_l) \tag{28}$$

$$\frac{A^{(i,j)}\left(\overline{\rho^{(i,j)}}-\rho_l\right)}{(\rho g-\rho_l)\left(1-\pi\gamma^2\right)}=\left(s_g^{(i,j)}\right)^2 \tag{29}$$

$$s_g^{(i,j)}=\left[\frac{A^{(i,j)}\left(\left(1-\alpha^{(i,j)}\right)\rho_l+\alpha^{(i,j)}\rho_g-\rho_l\right)}{(\rho g-\rho_l)\left(1-\pi\gamma^2\right)}\right]^{\frac{1}{2}} \tag{30}$$

$$s_g^{(i,j)}=\left[\frac{A^{(i,j)}\left(\rho_l-\alpha^{(i,j)}\rho_l+\alpha^{(i,j)}\rho_g-\rho_l\right)}{(\rho g-\rho_l)\left(1-\pi\gamma^2\right)}\right]^{\frac{1}{2}} \tag{31}$$

$$s_g^{(i,j)}=\left[\frac{A^{(i,j)}\alpha^{(i,j)}\left(\rho_g-\rho_l\right)}{(\rho g-\rho_l)\left(1-\pi\gamma^2\right)}\right]^{\frac{1}{2}} \tag{32}$$

$$s_g^{(i,j)}=\left[\frac{A^{(i,j)}\alpha^{(i,j)}}{\left(1-\pi\gamma^2\right)}\right]^{\frac{1}{2}} \tag{33}$$

One option for gamma is $\gamma=\frac{r_{pin}}{s_{pin}}$, where r_{pin} is the fuel pin radius, and s_{pin} is the pin pitch. A depiction of this type of annular cell is shown in Figure 31.

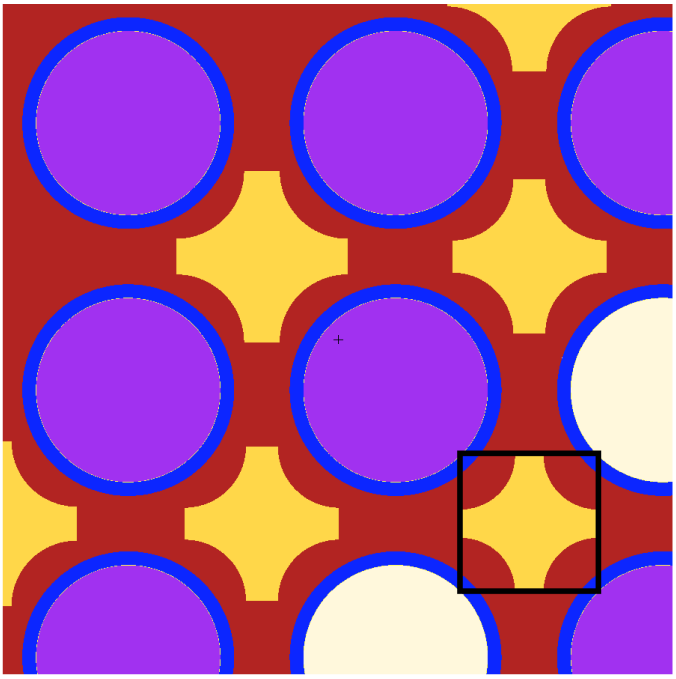

Figure 31. Depiction of the shape of the subchannel-shaped annular flow approximation. The subchannel-shaped annular flow is represented by yellow cells. The corners of the black square are in the same locations as the centers of the quarter circles removed from the corners of the vapor cell.

Notice that with this method, the centers of the cylindrical surfaces change location as the vapor cell increases in size.

A.3 Improved Subchannel-Shaped Annular Flow

In the subchannel-shaped annular flow of the previous section, it is clear from Figure 31 that with this approximation, the liquid film along the edge of fuel pins is not uniform within a moderator channel. Additionally, walls of liquid which show up along the edges of the coolant-centered channels as the void fraction increases. For clarity, the issues have been marked in Figure 32. To mitigate these issues, a slightly different approach is taken in which the saturated vapor cell is allowed to stretch to the edges of each coolant-centered channel, and the radius of the quarter circle removed from each corner of the cell is altered. An example of this improved form of subchannel-shaped annular flow is shown in Figure 33.

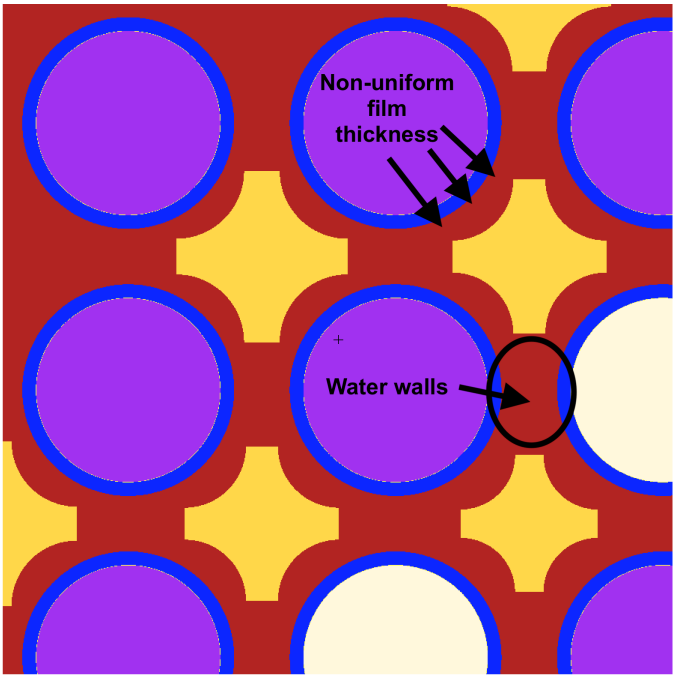

Figure 32. Demonstration of problems with the subchannel-shaped annular flow.

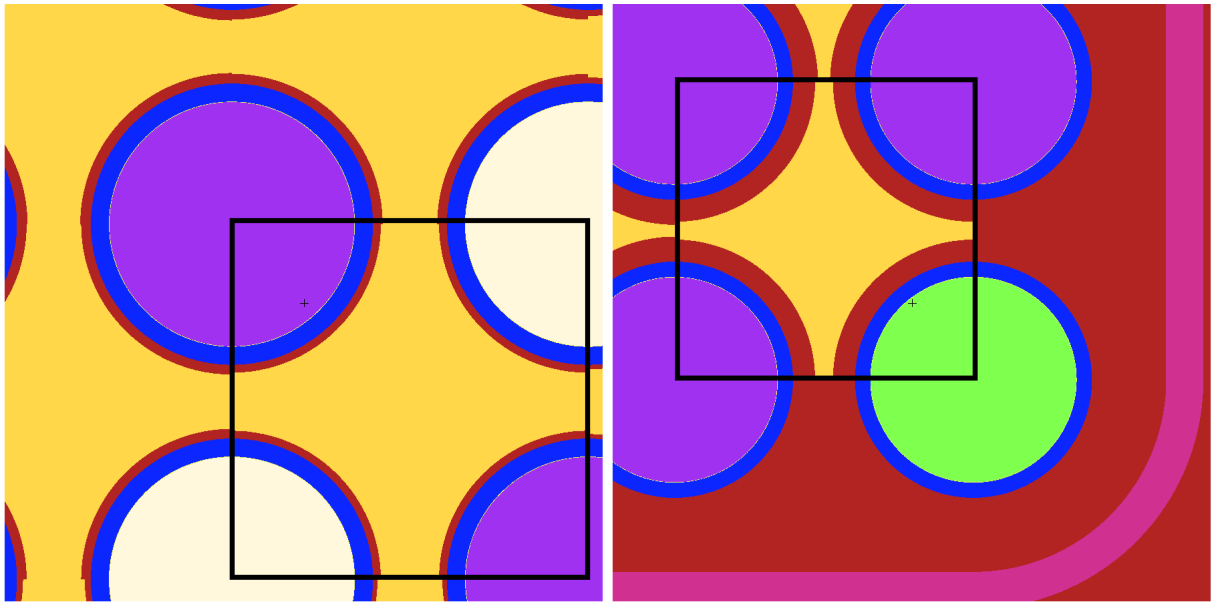

Figure 33. Depiction of the shape of the improved subchannel-shaped annular flow approximation. The vapor cell in the annular flow is represented by yellow cells. The corners of the black square are in the same locations as the centers of the quarter circles removed from the corners of the vapor cell. A high void case (left) and lower void case (right) are depicted to demonstrate how the vapor cell expands as void increases.

Notice that in this improved method of calculating the area of the vapor cells, the centers of the cylindrical surfaces removed from the corners of the cell are set to the center of the neighboring fuel pins, and the radius of these cylinders is decreased as the void fraction. Therefore, the area of the vapor cells increases. Using a derivation similar to that used in the previous two sections, the radius of the four corner cylinders can be determined using the following formula:

$$r_g^{(i,j)} = \left[\frac{s_p^2 - A^{(i,j)} \alpha^{(i,j)}}{\pi} \right]^{\frac{1}{2}}. \tag{34}$$

In this case, the width of the vapor cells is equal to the pin pitch, s_p. This is seen from the black box outlining the overall square shape of the vapor cell in Figure 33. With this new version of the subchannel-shaped annular flow, if the void is too low, then the radius of the corners becomes too large and will overlap. For this reason, if the radius of the corner cylinders is calculated to be over one half of the pin pitch, then the annular flow shape is reverted back to the original subchannel shape method. In this case, the vapor cells are small enough that the water walls and nonuniform liquid film should be less noticeable.

B MCNP Input Generation Using VTM

Generation of input files for MCNP can be a tedious task. Inputs used to model LWR fuel can have hundreds of cells for a single assembly. It is much easier to type up a VERA input (see the example in section C). To leverage the VERA common input, a python program called VERA to MCNP (VTM) was developed to read in the VERA inputs processed by VERAin and generate MCNP inputs with minimal extra input. The VTM input requires 22 values, all of which are described in Table 14.

B.1 VTM Problem Setup

The problem setup is the first stage of the process for building MCNP input files. VTM starts by reading in its own input, which consists of the 22 variables described in Table 14, and then storing the variables in a Python dictionary: $infile$. The MPACT cross section file supplied in the VTM input is parsed to collect the atomic masses of each isotope in the file. These atomic masses are used to convert mass densities to number densities in order to match the number densities used in MPACT as closely as possible.

Table 14. Input variables for VTM

folder	Path to the folder that contains the VERA XML to be read
subfolder	The MCNP input generated will be placed in
subsubfolder	$folder + subfolder + subsubfolder$
filename	The name of the VERA XML to be read
outfile	Name of MCNP input that will be printed
modfile	Name of CTF HDF5 file containing channel areas and void fractions (must be placed in $folder$)
moddensdiff	Select moderator distribution Options are described in Table 15.
channel_type	Select pin-centered or coolant-centered channels
axlev	Select the axial plane to pull moderator densities from the CTF HDF5 file
reactor_type	Select whether the reactor is PWR or BWR
wide_wide_gap	Select which corner to use as the wide wide corner (ignored for multiassembly cases)
cb-abs	flag for control blade absorption tallies
cbdep_flag	flag to turn on control blade depletion option
cbdep_step	Current time-step in control blade depletion process
cbdep_stop	Final time-step for control blade depletion
cbdep_delt	control blade depletion time-step size in days
xs_lib	Index for which MCNP cross section library to use (i.e. for ENDF/B-VII.1 use 8 [20]
KCODE	The KCODE card from MCNP
RAND	The RAND card from MCNP
LOST	The LOST card from MCNP
PRDMP	The PRDMP card from MCNP
MPACTdat	The name of the MPACT cross section file used in the MPACT run

Table 15. Options for the $moddensdiff$ variable in the VTM input file

0	Set moderator cells to uniform density based on void fraction in VERA XML
1	Set moderator densities to values based on the local void fractions from the CTF HDF5; this is a nonuniform option
2	Set moderator cells to uniform density based on lattice average void fraction from axial plane of interest from CTF
3	Construct annular flow model where moderator cells contain a cell of saturated liquid water around fuel and saturated vapor in the center of the channel; in this case, use cylindrical vapor cells, the size of which is determined by the mass balance in section A
4	Same as option 4 except with subchannel-shaped vapor cells
5	Same as option 4, but read void fraction from a .txt file instead

B.2 Boron-10 Depletion in Control Blades in VTM

For number density depletion of ^{10}B, the basic balance equation for reactions of importance in ^{10}B are shown in Equation 35.

$$\frac{dN(t)}{dt} = -N(t)\sigma_a\phi(t), \tag{35}$$

the solution of which is

$$N(t) = N(0)e^{-\sigma_a\phi(t)t}. \tag{36}$$

Currently, VTM depletes ^{10}B in each time step using the formula

$$N^{(t+1)} = N^{(t)}e^{-\sigma_a^{(t)}\phi^{(t)}\Delta t}. \tag{37}$$

However, a numerical scheme for Equation 35 is easily obtained by letting $\frac{dN(t)}{dt} = \frac{N_{t+1}-N_t}{\Delta t}$, in which case, the number densities should be depleted using Equation 38:

$$N_{t+1} = N_t\left(1 - \sigma_a\phi_t\Delta t\right). \tag{38}$$

If the temporal discretization were sufficiently fine, then Equation 38 could be used to approximate the depletion of ^{10}B. However, short time steps require a significant increase in the compute time used in MCNP, so VTM uses Equation 37.

B.3 How Is the Absorption Rate Determined?

B.3.1 First, Determine Pin Powers

In each pin, i, a pin power is requested in the following form:

$$P_i = N_i\int_0^\infty \phi(E)\sum_j f_j Q\left(E\right)\sigma_{f,j}(E)dE = N_i\overline{\sigma_{f,i}}\overline{\phi_i Q_i}. \tag{39}$$

In Equation 39, j is an isotope index, and f_j is the atomic ratio of isotope j. An example of the tally cards used to request this information for each fuel pin is as follows:

```
fc814 Tally in (1,9,1)
f814:n   354
fm814   -1  28  (-6 -8)
sd814   1
```

The units on these parameters are given in the table below.

Table 16. Units on MCNP pin power tallies as requested by VTM

N_i	$\frac{atoms}{barn-cm}$
$\overline{\sigma_f}$	$10^{-24}cm^2$
$\overline{\phi}$	$\frac{ntns-cm}{unit-time}$
$\overline{Q}$	$\frac{MeV}{fission}$
P_i	$\frac{(atoms-ntns)MeV}{(unit-time)fission} \Longrightarrow \frac{MeV}{unit-time}$

Note that the units on $\overline{\phi}$ are $\frac{ntns-cm}{unit-time}$ and not $\frac{ntns}{unit-time-cm^2}$. This is because MCNP usually divides tallies by the cell volume. VTM sets a segment divider card (`sdi`) of 1.0 which overrides this division by volume, so instead of $\frac{(particle-weight)(track-length)}{V_i}$, the output tallies will simply be $(particle-weight)(track-length)$.

The values P_i are then converted to $\frac{J}{unit-time}$. If it is assumed that this unit time is some multiple of seconds, then

$$\frac{J}{unit-time} = \frac{J}{sec\gamma} = \frac{1}{\gamma}Watts. \tag{40}$$

To use this data, it is necessary to determine γ. In VTM, this is carried out by assuming a $\hat{P} = 54\frac{KW}{L}$ power density and calculating the total output power from the assembly in question using Equation 41, where S_a is the assembly pitch and H is the current height,

$$P_{tot} = S_a^2 H\hat{P}. \tag{41}$$

Using this P_{tot} (converted to Watts) and letting $P_{mcnp} = \sum_i P_i$,

$$\frac{P_{tot}}{P_{mcnp}} \implies \frac{Watts}{Watts\frac{1}{\gamma}} \implies \gamma = \frac{P_{tot}}{P_{mcnp}}. \tag{42}$$

B.3.2 Determine boron-10 only absorption rates

Now, γ can be used to tie the MCNP "per unit source time" to a physical time scale. The ^{10}B absorption rates in B_4C cell i are requested in the following form:

$$A_i = N_i \int_0^\infty \phi_i(E)\sigma_{a,i}^{B10}(E)dE = N_i\overline{\sigma_{a,i}^{B10}}\overline{\phi_i}. \tag{43}$$

To ensure that $\sigma_{a,i}^{B10}$ is truly only from ^{10}B, a "false" material card that contains only ^{10}B is setup in the MCNP input and used as the material in each absorption tally's multiplier card. Below is an example of this tally and material:

```
c  abs-B10
M39   5010.81c 1.000000000000000E+0
```

```
...

fc1234 Absorption Tally North/South Blade Tube: 2 ring 1
f1234:n   481
fm1234   -1  39  (-2)
sd1234   1
fc1244 Absorption Tally North/South Blade Tube: 3 ring 1
f1244:n   483
fm1244   -1  39  (-2)
sd1244   1
```

At this point, N_i is the total number density of cell i (from the `-1` in `fmi`), so each absorption rate is multiplied by $\frac{10^{-24}}{N_i}$, where 10^{-24} is in units $\frac{cm^2}{barn}$. Thus, the absorption rate is now in the form shown in Equation 44:

$$\hat{A}_i = \overline{\sigma_{a,i}^{B10}}\overline{\phi_i}. \tag{44}$$

Here, $\overline{\phi}$ has the same units as shown in the above table (again, the division by cell volume is canceled by an `sdi 1.0` card). $\overline{\sigma_{a,i}^{B10}}$ has the same units as $\overline{\sigma_f}$. Therefore, the units of $\hat{A}_i$ are $\frac{cm^2-ntns-cm}{sec}$. Note that the "per seconds" is included because these absorption rates have already been multiplied by the normalization factor needed to yield a $54\frac{KW}{L}$ power density from the pin powers determined by MCNP. Finally, $\hat{A}_i$ is divided by the volume of cell i:

$$\widetilde{A_i} = \frac{\hat{A}_i}{V_i},$$

and $\widetilde{A_i}$ is in units of $\frac{ntns}{sec}$, or simply sec^{-1}. Now, $\widetilde{A_i}$ can be used in Equation 37 to determine depleted number densities at the end of a given time-step, as follows:

$$N_{i,B10}^{(t+1)} = N_{i,B10}^{(t)} exp\left[-\widetilde{A_i^{(t)}}\Delta t\right], \tag{45}$$

where Δt is in seconds. For the next time step, the total cell number density is decreased using Equation 46:

$$N_i^{(t+1)} = N_i^{(t)} - \left(N_{i,B10}^{(t)} - N_{i,B10}^{(t+1)}\right). \tag{46}$$

B.3.3 Should Other Absorption Rates Be Considered?

The 17$^{\text{th}}$ edition of the BECHTEL Chart of the Nuclides [21] is employed to analyze potential neutron interactions in the the absorber tubes of control blades, which contain B_4C. The two naturally occurring isotopes of boron are ^{10}B and ^{11}B, and they occur at atomic fractions of 19.9 and 80.1%, respectively. The (n,α) cross section of ^{10}B is nearly 4,000 barns. The other cross sections of ^{10}B are less than 1 barn, so approximating all ^{10}B absorptions as the (n,α) will be

acceptable. The ^{11}B isotope has thermal and fast capture cross sections, and at 5 millibarns and 2 millibarns, these will not contribute significantly and can be ignored. Therefore, in VTM control blade depletion calculations, the depletion of ^{11}B is not tracked.

The two naturally occurring carbon isotopes: ^{12}C and ^{13}C, both have capture cross sections of 3.5 millibarns or less. If that capture occurs and ^{11}C is formed, then its capture cross section is less than 1 microbarn. ^{14}C will decay through a β^- decay into ^{14}N, but with a half-life of 5,715 years. This will not be a significant reaction. Additionally, the sub μb capture cross section of ^{14}C means that there will not be a significant amount of ^{15}C produced, so this chain does not need to be followed any further.

So far, the (n, α) is the most important neutron interaction in B_4C. The interaction takes place in the following form:

$$B^{10} + n \rightarrow \alpha + Li^7$$

^{4}He (the same as an α particle for neutronic applications) is neutronically inert, so tracking ^{4}He is not necessary. ^{7}Li has two capture cross sections, and at 45 and 20 millibarns, these will not have any large effects. Furthermore, if a neutron is absorbed by ^{7}Li, then ^{8}Li is formed, and it decays to ^{8}Be with a half life of 0.84 seconds. ^{8}Be has a half-life on the order of 10^{-17} seconds and undergoes decay as

$$Be^8 \rightarrow 2\alpha$$

If ^{7}Li does absorb any neutrons, then it quickly follows a chain of decay into helium nuclei and thus will not be a significant contributor of absorption in the control blade.

In summary, the only reaction that requires tracking is the destruction of ^{10}B-10 through absorption. Thus, the methods described in the previous sections are sufficient for simulating control blade depletion.

B.3.4 Control Blade Depletion Process

To deplete control blades, many MCNP cases are run for a given system, each being for a different time step. When `cbdep_flag` and `cb-abs` from Table 14 are turned on, the material cards for B_4C are set up for each individual absorber tube cell, and absorption rates tallies are requested as described in subsubsection B.3.2. The MCNP case is then run, and the resulting pin power tallies are used as shown in subsubsection B.3.1 to obtain a renormalization factor which can be applied to all tallies to obtain accurate absolute absorption rates. Absorption rates in each absorber tube, pin powers, and B_4C number densities are stored in a separate file for each time step.

First, VTM is run for the first time-step with a fresh control blade. The number densities in each absorber tube are stored in a JSON formatted file called *data.json* to be used later. All data in this file are stored in a time-dependent array. After this first case finishes, a separate script performs the calculations from subsubsection B.3.1 and subsubsection B.3.2 on the results, and then it stores the absorption rates in *data.json*. The value of `cbdep_step` in the VTM input is incremented up from 0 to 1, and VTM is called again. Because `cbdep_step` is greater than 0, VTM grabs the data from *data.json* and uses the number densities and absorption rates from the previous time step to calculate new ^{10}B number densities in each absorber tube using Equation 45. The new number densities are applied to the MCNP input and are then stored in *data.json*. Now,

the new MCNP is run, and the process repeats. This process is controlled by a shell script partnered with VTM.

C Example VERA Input for a Single BWR Assembly

```
! ------------------------------------------------------------------------------
! MPACT single lattice BWR input Built by MSLGEN on: October 12, 2019 at 20:04:59
! ------------------------------------------------------------------------------

[CASEID]
  title 'BWR 2D Single Lattice @ void=40.0 [%], Fuel Temp=900 K type=8x8_1'

[STATE]
  power               100.0
  tinlet              600 K
  tfuel               900 K
  pressure             1040
  sym                  full
  feedback              off
  void
     40.0
  boron                 0.0
  xenon                zero
  rodbank               A 0

[CORE]
  reactor_type          BWR
  size                    1
  apitch              15.24
  height                1.0
  rated          0.01161288 0.01
  core_shape
      1
  assm_map
     ASSY1
  crd_map
     BLADE
  bc_rad         reflecting
  bc_top         reflecting
  bc_bot         reflecting
  mat            zr2 6.56 zirc2
  mat            zr4 6.56 zirc4
  mat            he 0.000176 he-4
  crd_bank                A

[ASSEMBLY]
  npin                    8
  ppitch             1.6256
```

```
 gap             0.9525 0.47498
 channel_box     zr4 0.2032 0.9652 0.0 0.0
 fuel            U16  10.0642 94.5 / 1.6
 fuel            U20  10.0642 94.5 / 2.0
 fuel            U22  10.0642 94.5 / 2.2
 fuel            U24  10.0642 94.5 / 2.4
 fuel            U26  10.0642 94.5 / 2.6
 fuel            U28  10.0642 94.5 / 2.8
 fuel            U30  10.0642 94.5 / 3.0
 fuel            U36  10.0642 94.5 / 3.6
 fuel            U36G  9.939  94.5 / 3.6 / gad=4.0
 fuel            U38  10.0642 94.5 / 3.8
 fuel            U40  10.0642 94.5 / 3.95
 fuel            U40G  9.939  94.5 / 3.95 / gad=4.0


 cell            1 0.53213 0.61341 / U16  zr2
 cell            2 0.53213 0.61341 / U20  zr2
 cell            3 0.53213 0.61341 / U22  zr2
 cell            4 0.53213 0.61341 / U24  zr2
 cell            5 0.53213 0.61341 / U26  zr2
 cell            6 0.53213 0.61341 / U28  zr2
 cell            7 0.53213 0.61341 / U30  zr2
 cell            8 0.53213 0.61341 / U36  zr2
 cell            9 0.53213 0.61341 / U38  zr2
 cell            10 0.53213 0.61341 / U40  zr2
 cell            51 0.53213 0.61341 / U40G zr2
 cell            52 0.53213 0.61341 / U36G zr2
 cell            WR 1.60 1.62 / mod zr4 / large4


 lattice         LAT
       1
       2  6
       4  8 10
       6 10 52 WR
       6 10 10 WR WR
       6 10 51 10 10 10
       5  9 10 51 10 51 10
       3  7  9 10 10 10  9  6

 axial           ASSY1  0.0 LAT 1.0


[CONTROL]
```

```
  title          GE OEM Control Blade
  npin                    8
  stroke                1 1
  mat            ss304 8.0  ss
  mat            abs   1.757 b4c
  cell           TUBE 0.17526 0.23876 / abs ss304
  blade          21 TUBE 12.3825 0.79248 0.39624 0.14224  1.98501  ss304
  rodmap         EMPTY
    TUBE
    - -
    - - -
    - - - -
    - - - - -
    - - - - - -
    - - - - - - -
    - - - - - - - -

  axial          BLADE 0.0 EMPTY 1.0


[MPACT]
  vis_edits             fsr
  grid_treatment homogenize
  ray_spacing          0.01
  polars_octant           3
  azimuthals_octant        64
  quad_type      CHEBYSHEV-YAMAMOTO
  num_space               1
  num_angle              -8
  num_threads             1
```

D Example VTM Input

```
FILE PATH INFORMATION----------------------
folder = /Volumes/PhD/outputs/thesis_outs/MPACT/10x10Cases/
subfolder = set1/
subsubfolder = 0.0.0900.ave.mod.0.10x10_1/
filename = 0.0.0900.10x10_1.xml
outfile = 0.0.0900.ave.mod.0.10x10_1.mcnp
modfile = 10x10.control.ctf.h5
MODERATOR HANDLING INFORMATION------------
moddensdiff = 2
channel_type = mod
axlev = 0
GEOMETRY INFORMATION----------------------
reactor_type = bwr
wide_wide_gap = NW
CONTROL BLADE INFORMATION-----------------
cb-abs = 0
cbdep_flag = 0
cbdep_step = 0
cbdep_stop = 0
cbdep_delt = 0
DEALER'S CHOICE MCNP CARDS----------------
xs_lib = 8
KCODE 300000 1.000 100 2800
RAND GEN=2
LOST 150 150
MPACTdat mpact51g_71_v4.2m5_12062016_sph.fmt
PRDMP = J 200 1 1 15
```

E Additional Plots for Normalized Fission Rate Sensitivity to Bundle Average Void

The plots presented below are additional plots not shown in the main body of the report. These plots show pin power differences caused by the use of a bundle average void (bun) instead of the use of a radial void distribution (ctf). These cases were not found to be the most limiting cases for each bundle, but they still provide useful information. The maximum and minimum difference in the normalized fission rate for each case were reported in Table 8.

E.1 Controlled GE9

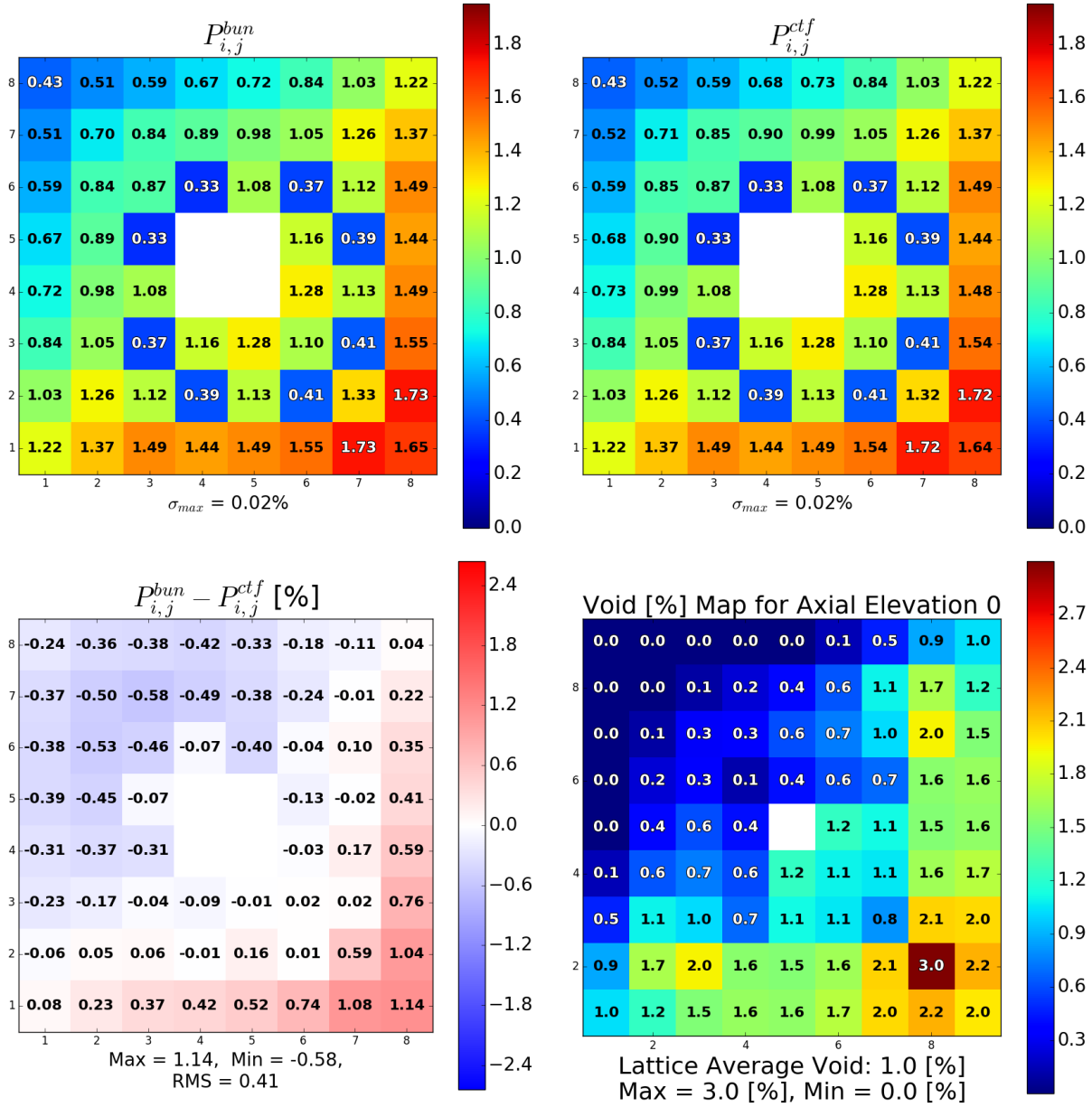

Figure 34. Comparison of normalized fission rates for the bottom of a controlled GE9 bundle in the bundle average void test.

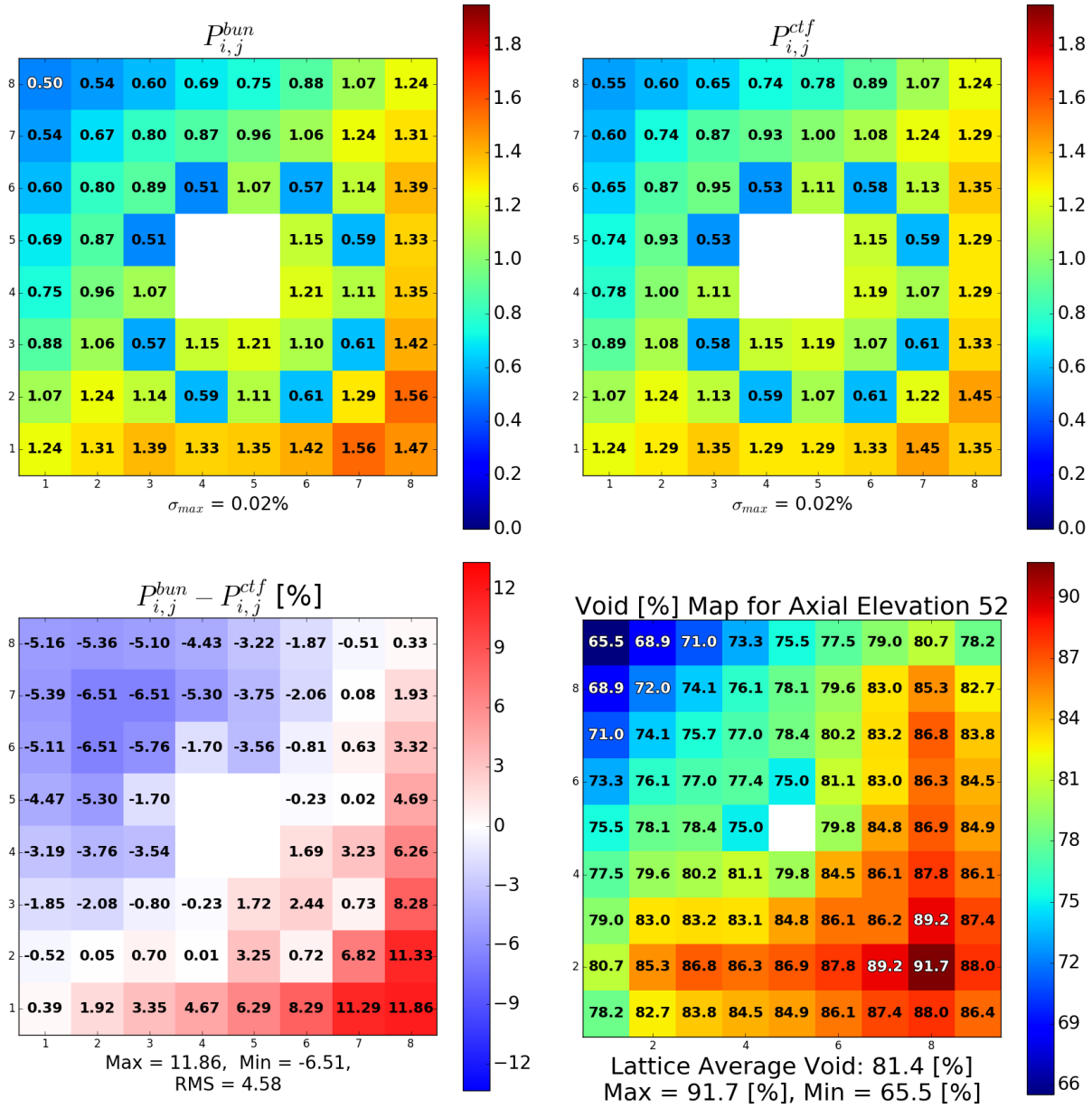

Figure 35. Comparison of normalized fission rates for the top of a controlled GE9 bundle in the bundle average void tests.

E.2 Uncontrolled GE9

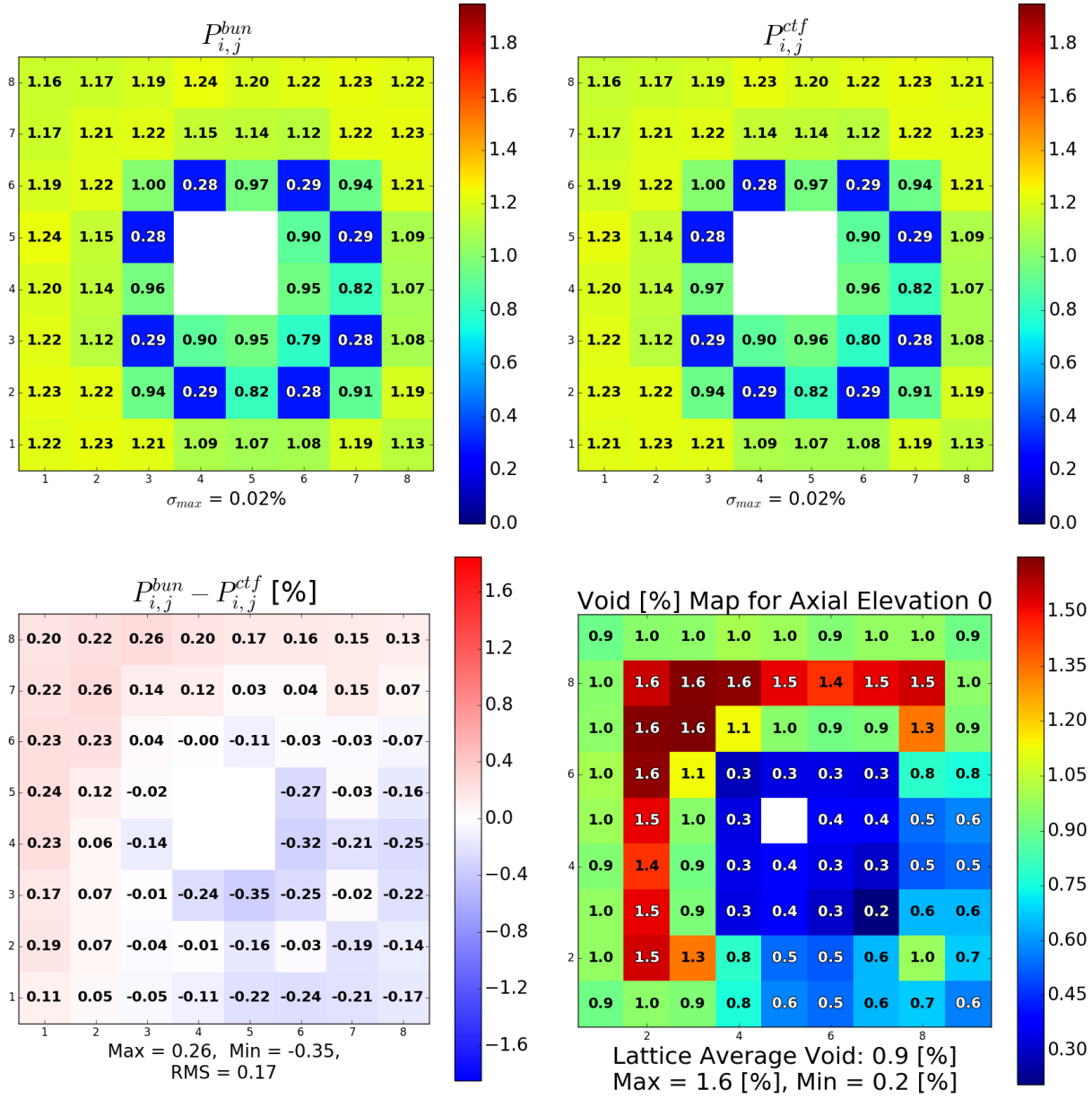

Figure 36. Comparison of normalized fission rates for the bottom of an uncontrolled GE9 bundle in the bundle average void tests.

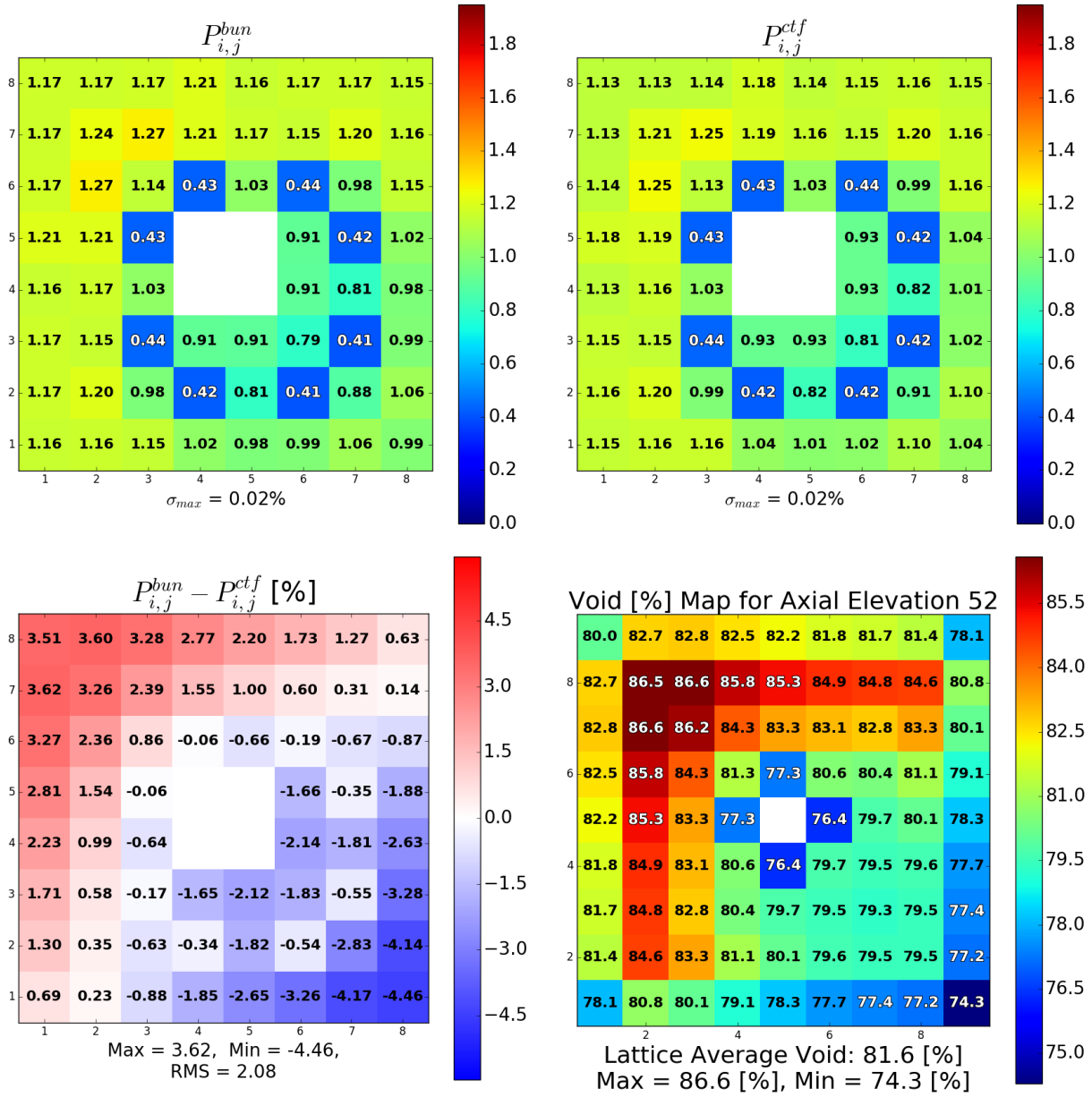

Figure 37. Comparison of normalized fission rates for the top of an uncontrolled GE9 bundle in the bundle average void tests.

E.3 Controlled GE14

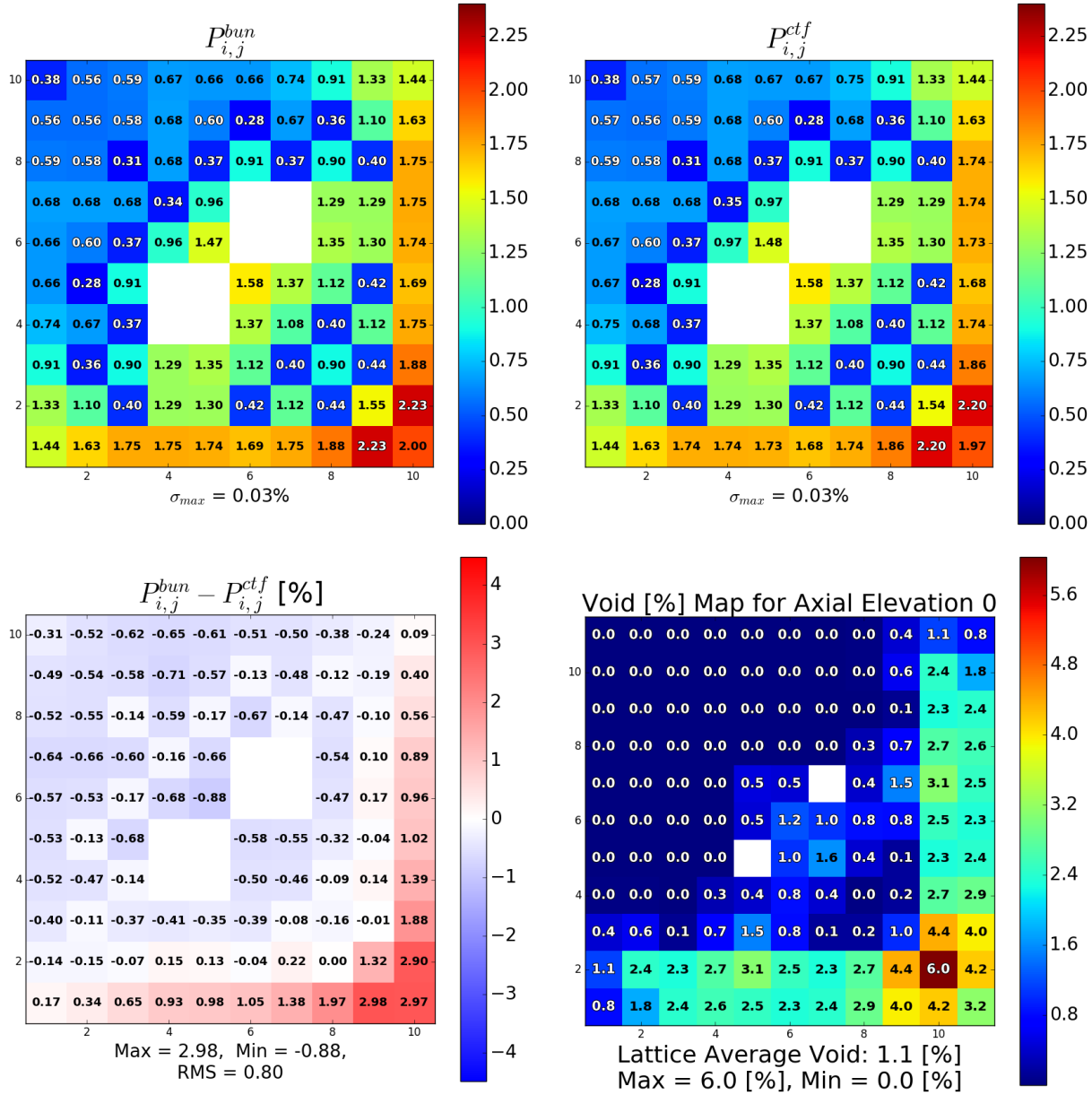

Figure 38. Comparison of normalized fission rates for the bottom of a controlled GE14 bundle in the bundle average void tests.

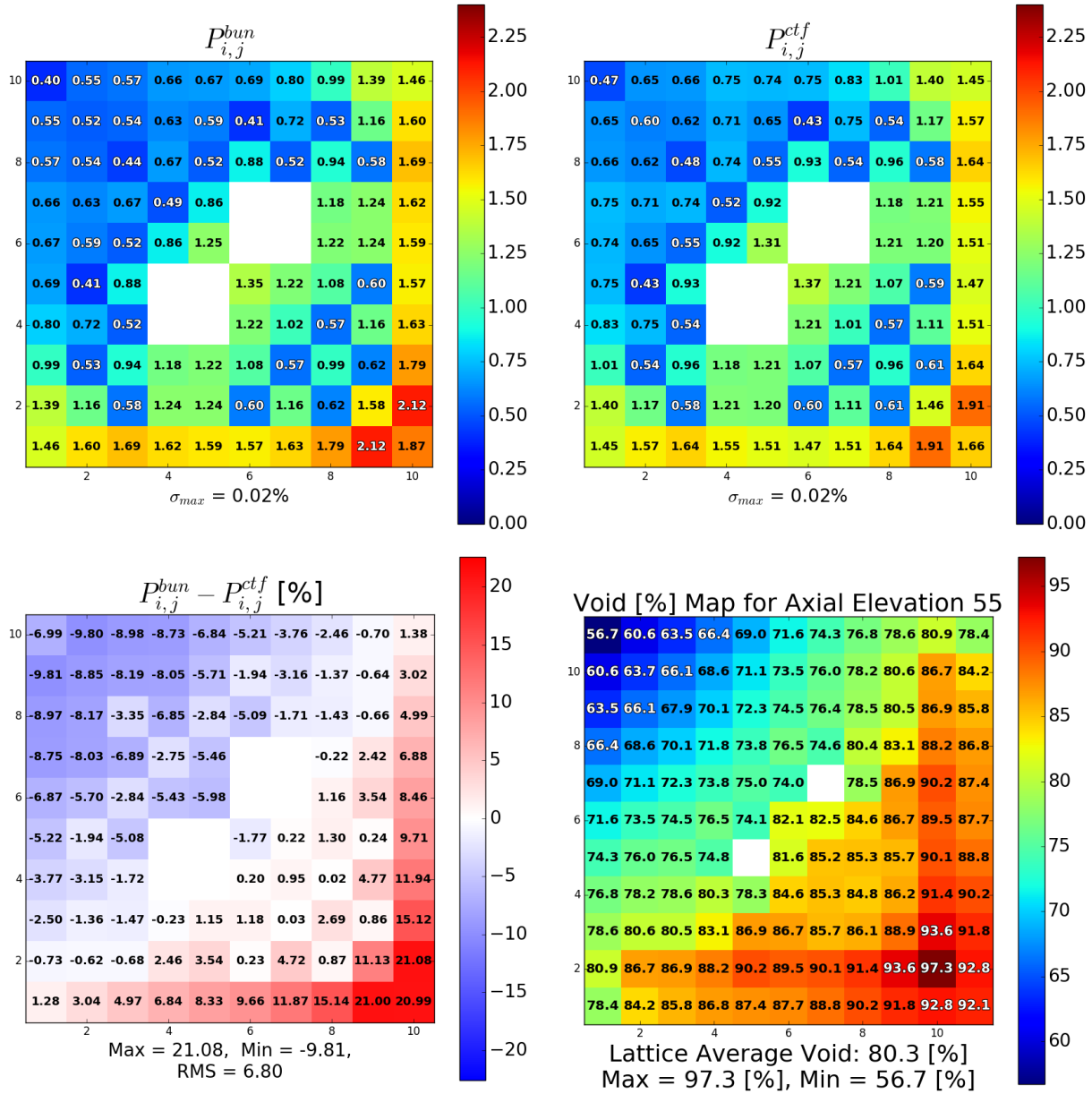

Figure 39. Comparison of normalized fission rates for the top of a controlled GE14 bundle in the bundle average void tests.

E.4 Uncontrolled GE14

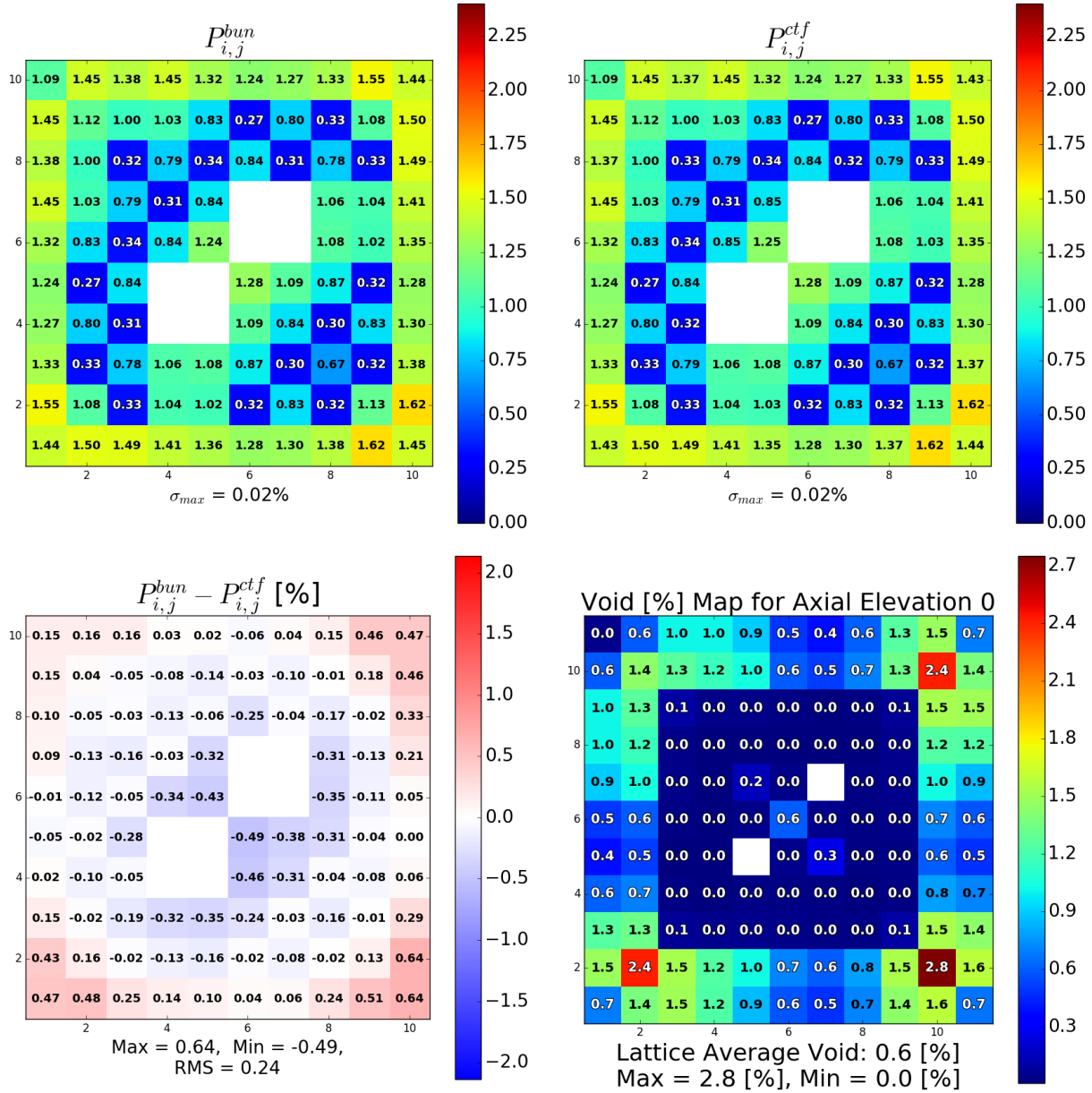

Figure 40. Comparison of normalized fission rates for the bottom of an uncontrolled GE14 bundle in the bundle average void tests.

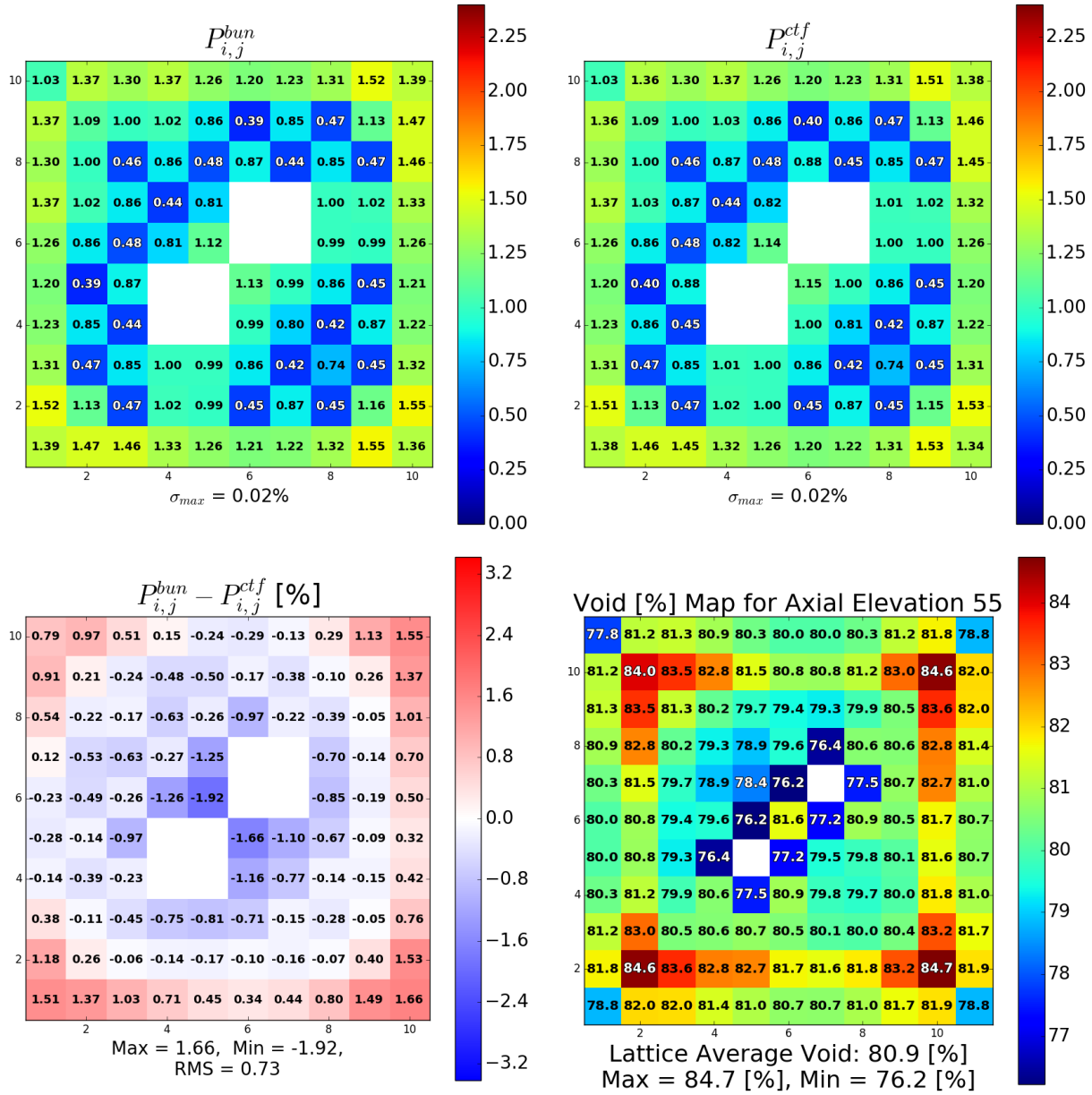

Figure 41. Comparison of normalized fission rates for the top of an uncontrolled GE14 bundle in the bundle average void tests.

F Additional Plots for Normalized Fission Rate Sensitivity to Pin-Centered Channels

Additional plots not shown in the main body of the report are provided below. These plots show normalized fission rate differences caused by implementation of pin-centered channels (*pin*) instead of coolant-centered channels (*mod*). Void distributions from CTF are determined in coolant-centered channels, and these data were mapped to a pin-centered channel basis using area weighting. These cases were not found to be the most limiting cases for each bundle. The maximum and minimum differences in normalized fission rate for each case are reported in Table 10.

F.1 Controlled GE9

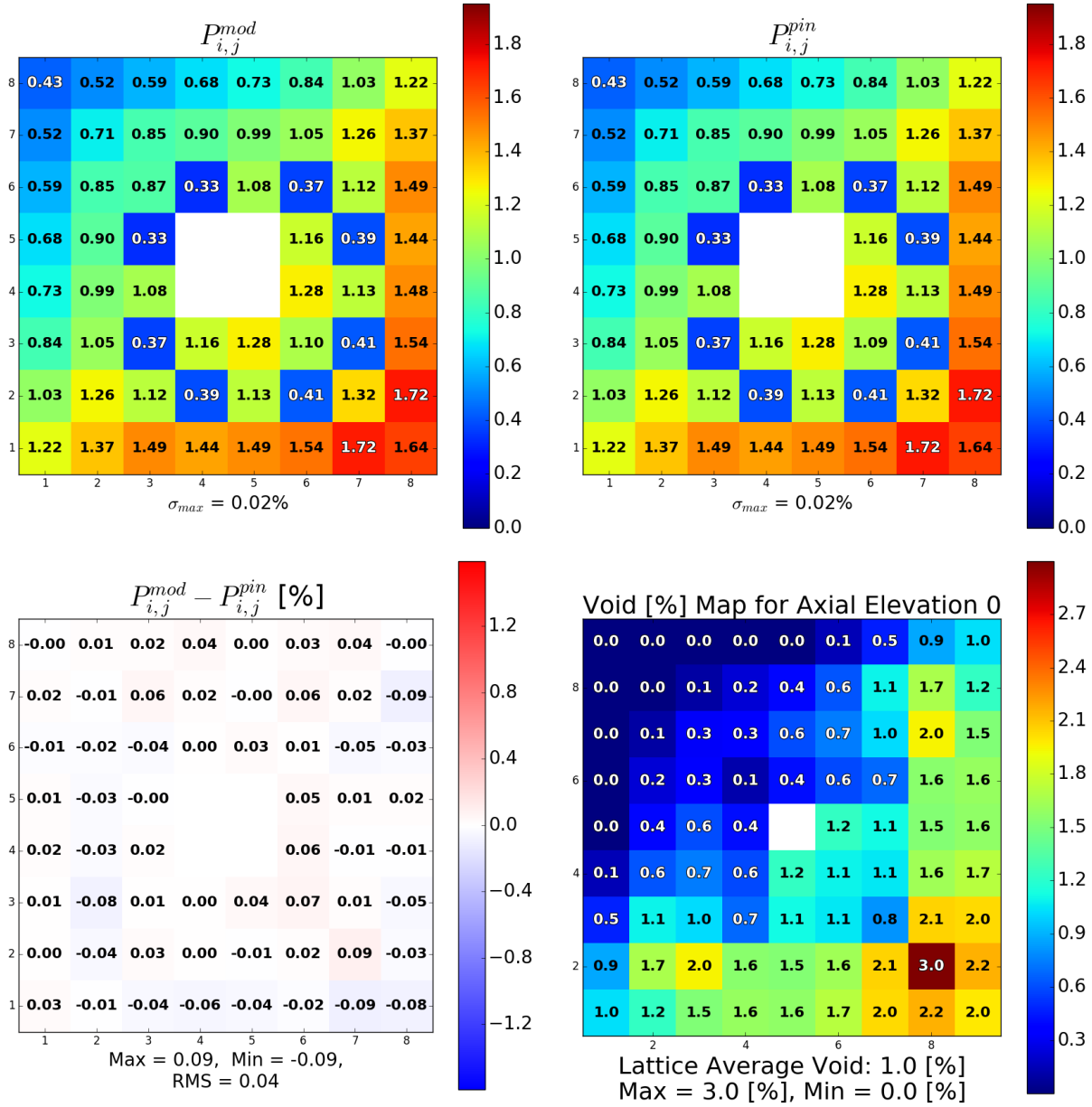

Figure 42. Comparison of normalized fission rates for the bottom of a controlled GE9 bundle in the pin-centered channel tests.

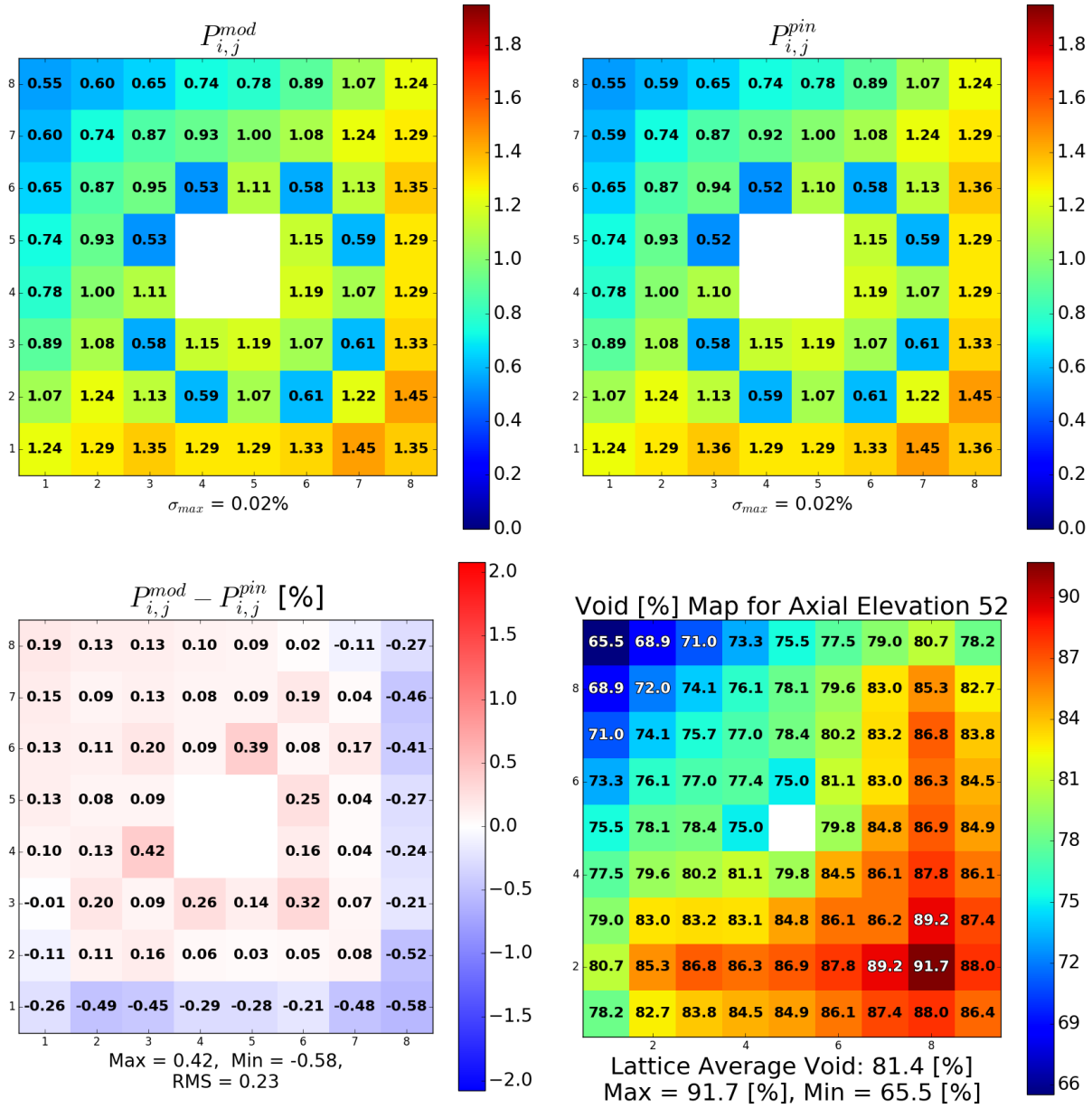

Figure 43. Comparison of normalized fission rates for the top of a controlled GE9 bundle in the pin-centered channel tests.

F.2 Uncontrolled GE9

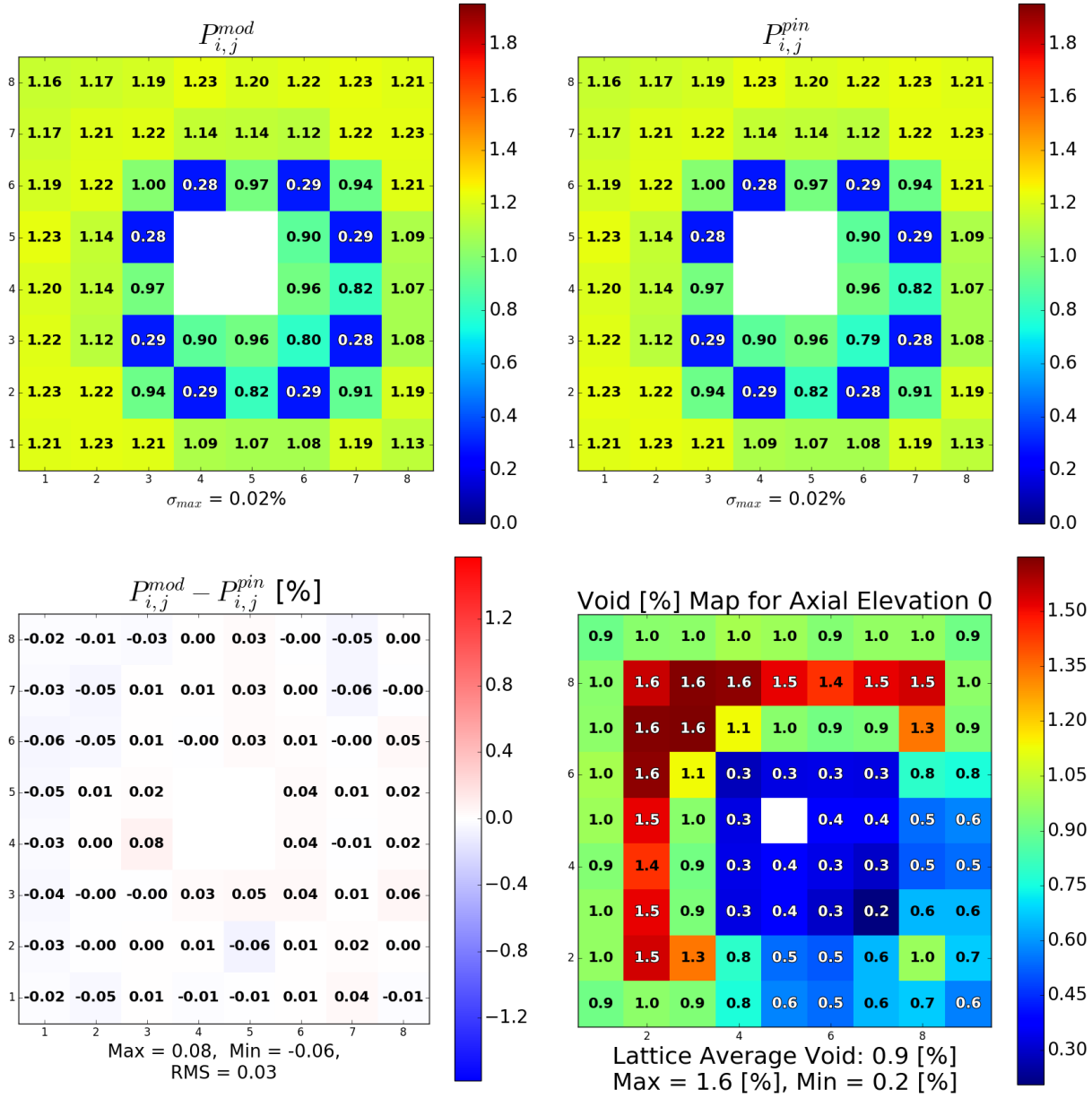

Figure 44. Comparison of normalized fission rates for the bottom of an uncontrolled GE9 bundle in the pin-centered channel tests.

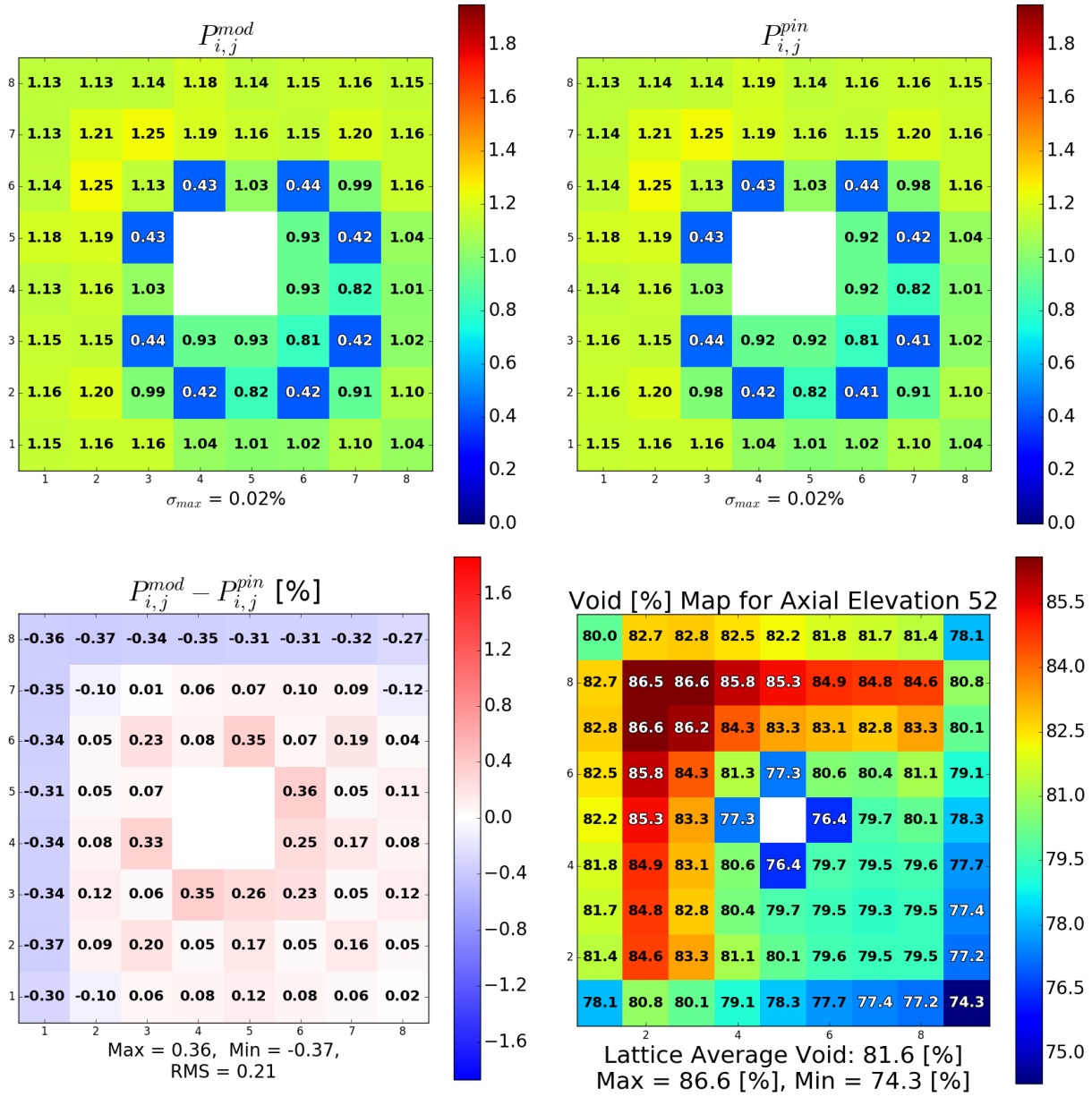

Figure 45. Comparison of normalized fission rates for the top of an uncontrolled GE9 bundle in the pin-centered channel tests.

F.3 Controlled GE14

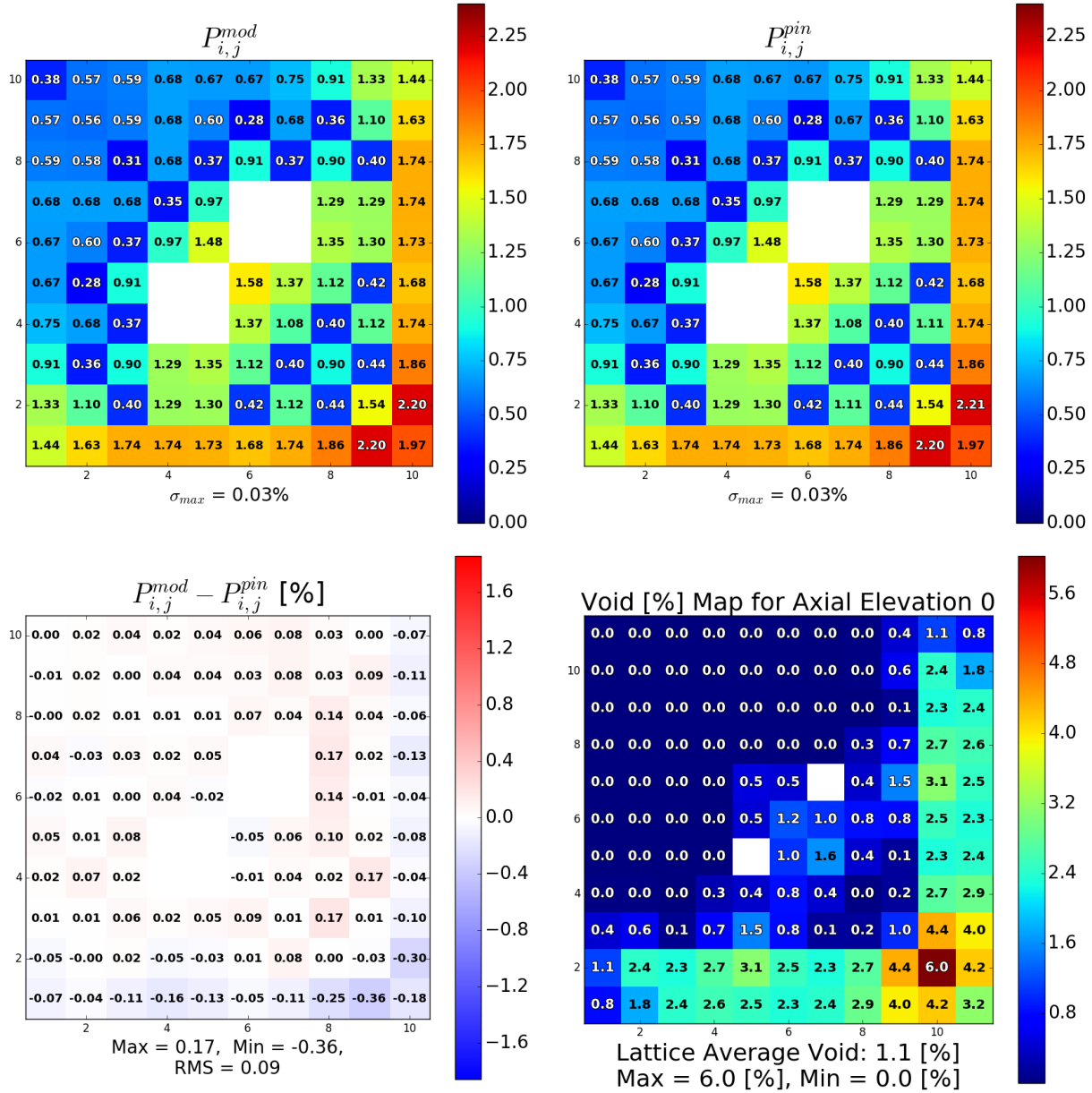

Figure 46. Comparison of normalized fission rates for the bottom of a controlled GE14 bundle in the pin-centered channel tests.

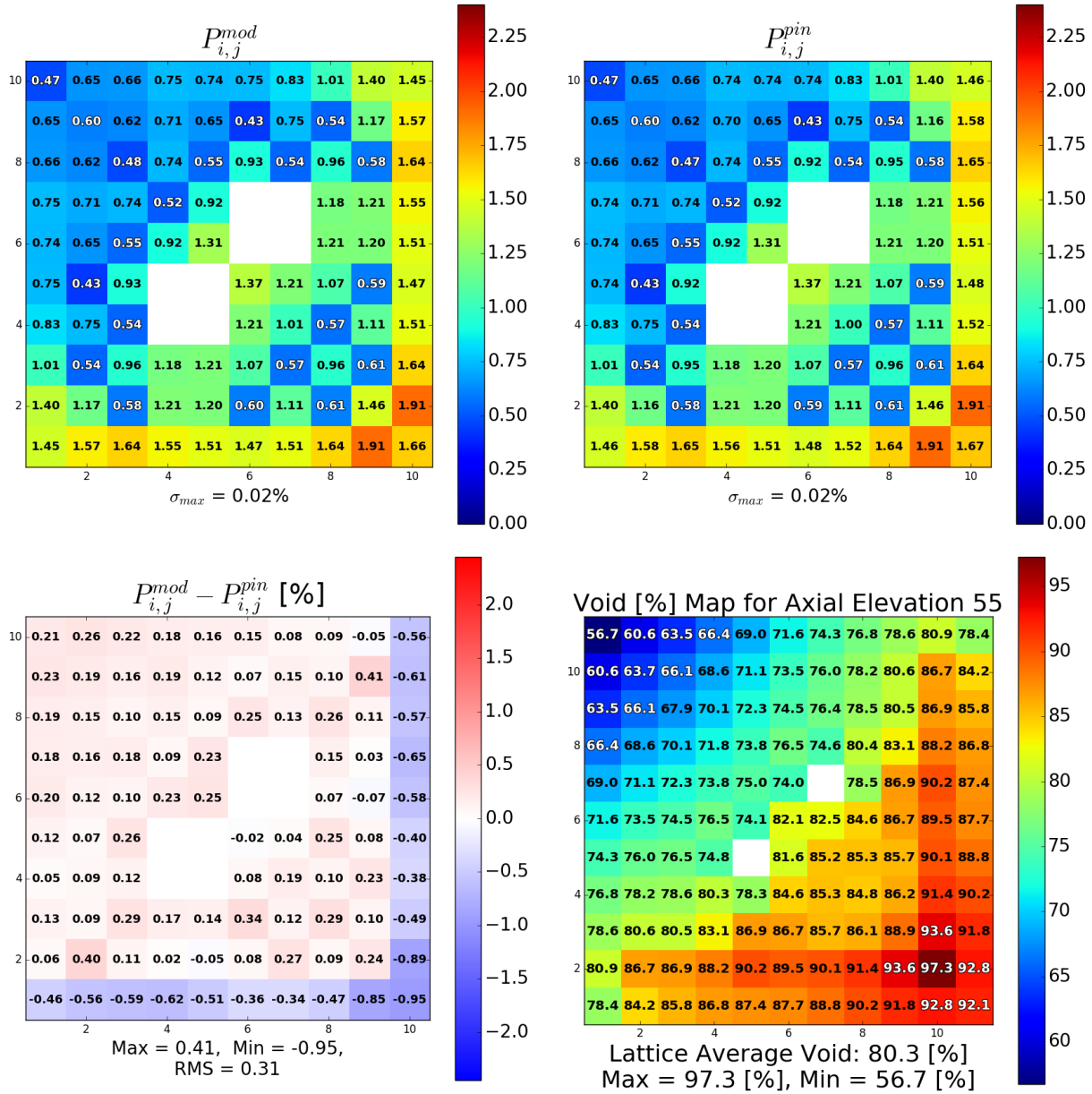

Figure 47. Comparison of normalized fission rates for the top of a controlled GE14 bundle in the pin-centered channel tests.

F.4 Uncontrolled GE14

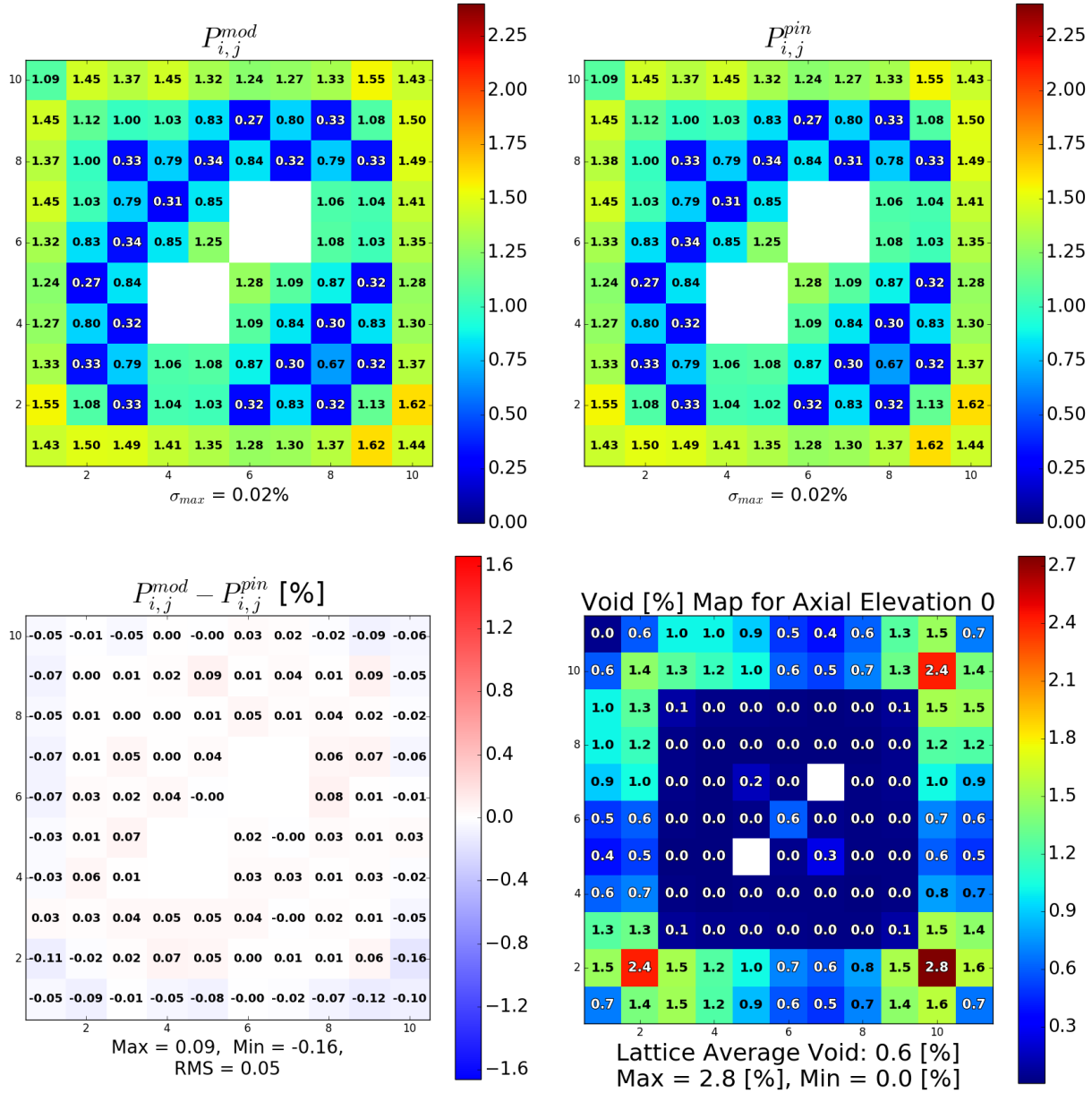

Figure 48. Comparison of normalized fission rates for the bottom of an uncontrolled GE14 bundle in the pin-centered channel tests.

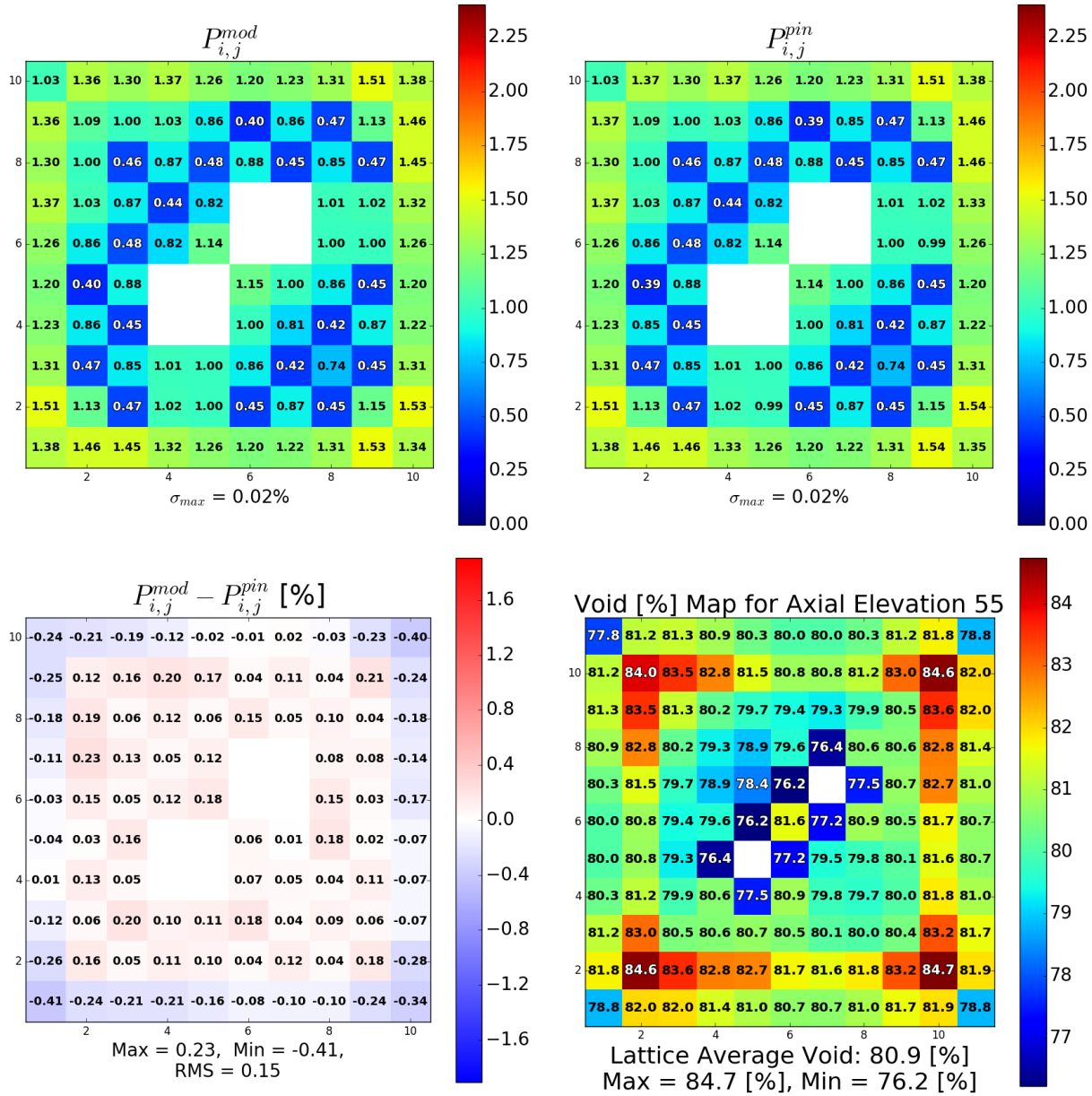

Figure 49. Comparison of normalized fission rates for the top of an uncontrolled GE14 bundle in the pin-centered channel tests.

G Additional Plots for Normalized Fission Rate Sensitivity to Annular Flow

Additional plots not shown in the main body of the report are provided below. These plots show normalized fission rate differences caused by the presence of annular flow (anu) as opposed to the use of a simple radial void distribution (ctf). These cases were not found to be the most limiting cases for each bundle. The maximum and minimum differences in normalized fission rate for each case were reported in Table 12.

G.1 Controlled GE9

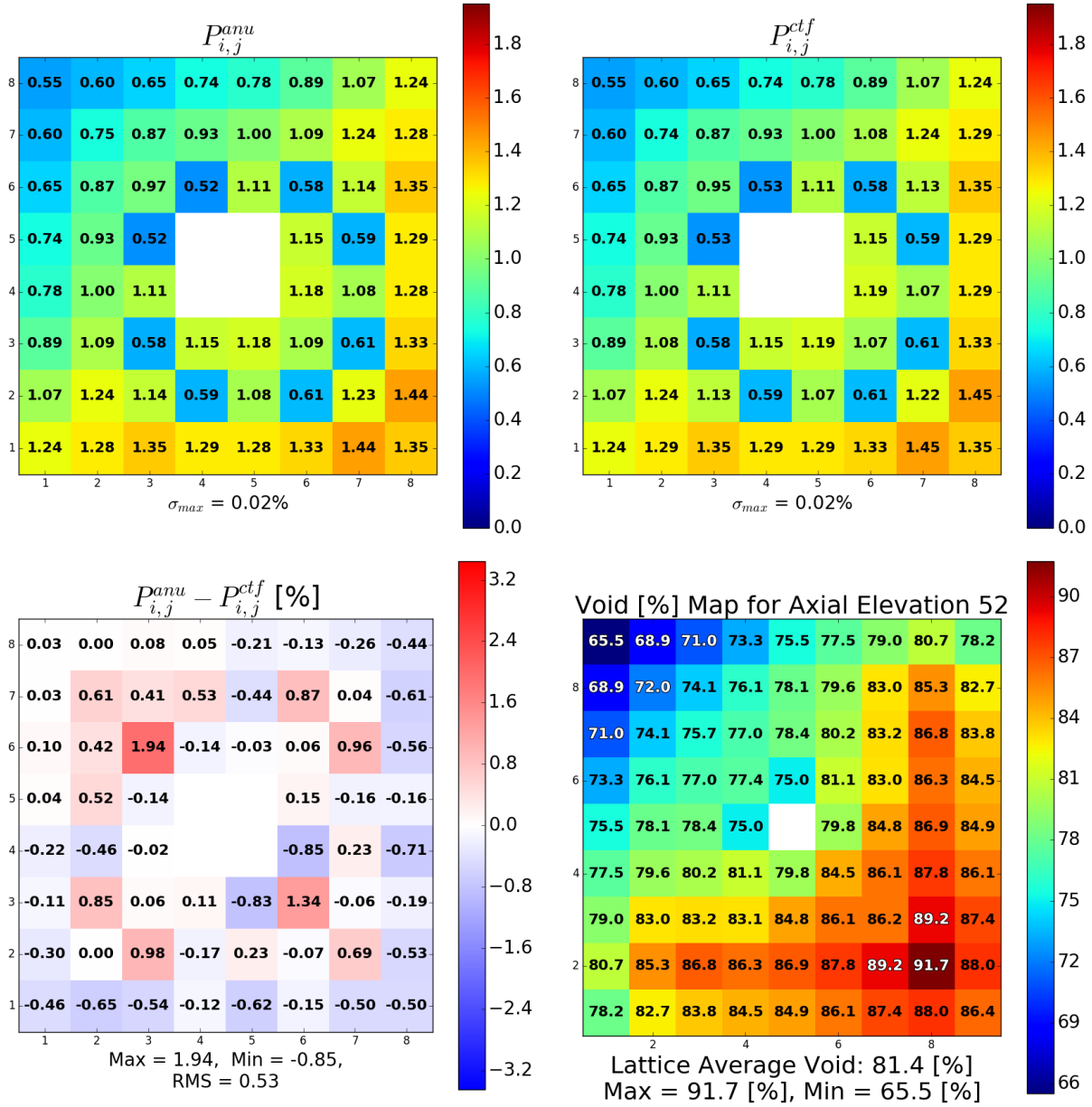

Figure 50. Comparison of normalized fission rates for the top of a controlled GE9 bundle in the annular flow tests.

G.2 Uncontrolled GE9

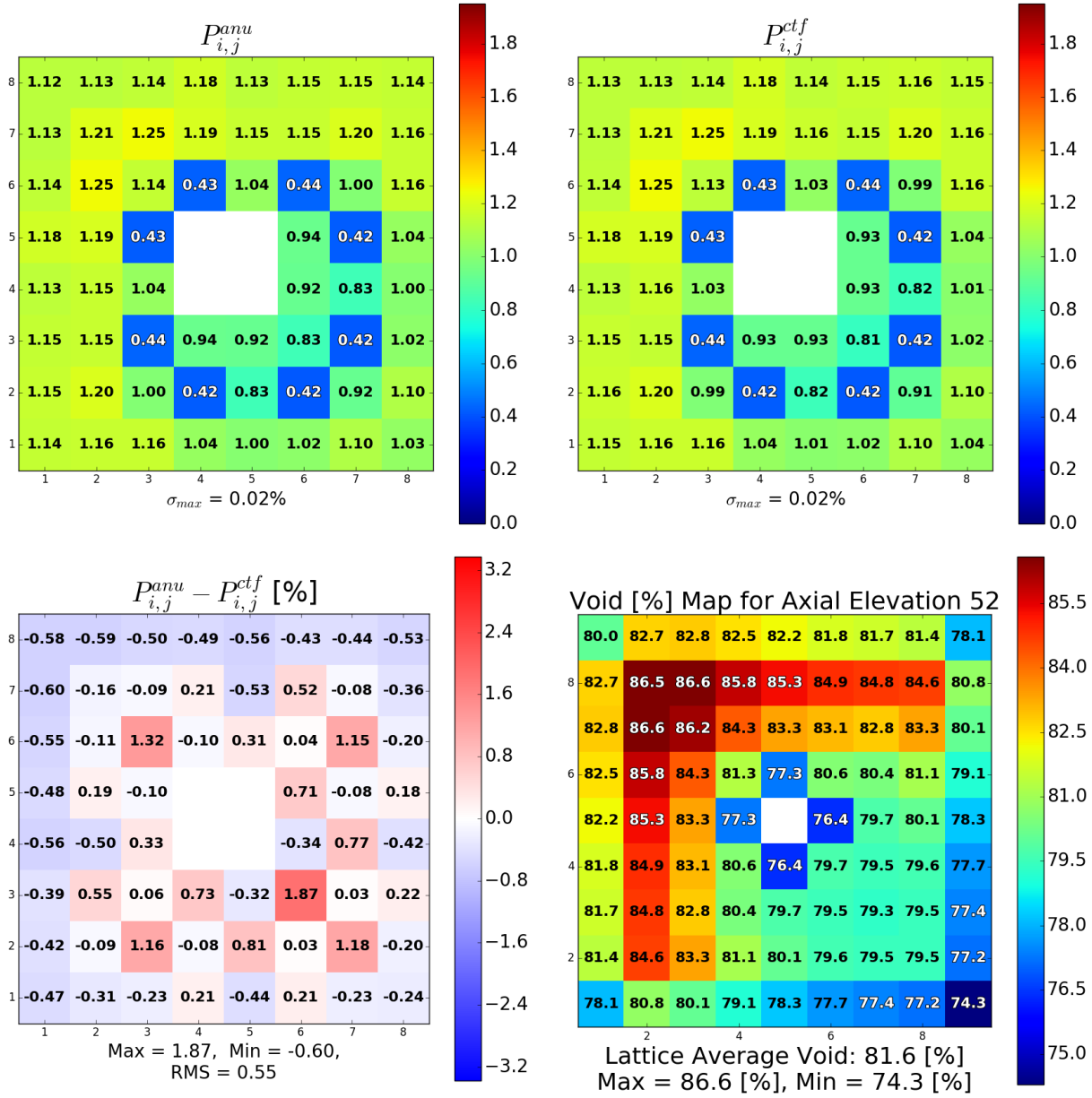

Figure 51. Comparison of normalized fission rates for the top of an uncontrolled GE9 bundle in the annular flow tests.

G.3 Controlled GE14

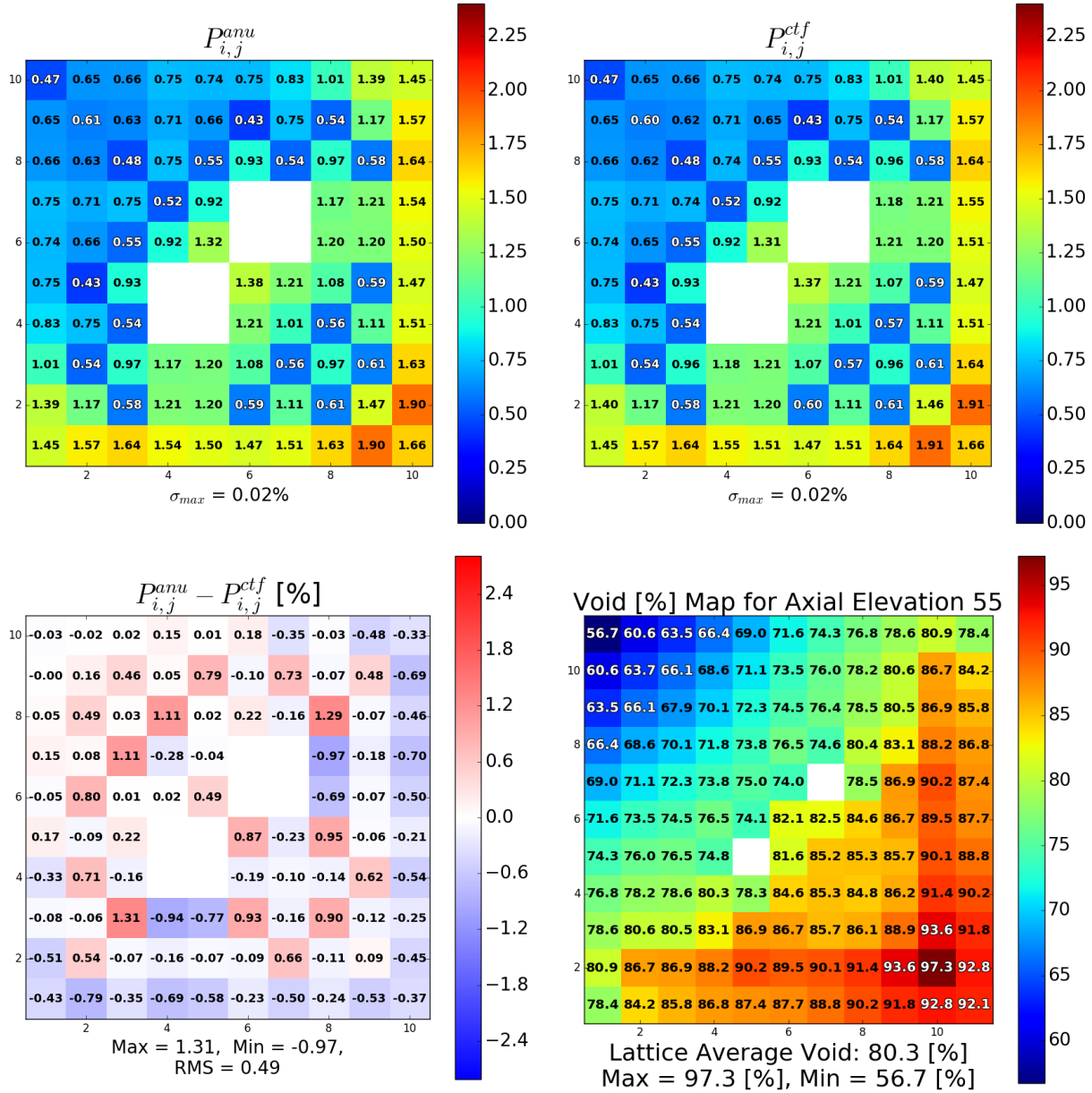

Figure 52. Comparison of normalized fission rates for the top of a controlled GE14 bundle in the annular flow tests.

G.4 Uncontrolled GE14

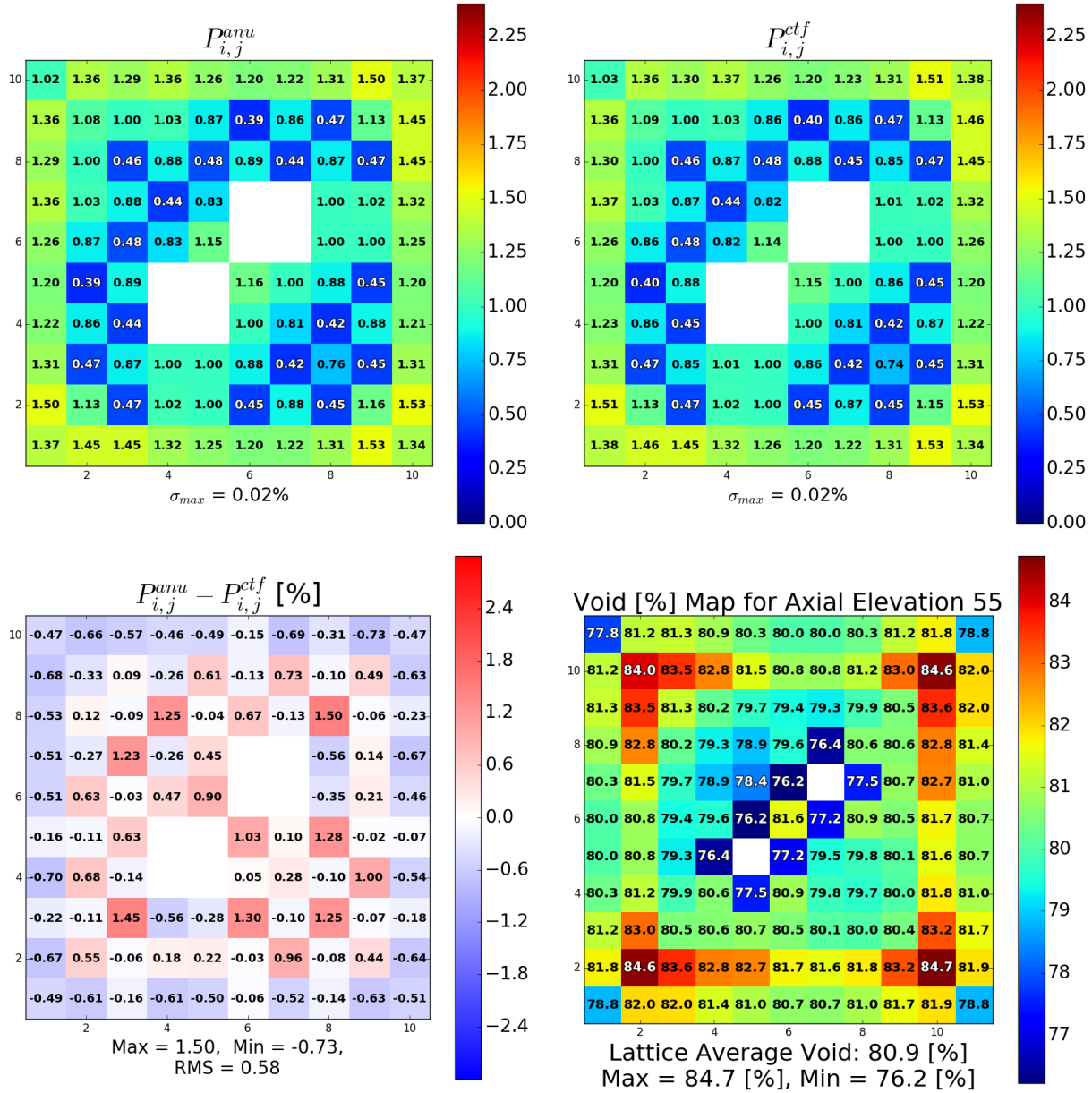

Figure 53. Comparison of normalized fission rates for the top of an uncontrolled GE14 bundle in the annular flow tests.